

**MOLECULAR DYNAMICS STUDIES ON
INTERFACE HEAT TRANSFER CONTROL USING
ELECTRIC FIELD**

**A Thesis Submitted to
the Graduate School of Engineering and Sciences of
İzmir Institute of Technology
in Partial Fulfillment of the Requirements for the Degree of**

DOCTOR OF PHILOSOPHY

in Mechanical Engineering

**by
Onur YENİGÜN**

**July 2021
İZMİR**

To my beloved grandfather, Mustafa Yenigün.

ACKNOWLEDGMENTS

First of all, I would like to express my deepest appreciation and give sincere thanks to my thesis advisor Prof. Murat Barışık, for his continuous support and guidance during this thesis. He mentored me to become an individual researcher and an instructor. Without his bright ideas, attention and diligence, this dissertation would not have been accomplishable. I also would like to thank my examining committee members, Prof. Erdal Çetkin, Prof. Haldun Sevinçli, Prof. Aytunç Erek and Prof. Alpaslan Turgut for their valuable contributions to this dissertation.

I would like to thank Turkish Academy of Sciences (TUBA) in the framework of the Young Scientist Award Programme (GEBIP2017) for supporting this dissertation and TUBITAK ULAKBIM, High Performance and Grid Computing Center (TRUBA resources) for providing the computational resources for numerical calculations reported in this thesis.

I also would like to thank my colleagues Dr.Tümcan Şen, Dr.Doğuş Zeren, Mümine Gerçek and members of “MiNaEng” Lab. for their friendship and countless times of fun memories. Their presence in my graduate education made everything so much easier.

I take this opportunity to express my gratitude to my family, Cemal, Nurten and Mustafa Can Yenigün and my grandparents Musatafa and Hatice Yenigün for their love and support throughout my whole education life.

Finally, but most importantly, I would like to thank my fiancée, love of my life, Su, for her endless care and love. I could not have finished this dissertation and I cannot imagine a world without the sunshine of your love.

ABSTRACT

MOLECULAR DYNAMICS STUDIES ON INTERFACE HEAT TRANSFER CONTROL USING ELECTRIC FIELD

Thermal management is considered as a bottleneck for the development of next generation micro/nano-electronics with high heat dissipation rates. When component sizes decrease to nanoscales, increase in surface to volume ratio leads the interfacial thermal resistance (ITR) to dominate the heat transfer behavior. The current study focuses on characterizing ITR at molecular level and exploring smart thermal management concepts for nano-scale systems. In sequence, the effect of solid thickness on ITR was investigated such that the altered phonon spectrum inside the solid domain creating the size dependency on thermal conductivity was also found to create a size dependency in ITR. Next, an active and local manipulation of heat transfer between water and various solids by an applied uniform and/or non-uniform electric field was examined. When the water molecules underwent electric field induced orientation polarization and liquid dielectrophoresis (LDEP), a substantial increase in heat transfer was developed due to the decrease in ITR and increment in thermal conductivity. Finally, an interface-localized heat transfer control technique was proposed, where interdigitated electrodes (IDEs) were embedded into the heat dissipating surface. IDEs created an electric field gradient exclusively near the electrode surface which resulted in LDEP forces on the water dipoles at near surface region enhancing solid/liquid interface energy and almost eliminating the ITR. We developed semi-empirical and theoretical relations to describe ITR variation by the electric field, which will be important for thermal management of current and future technologies.

Keywords: Nanoscale Heat Transfer, Molecular Dynamics, Interfacial Thermal Resistance, Electric Field, Liquid Dielectrophoresis

ÖZET

ELEKTRİK ALAN KULLANARAK ARAYÜZEY ISI TRANSFERİ KONTROLÜ ÜZERİNE MOLEKÜLER DİNAMİK ÇALIŞMALARI

Yüksek ısı yayılım değerleri olan yeni nesil mikro/nano elektronik cihazların geliştirilmesinin önündeki engel termal yönetim olarak değerlendirilmektedir. Bileşen boyutları nano boyutlara düştüğünde, yüzey/hacim oranındaki artış, arayüzey termal direncinin (ITR) ısı transfer davranışı üzerinde büyük etki yaratmasına yol açar. Mevcut çalışma, ITR'ı moleküler düzeyde karakterize etmeye ve nano-ölçekli sistemler için akıllı termal yönetim kavramlarını keşfetmeye odaklanmaktadır. Sırayla, katı kalınlığının ITR üzerindeki etkisi araştırıldı ve ısı iletkenlik üzerindeki boyut bağımlılığını yaratan fonon spektrumu değişimi aynı zamanda ITR üzerinde de bir boyut bağımlılığı yarattığı bulundu. Daha sonra, uygulanan homojen ve/veya homojen olmayan elektrik alan ile su ve çeşitli katılar arasındaki ısı transferinin aktif ve lokal manipülasyonu incelendi. Su molekülleri, elektrik alan kaynaklı oryantasyon polarizasyonu ve sıvı dielektroforesize (LDEP) maruz kaldığında, ITR'deki azalma ve termal iletkenlikteki artış nedeniyle ısı transferinde önemli bir artış meydana geldi. Ek olarak, birbiri içine geçen elektrotların (IDE'ler) ısı yayan yüzeye gömüldüğü bir arayüzeye lokalleştirilmiş ısı transferi kontrol tekniği önerildi. IDE'ler, yalnızca elektrot yüzeyinin yakınında bir elektrik alan gradyanı yarattı ve bu katı/sıvı arayüzey enerjisini artıran ve neredeyse ITR'yi ortadan kaldıran yüzeye yakın su dipolleri üzerindeki LDEP kuvvetlerinin oluşmasıyla sonuçlandı. Son olarak, mevcut ve gelecekteki teknolojilerin termal yönetimi için önemli olan, elektrik alanına göre ITR varyasyonunu tanımlamak için yarı ampirik ve teorik ilişkiler geliştirildi.

Anahtar kelimeler: Nanoölçek Isı Transferi, Moleküler Dinamik, Arayüzey Termal Direnci, Elektrik Alan, Sıvı Dielektroforesis

TABLE OF CONTENTS

LIST OF FIGURES	vii
LIST OF TABLES	xi
CHAPTER 1 INTRODUCTION	1
1.1. Interface Thermal Resistance	2
1.2. Use of Electric Field for Active Control of Various Physics	8
1.3. Molecular Dynamics.....	13
1.4. Objective of the Thesis.....	17
CHAPTER 2 EFFECT OF NANO-FILM THICKNESS ON THERMAL RESISTANCE AT WATER/SILICON INTERFACE.....	19
2.1. Simulation Details	20
2.2. Results and Discussion	22
2.3. Conclusion.....	29
CHAPTER 3 ELECTRIC FIELD CONTROLLED HEAT TRANSFER THROUGH SILICON AND NANO-CONFINED WATER.....	31
3.1. Simulation Details	32
3.2. Results and Discussion	34
3.3. Conclusion.....	43
CHAPTER 4 LOCAL HEAT TRANSFER CONTROL USING LIQUID DIELECTROPHORESIS AT GRAPHENE/WATER INTERFACES	45
4.1. Simulation Details	46
4.2. Results and Discussion	51
4.2.1. Uniform Electric Field.....	51
4.2.2. Non-uniform Electric Field	56
4.3. Conclusion.....	68
CHAPTER 5 HEAT TRANSFER CONTROL BY INTERFACE-LOCALIZED LIQUID DIELECTROPHORESIS USING INTERDIGITATED ELECTRODES	70
5.1. Simulation Details	71
5.2. Results and Discussion	75
5.3. Conclusion.....	88
CHAPTER 6 SUMMARY.....	89
REFERENCES	92

LIST OF FIGURES

<u>Figure</u>	<u>Page</u>
Figure 1.1. Heat Assisted Magnetic Recording (HAMR) writing scheme (Stipe et al., 2010).....	1
Figure 1.2. Temperature jump (ΔT) and Kapitza length (L_K) description at solid/liquid interface.....	4
Figure 1.3. (a) Temperature discontinuity of typical solid/liquid interface and (b) temperature continuity of crystal/melt interface	7
Figure 1.4. Enhanced surface wetting as a function of electric field strength (Song et al., 2013).....	9
Figure 1.5. Electrowetting on dielectric (EWOD) methodology (Chae et al., 2014).....	11
Figure 1.6. Dielectrowetting spreading of a droplet with varying voltage (McHale et al., 2011).....	12
Figure 1.7. Lennard-Jones potential as a function of intermolecular distance	15
Figure 1.8. Coulombic potential as a function of intermolecular distance	16
Figure 2.1. Simulation domains with different silicon thicknesses (a) 5nm, (b) 8nm, (c) 13nm, (d) 25nm, (e) 40nm and (f) 60nm.	20
Figure 2.2. Temperature distributions of the systems with nano-film thicknesses of 5, 8, 13, 25, 40 and 60nm with (a) $1.0 \times \epsilon^* \text{Si-O}$, (b) $0.4 \times \epsilon^* \text{Si-O}$ and (c) $0.125 \times \epsilon^* \text{Si-O}$	23
Figure 2.3. Thermal conductivity of silicon varying with nano-film thickness	25
Figure 2.4. Near wall density profiles of different nano-film thicknesses at different interaction parameters of (a) $0.125 \times \epsilon^* \text{Si-O}$, (b) $0.4 \times \epsilon^* \text{Si-O}$ and (c) $1 \times \epsilon^* \text{Si-O}$	26
Figure 2.5. (a) Variation of Kapitza Length by interaction strength. (b) Variation of Kapitza Length normalized with bulk L_K (60nm nano-film) by nano-film thickness.	28
Figure 2.6. Variation of Kapitza Length normalized with bulk L_K (60nm nano-film) by thermal conductivity normalized with bulk k (Sellan et al., 2010).....	29
Figure 3.1. Simulation domain for silicon water system under uniform electric field.....	32

<u>Figure</u>	<u>Page</u>
Figure 3.2. Temperature distributions at electric field strengths of 0, 0.35, 0.70 and 1.05 V/nm	35
Figure 3.3. Water density distributions at different electric field strengths	36
Figure 3.4. Water density distributions at different electric fields (a) near hot surface with positively charged electrode and (b) near cold surface with negatively charged electrode	36
Figure 3.5. Density distributions of water under electric field varying from 0.44 to 0.96 V/nm	37
Figure 3.6. Water density distributions of high electric field range (a) near hot surface with positively charged electrode and (b) near cold surface with negatively charged electrode	37
Figure 3.7. The snapshots of the silicon/water system at electric fields of (a) 0, (b) 0.18, (c) 0.35, (d) 0.40, (e) 0.44, (f) 0.53, (g) 0.61, (h) 0.61 (i) 0.79 and (j) 0.88 V/nm	39
Figure 3.8. The snapshots of the silicon/water system under 0.88 V/nm electric field at (a) 3D view, (b) side view, (c) ice (0,0,1) view and (d) ice (1,0,1) view	40
Figure 3.9. Normalized temperature profiles of water under electric fields varying from (a) 0 to 0.4 V/nm and (b) 0.4 to 0.96 V/nm	40
Figure 3.10. (a) Thermal conductivity of water and (b) Kapitza length as a function of electric field strength	41
Figure 3.11. Total heat flux through the nano-confined water as a function of applied electric field strength	43
Figure 4.1. Simulation domain of graphene/water system for (a) uniform and (a) non-uniform electric field studies	47
Figure 4.2. Simulation domain of graphene water system under non-uniform electric field for numerical calculation by COMSOL	51
Figure 4.3. Density distributions at electrode charges of 0, 0.018, 0.036, 0.044 and 0.053 e per atom	52
Figure 4.4. The snapshots of the water confined in graphene under uniform electric field with electrode charges of (a) 0, (b) 0.018, (c) 0.036, (d) 0.044, (e) 0.053, (f) 0.062 e per atom and (g) the corresponding probability distributions of water dipoles	53

<u>Figure</u>	<u>Page</u>
Figure 4.5. Temperature distributions of graphene/water system (a) before electro-freezing and (b) after electro-freezing (larger markers indicate averaged temperature profile)	54
Figure 4.6. (a) Kapitza length and (b) Thermal conductivity of water and (c) non-dimensional heat flux as a function of electrode charge	55
Figure 4.7. (a-h) Electric field contours, (g-l) molecular orientations, (m-r) dipole moment vectors of water molecules and (s-x) density contours at different electrode charges	59
Figure 4.8. Temperature contours at different electrode charges of (a) $q_{plate}=0$, (b) $0.025 e$, (c) $0.05 e$, (d) $0.075 e$, (e) $0.1 e$ and (f) $0.125 e$	60
Figure 4.9. (a) Representation of the regions for local measurements. Temperature counter of $q_{plate}=0.12e$ case was used in figure. Local variation of (b) LK-Hot, (c) LK-Cold, and (d) water density measured at each local region for different electrode charges	62
Figure 4.10. (a) Kapitza Length values at hot and cold interfaces under varying uniform and non-uniform electric fields. (b) Local water thermal conductivities in line with pin and plate electrodes compare to water thermal conductivity under uniform electric field.....	63
Figure 4.11. Temperature contours of $q_{Plate}=0.075 e$ case with different heat transfer directions as the pin electrode on (a) hot and (b) cold reservoir side.....	66
Figure 4.12. Variation of local heat rates at pin and plate electrode regions under non-uniform electric field as a function of electrode charge. Results of uniform electric field case are given for comparison	68
Figure 5.1. Molecular dynamics simulation domain for nano-interdigitated electrodes.....	72
Figure 5.2. Finite element simulation domain for nano-interdigitated electrodes with electric field contour and electric field lines	73
Figure 5.3. Electric field contours for surface charge densities of (a-e) 0.3 , (f-j) 0.5 and (k-o) $0.6 C/m^2$ with electrode widths of 0.5 , 1 , 1.5 , 3 and $5nm$ and (p) average electric field strength values at $1nm$ away from the surface for varying electrode widths.....	76

<u>Figure</u>	<u>Page</u>
Figure 5.4. Density contour of water molecules for IDE with 3nm electrode width and 0.6 C/m ² surface charge density	77
Figure 5.5. Near wall density distributions of water molecules for different electrode widths and for surface charge densities of (a) 0.3 C/m ² , (b) 0.5 C/m ² and (c) 0.6 C/m ²	78
Figure 5.6. Dipole vectors of water molecules for nano-interdigitated electrodes with surface charge densities of (a-e) 0.3 C/m ² , (f-j) 0.5 C/m ² and (k-o) 0.6 C/m ² with 0.5, 1, 1.5, 3 and 5nm electrode widths, respectively	79
Figure 5.7. Temperature contour of water molecules for IDE with 3nm electrode.....	81
Figure 5.8. Temperature distribution of water and carbon molecules for different electrode widths and for surface charge densities of (a) 0.3 C/m ² (b) 0.5 C/m ² and (c) 0.6 C/m ²	81
Figure 5.9. Kapitza Length values for different electrode widths and surface charge densities for (a) hot wall, where IDEs are placed and (b) cold wall	83
Figure 5.10. Kapitza Length variation with average electric field strength 1nm away from the surface for different surface charge densities.....	84
Figure 5.11. Normalized heat flux values for average interface electric field strength for different surface charge density and electrode widths.....	85
Figure 5.12. Total thermal resistance of the system with varying system height and corresponding proportion of Interface Thermal Resistance of both hot and cold surfaces to the total thermal resistance	87

LIST OF TABLES

<u>Table</u>	<u>Page</u>
Table 2.1. Molecular interaction parameters used in the current study	21
Table 2.2. Interaction strength values between Silicon and Oxygen	21
Table 2.3. Kapitza length values measured at different nanofilm thicknesses and at different surface wettings.	27
Table 3.1. Molecular interaction parameters used in the current study	33
Table 4.1. Electric charges assigned on pin and plate electrodes and number of water molecules simulated at each case	48
Table 4.2. Molecular interaction parameters used in the current study	49
Table 5.1. Molecular interaction parameters used in the current study	72

CHAPTER 1

INTRODUCTION

Nanoscale heat transfer is crucial due to the advancements in nano-fabrication techniques led to characteristic length of the electronic, optoelectronic and photonic devices to decrease from micrometers to nanometers. Miniaturization bringing the need for removal of high heat fluxes per area complicates heat transfer. For example, sub 3nm transistors can be manufactured by the semiconductor industry (Seon et al., 2021). The reduction in transistor size yields increased packing on a single chip and increased computational power, but also results in extremely high heat generation. If the growth in power density continues similar to the predictions of the Moore's Law, heat generation per area of a microprocessor will reach the heat flux of the sun's surface (Zhang and Guo, 2012). Furthermore, new technologies such as Heat Assisted Magnetic Recording (HAMR) (Figure 1.1) develop with the need for more storage, where a laser beam heats a 20nm spot and then needs to be cooled down in nanoseconds (Ju et al., 2015). Hence, thermal management has become one of the main challenges for the future technologies. Therefore, it is of great significance for the development of such devices to understand, characterize and manipulate the nanoscale heat transfer.

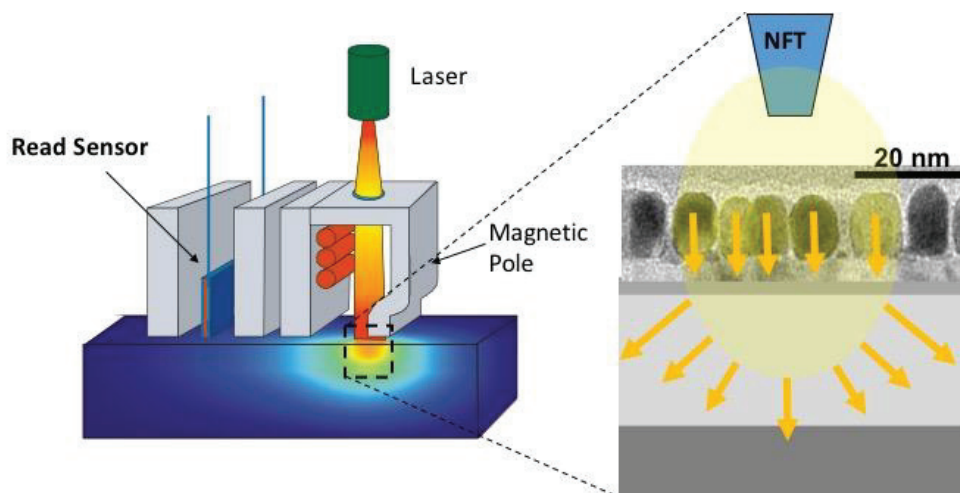


Figure 1.1. Heat Assisted Magnetic Recording (HAMR) writing scheme (Stipe et al., 2010)

There are two non-continuum mechanisms that interrupts heat transfer at nanoscale. First, a decrease of solid size alters the heat conduction inside a semi-

conductor solid domain which diverges from the conventional bulk scale behavior. This nanoscale size effect is a well-known phenomenon observed both numerically and experimentally by many researchers (Asheghi et al., 1998, Ju and Goodson, 1999, Schelling et al., 2002, Liu et al., 2004, Ma et al., 2012, Dong et al., 2014) as the reduction of solid thermal conductivity by decreasing length. When the nano-film thickness becomes shorter than the bulk value of the phonon mean free path (MFP), the spectrum of heat-carrying phonons inside the solid domain develops different than the bulk phonon propagation and the resulted thermal conductivity decreases. Second, decrease of component size in a micro/nano system increases the number of interfaces and their influence. The heat transfer between two dissimilar materials is interrupted due to the mismatch in their phonon spectrum. Such difficulty of phonon passage is characterized by the interface thermal resistance (ITR) which becomes the most dominant mechanism by the increase of surface-to-volume ratio.

In order to characterize nano-scale heat transfer, experiments and theoretical investigations are conducted in the past (Ge et al., 2006, Landry and McGaughey, 2009, Gatapova, 2016). However, conducting such experimental investigations are expensive and requires sophisticated instruments. On the other hand, conducting molecular dynamics simulations are proved to be a good alternative to the experiments by many researchers. Furthermore, with the increase of systems consist of many substrates and layers, significance of interface thermal resistance is become prominent. Molecular dynamics simulations allow researchers to investigate the effect of interface thermal resistance on nano-scale heat transfer extensively, by varying numerous interface and material properties. However, literature is still far from a complete understanding and further studies require for a better design of enhanced heat dissipation.

1.1. Interface Thermal Resistance

When two dissimilar dielectric materials are in contact with each other, a temperature jump occurs at the interface due to the phonon mismatch of these materials and it is known as Interfacial Thermal Resistance (ITR). Especially, with increased surface to volume ratio caused by the miniaturization trend, ITR can highly interrupt the heat transfer process at the interface. Interface thermal resistance phenomenon is first

discovered by Kapitza in 1941 during investigating super-fluidity of Helium, experimentally. Kapitza measured a discontinuity in the temperature distribution at the junction of He II and heated metal surface, while trying to comprehend why the actual thermal conductivity of He II in capillary is higher than the bulk thermal conductivity of He II. In these experiments, thermal resistance of $2 \text{ m}^{\circ}\text{Kcm}^2/\text{mW}$ were measured while the temperature is in the order of 2°K . (Kapitza, 1941, Pollack, 1969). There are different methods available for the characterization of Interfacial thermal resistance. First, interfacial thermal resistance can be expressed as a function of heat flux (\vec{q}) and the temperature jump at the interface of dissimilar materials (ΔT) as,

$$\Delta T = -R_K \vec{q} \cdot \vec{n} \quad (1.1)$$

where \vec{n} is the surface normal vector and R_K is the interfacial thermal resistance, also known as Kapitza resistance. Second, an analogous definition for the Kapitza resistance is widely used in the literature, which is called Kapitza length. As illustrated in Figure 2.1, Kapitza length is calculated by extrapolating the temperature gradient of the liquid until it reaches the temperature of the solid at the interface. Then, Kapitza length (L_K) can be expressed as a function of temperature jump at the interface and the temperature gradient of the liquid as in the following equation,

$$\Delta T = L_K \left. \frac{\partial T}{\partial n} \right|_{\text{liquid}} \quad (1.2)$$

where $\partial T/\partial n$ is the temperature gradient of the liquid and ΔT is the temperature jump at the liquid/solid interface. Kapitza length (L_K) is correspondent of “Velocity Slip” in liquid flow tangential to the surface.

There are multiple experimental (Kapitza, 1941, Pollack, 1961, Ge et al., 2006, Gatapova, 2016) and computational studies regarding dependence of ITR and the resulted heat transfer on interface properties, such as surface wetting (Murad and Puri, 2008, Kim et al., 2008, Shi et al., 2012, Alexeev et al., 2015), surface temperature (Barisik and Beskok, 2012, Pham et al., 2014, Song and Min, 2013, Barisik and Beskok, 2014, Vera and Bayazitoglu, 2015), surface atomic density (Vo et al., 2016, Saleman et al., 2017, Vo and Kim, 2018) liquid pressure (Pham et al., 2013, Han et al., 2017), size effect (Liang et al., 2014, Alexeev et al., 2015, Pham et al., 2016) and thermal oscillation frequencies (Kim et al., 2012, Giri et al., 2017).

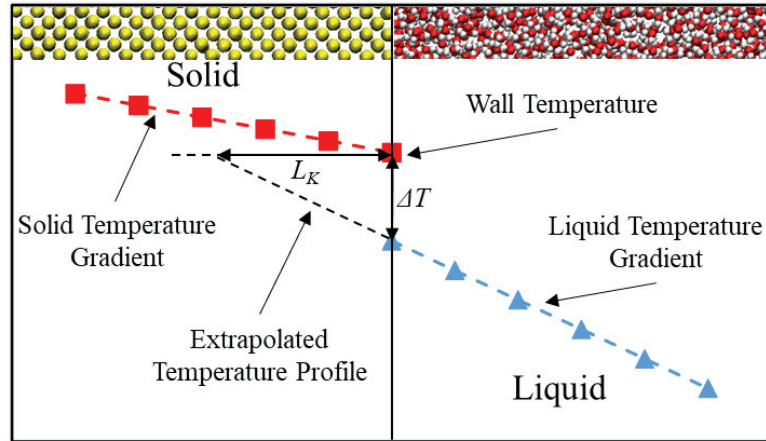


Figure 1.2. Temperature jump (ΔT) and Kapitza length (L_K) description at solid/liquid interface

Experimental measurements of L_K are reported between water and chemically functionalized solids (Ge et al., 2006). These chemically functionalized solids have Aluminum and Gold layers at the water interface to investigate the thermal conductance on both hydrophobic and hydrophilic surfaces, respectively. The thermal conductance at the interface is measured with time-domain thermoreflectance method and Kapitza length values are found 10-12nm and 3-6nm for hydrophobic and hydrophilic surfaces, respectively. Another study also experimentally investigated the temperature jump at the water/air interface while evaporation took place at the heater surface (Gatapova et al., 2016). At normal atmospheric conditions, temperature profiles are measured across the liquid/gas interface with a specially manufactured micro thermocouple with a sensor thickness of $4\mu\text{m}$. Different temperature jumps are clearly observed over varying heater temperatures. Specifically, detailed data on the temperature dependence of the temperature jump at the liquid/gas interface are reported and validated with kinetic theory, qualitatively and with classical energy balance on the interface, quantitatively.

Effect of surface wetting on interface thermal resistance is investigated across silica wafer and water vapor interface with varying surface wetting properties with Molecular Dynamics (MD) simulations (Murad and Puri, 2008). A significant reduction in the interface thermal resistance was observed as the surface transformed into more hydrophobic nature. The main reason behind this phenomenon is the improved intermolecular interaction frequencies with the increase in adsorption and absorption at the surface. Another study reported significance of interaction strength between the

solid/liquid coupling on the interface thermal resistance with molecular dynamics simulations. No temperature jumps are observed with high solid/liquid coupling interaction parameters. However, with weak solid/liquid interaction potentials temperature jumps took place at the interface. (Kim et al., 2008) In addition, the heat conduction between liquid argon confined between silver and graphite walls are investigated, separately. Silver and graphite walls are selected on purpose since the interaction parameter between silver/argon pair is twelve times higher than graphite/argon pair. Such significant difference in interaction parameter on solid/liquid coupling represents different surface wetting conditions. As a result, well known density layering at near wall regions are observed and the density peaks of liquid argon showed different values for silver and graphite surfaces in accordance with their interaction strength parameters. Finally, Kapitza length at silver/argon interface measured three times smaller than the Kapitza length at graphite/argon interface in parallel with their corresponding density layering and peaks. (Shi et al., 2012). In order to reveal liquid layering effects, the Kapitza resistance at few-layer graphene and water interface is investigated, where the wettability of the surface, pressure, channel height and number of graphene layers are systematically varied (Alexeev et al., 2015). It is observed that with increased wettability and pressure, density peak near the graphene surfaces are increased drastically and resulted in reduction of the interfacial thermal resistance. In addition, changing channel height did not affect both near wall density peak of water and interface thermal resistance between graphene and water. However, it is documented that increasing the number of graphene layers decreased the thermal resistance at the graphene/water interface without affecting the density peak up to a point where the length of the graphene came to a balance with phonon mean free path of the c-axis graphene. Effect of ordered water layers near graphene wall is further investigated, where graphene layer adjacent to water is inserted with negative and positive charges, to substantially decrease the interface thermal resistance (Ma et al., 2018). Effect of different charge decorations and intensities on interface heat transfer are studied. When surface charges are presented, water molecules got attracted to the charged graphene wall due to coulombic interactions and created ordered water layering near the wall, which is the main reason for the reduction on interface thermal resistance. Another reason for this reduction is the additional heat channel generated by the improved coulombic interactions between the charged carbon atoms and water molecules. Such phenomenon is proved with comparing the heat transfer rates of the same graphene/water system without surface charges but with increased

interaction strength parameter, in which density peak of the liquid layering matches with the original system. Results showed that the heat transfer rate of the original system is 20% higher than the other one, even though they have the exact same near wall liquid layering. Finally, 97% reduction in the Kapitza resistance is reported. However, computation of Kapitza resistance is erroneous. While calculating Kapitza resistance, Ma et al., measured the temperature difference between the nearest graphene layer and liquid. This method yields fundamentally wrong thermal resistance since there is another temperature jump between the charged layer of graphene and next graphene layer without charge. Such an additional thermal resistance caused by the fact that charged carbon atoms' vibration modes are altered, thus creates a phonon mismatch with the neutral carbon atoms. Instead, temperature jumps should be calculated based on the bulk temperature gradients of both solid and liquid.

Next, temperature dependence of Kapitza length is thoroughly investigated in the literature by many researchers. However, there are contradictions between these results. While some researchers found interfacial thermal resistance results independent from wall temperatures (Pham et al., 2014), others found increasing thermal resistance with elevated surface temperature (Kim et al., 2008, Shi et al., 2012). On the contrary to the inconsistent temperature dependence of interfacial thermal resistance studies in the literature, temperature dependency of the interfacial thermal resistance is explained with varying surface wettability (Song et al., 2013, Barisik et al., 2014). Basically, variation of Kapitza length by the temperature is defined by the temperature dependence of phonon dynamics on hydrophobic surfaces, while it is dominated by the temperature dependence of near surface liquid layering on hydrophilic surfaces. Since, increased temperatures improve the phonon dynamics but decreases the liquid density peak near the surface, Kapitza length is found decreasing with increasing wall temperature at hydrophobic surfaces and increasing with increasing wall temperature at hydrophilic surfaces. Furthermore, it is found that another temperature dependency comes from different molecular dynamics boundary treatment effects. Up to this point, while investigating thermal resistance at solid/liquid interface, literature was employing constant wall temperatures by applying thermostats to all molecules in the solid domain. It is proved that by forcing all the molecules of the solid to vibrate at a certain level to maintain constant temperature creates different phonon spectrum inside the solid domain. Consequently, phonon harmony at the solid/liquid interface differs and results in altered interfacial thermal resistances. By only applying thermostats to a certain number of

molecules at far end sides of the of the solid domain, the molecules of the solid domain are allowed to develop their own phonon spectrum based on the material properties. In addition, it is documented that another thermal resistance occurs at the interface of thermostat applied molecules and thermostat free molecules of solid domain. This phenomenon is coined with artificial thermal resistance term (Barisik and Beskok, 2012).

While literature mostly studied the thermal resistance at the interfaces of dissimilar materials, Vo and Kim investigated the thermal resistance at the interface of a crystal and its melt (Vo and Kim, 2018). Based on MD simulation results, physics behind the temperature continuity at the interface of crystal and its melt are credited to the non-diffusive mismatch caused by the structural diffusivity as illustrated in Figure 1.3. No temperature jumps were observed at these interfaces due to perfect vibrational coupling of the crystal and its melt, which differed from the typical solid/liquid interface.

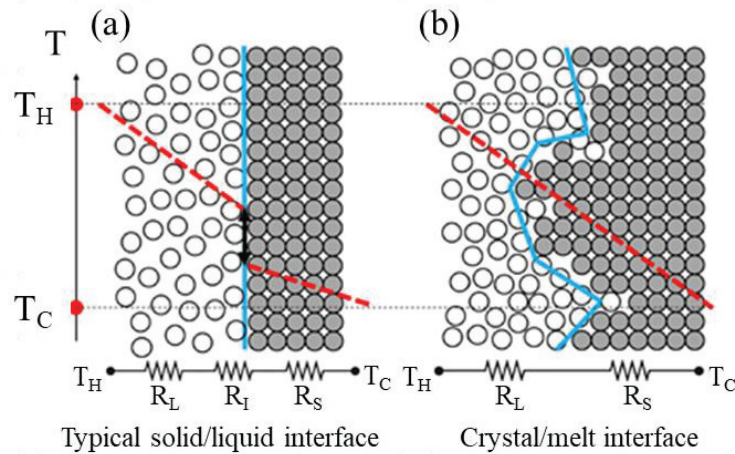


Figure 1.3. (a) Temperature discontinuity of typical solid/liquid interface and (b) temperature continuity of crystal/melt interface

Lastly, literature also focused on pressure dependence of interface thermal conductance (Pham et al., 2013, Han et al., 2017). While some researchers studied the effects of pressure on Kapitza length with both hydrophobic and hydrophilic surfaces (Pham et al., 2013), others focused on the resulting effects on the vibrational modes of the phonon spectrum at the pressure applied interface. Molecular dynamics studies showed that pressure dependence of interface thermal conductance vary with surface wettability. Specifically, heat transfer across the interface of liquid and hydrophilic surface found independent from increased bulk pressure due to the stable near wall density peak by strong adsorption on the surface. However, hydrophobic surfaces showed significant increase in the initially poor thermal coupling at the liquid interface due to increased liquid layering. In addition, phonon spectral analysis results showed that

density of high frequency vibrations is increased with the increased pressure, while the low frequency vibrations remain constant. Enhanced high frequency phonon interactions are result of improved liquid structuring at the near wall region (Pham et al., 2013, Han et al., 2017).

In this section, literature on how various properties altered interface thermal resistance is covered. Studies show that surface wetting is one of the most effective interface properties that effect interfacial thermal resistance. Hydrophilic surfaces transport heat better due to increased liquid layering near the solid surface created by enhanced solid/liquid interface energy. In addition, similar liquid layering effect can be captured by increasing the pressure at the solid/liquid interface. In the light of these information, researchers modified the surface wetting by chemically altering the surface (Ge et al., 2006, Shenogina et al., 2009), employing nano structures at the surface (Wang and Koblinski 2011, Huang et al., 2013) and assigning surface charges (Ma et al., 2018) to increase interface heat transfer significantly. Previously mentioned techniques provided passive surface wetting and heat transfer control. However, recent technologies require more sophisticated, active control techniques for surface wetting and need-based heat transfer.

1.2. Use of Electric Field for Active Control of Various Physics

The electric field is the physical field around the charged particle within which the other charged particles or molecules experience the force of attraction or repulsion. In a confined dielectric liquid, electric field can manipulate the orientation of the dipole of the dielectric liquid molecules and/or increase solid/liquid coupling at the interface through electrostatic interactions between charged molecules. Most common electric field applications in micro/nano scale systems are electrowetting on dielectric (EWOD), dielectrowetting and liquid dielectrophoresis (LDEP), in which the surface wetting can be altered, liquid actuation can be achieved and heat transfer can be enhanced.

Electric field can manipulate solid/liquid coupling through the electrostatic interactions between the charged wall and the liquid. This process is also known as electrowetting, where interface energy between solid and liquid can be actively controlled by an electric field (Mugale and Baret, 2005). Wetting is a measure of how the liquid

behaves when it is in contact with a solid surface. There are different ways to manipulate surface wetting such as, employing nanostructures at the surface (Lundgren et al., 2003, Spori et al., 2008, Chen et al., 2014, Zhang et al., 2016) or using surface coatings (Motezakker et al., 2017, Li et al., 2017, Sadaghiani et al., 2018). However, these methods are passively controlling the surface wetting by changing the surface morphology by either chemically or mechanically. On the other hand, electrowetting is a method that actively controls the surface wetting, by applying an electric field parallel or perpendicular to the surface. Molecular Dynamics simulations have been used to investigate electrowetting applications as shown in Figure 1.4, where enhanced wettability of nano water droplets is observed with applied electric field parallel to the surface (Zhang et al., 2016). It is documented that as electric field strength increases, wetting angle decreases due to the stronger solid/liquid coupling and the surface becomes more hydrophilic.

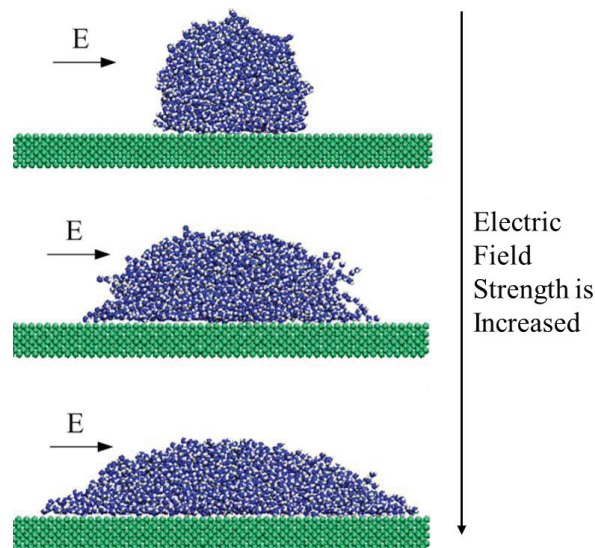


Figure 1.4. Enhanced surface wetting as a function of electric field strength (Song et al., 2013)

There are two electric field application methods that can control surface wettability through electrohydrodynamic effects on the three-phase contact line of a droplet, which are electrowetting on a dielectric (EWOD) and liquid dielectrophoresis (LDEP) mechanisms. In EWOD applications, the electrodes are covered by a hydrophobic dielectric layer and the apparent contact angle of a droplet is controlled by applying alternating/direct current (AC/DC) voltage between the electrode and droplet as illustrated in Figure 1.5 (Chae et al., 2014). Free ions inside of the conducting droplet aggregate near the electrode interface with the application of electric field, creating a

coulombic force. Due to the maximum outward portion of the coulombic force, free ions tend to accumulate at the interface of three-phase contact line, which results in spreading motion of the liquid droplet. EWOD is being used in various applications such as planar receiver coils (Byun et al., 2015), liquid droplet actuation and transport in microfluidics (Pollack et al., 2000, Lee et al., 2002, Barman et al., 2015), microdroplet tensiometer (Banpurkar, 2008) and micro air bubble control (Zhao et al., 2007). However, this effect is only valid when the liquid has ions in it. If the liquid is deionized, there are different effects which play a role on the surface wettability, as follows; electro-stretching effect (Luedtke et al., 2011, Yen 2012, Song et al., 2013, Lee et al., 2013) and bias polarity effect (Gubskaya and Kusalik, 2002, Daub et al., 2007). Assuming that, a uniform electric field is applied to a dielectric liquid droplet, the system free energy depends on the surface tension and depolarization of the liquid. When the electric field strength is increased, the droplet shape tends to elongate in the direction of the field, causing electro-stretching (Yen, 2012). In bias polarity effect, the water dipole orientation distribution is influenced by the electric field, which cannot be neglected at the nanoscale. While an external electric field is applied perpendicularly to the surface, the OH bonds are more likely to point towards the charged solid surface. Hence, dipolar molecules tend to be drawn closer to the surface due to increased coulombic interaction, which results in reduction of the interfacial free energies. Thus, reduction of the contact angle is achieved (Daub et al., 2006). When the electric field strength is further increased, the water molecules start to form crystalline structures while dipole moments are aligning through the electric field direction. In the literature, this phenomenon is known as electro-freezing, which is well established both numerically and experimentally (Luedtke et al., 2011, Braslavsky et al., 1998, Evans et al., 2007, Wei et al., 2008, Bratko et al., 2008, Xie et al., 2010, Hu et al., 2012, Yan et al., 2012). Furthermore, when the liquid molecules start form a greater structural order, it enhances phonon transfer, which increases the thermal conductivity of the liquid. Evans et al., reported that the thermal conductivity of the water increases 3 times when under strong electric fields (Evans et al., 2007). Moreover, in polarized liquids under uniform electric field, the forces on the two charges of the dipole are in balance, so the net force on the dipoles is zero. However, it exerts a torque on the dipoles to align them on the electric field direction. The situation is different if the electric field is non-homogenous. Since there is an electric field gradient, the forces on the two ends of the dipoles are different than each other, which creates an overall force and bulk fluid motion (Jones, 2001). Consequently, dipoles of the deionized liquids exposed to a non-uniform

electric field experience a force towards higher electric field gradient region. Such phenomenon is known as liquid dielectrophoresis (LDEP) (Edwards et al., 2018).

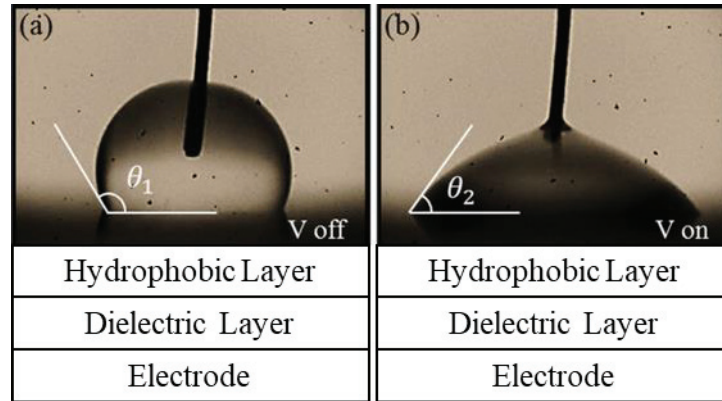


Figure 1.5. Electrowetting on dielectric (EWOD) methodology (Chae et al., 2014)

Liquid dielectrophoresis (LDEP) is first investigated by Pellat in 1895 by demonstrating the dielectric liquid (insulating oil) motion driven by non-uniform electric field against gravity (Pellat, 1895). The experiment was consisting of two parallel electrodes separated by a distance and submerged in a dielectric liquid. When a voltage is applied between the electrodes, an electric field gradient is created at the liquid/air interface, which generates an upwards motion of the dipoles of the dielectric liquid against gravity to a new equilibrium height between the electrodes. Nowadays, liquid dielectrophoresis is mostly used in micro/nano-fluidic devices for precision liquid actuation, droplet dispensing and wetting control purposes along with electro-wetting-on-dielectric (EWOD) (McHale et al., 2011). The electro-wetting phenomenon is actuated in EWOD approach by the charged ions accumulated at the solid-liquid interface between electrode covered by dielectric hydrophobic layer and droplet of conducting liquid acting as capacitive structure. The contact angle can be controlled with modulating the voltage between the electrode and the droplet by generating an electrohydrodynamic force at the droplets three-phase contact line (Chen and Bonaccurs 2014). On the other hand, LDEP creates a bulk force on the dipoles of the dielectric liquid towards the higher electric field gradient. To modify the energy balance at the solid-liquid interface, the bulk liquid dielectrophoresis can be converted into an interface-localized form by using interdigitated electrodes. This is also known as dielectrowetting (McHale et al., 2011). Main advantage of dielectrowetting over EWOD is based on its ability to distribute the droplet over the interdigitated electrodes as thin film and prevail the contact angle saturation as documented in Figure 1.6.

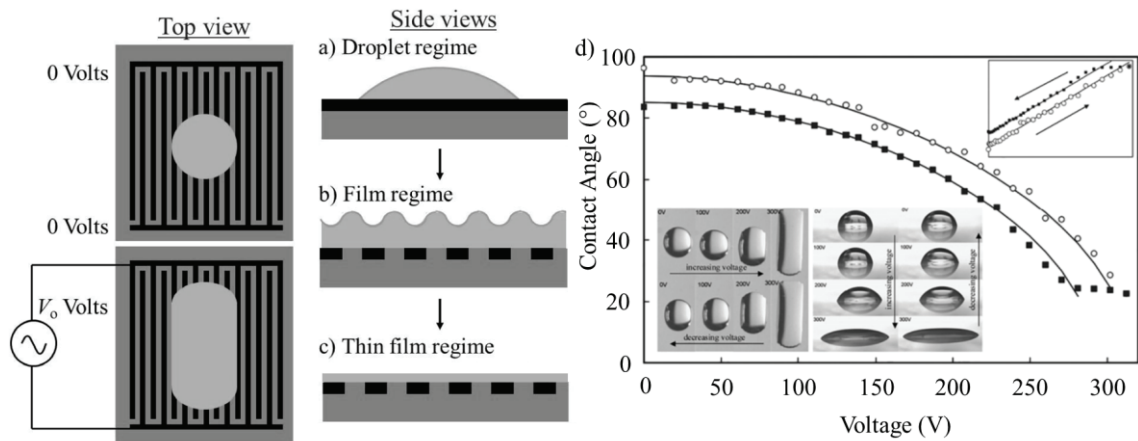


Figure 1.6. Dielectrowetting spreading of a droplet with varying voltage (McHale et al., 2011)

Lastly, using electric field to enhance boiling heat transfer is a well-known application (Celestini et al., 2012, Shahriari et al., 2014, Shahriari et al., 2017, Wang et al., 2017, Sur et al., 2018). Biggest problem of the boiling heat transfer is the vapor film formation on the surface (i.e., Leidenfrost phenomenon), which limits the heat transfer and leads to breakdown of the structure due to high surface temperature (Celestini et al., 2012). By applying electric field, this vapor film formation can be avoided. The interface electric field within the vapor film can draw fluid towards the surface and boost surface wetting.

In this section, what kind of physics that electric field can create, and its fundamental applications are discussed. Studies show that surface wettability can be enhanced significantly with applied electric field, where contact angle decreases with increased voltage. In addition, dielectric liquid molecules are influenced by the presence of electric field in terms of change in dipole orientation with uniform electric field and forces acted on dipoles with non-uniform electric field. These mechanisms are proved to be useful to enhance heat transfer during boiling process while eliminating the vapor film formation of the hot surface by attracting the fluid towards the surface and has a potential to do a lot more. Electrowetting phenomenon is also demonstrated by Molecular Dynamics simulations, which gives researchers opportunity to do a wide range of studies without the cost of expensive experimental facilities.

1.3. Molecular Dynamics

Theoretically, deficiency in overlap between phonon dispersions of different materials can be calculated by The Mismatch Models, where the upper and lower limits of ITR can be predicted by either neglecting phonon scattering or assuming diffusive phonon scattering. But determination of the true ITR value requires calculation of both harmonic and the anharmonic wave behaviors developing in a certain crystal structure with boundaries. For such a case, the coupled motions of the atoms in real space under both intra- and inter-molecular force interactions can be modeled by Molecular Dynamics (MD) with LAMMPS (Large-scale Atomic/Molecular Massively Parallel Simulator) algorithm (Plimpton, 1995). MD provides the natural formation and transport of phonons via vibrations in the crystal lattice and has been practiced by many to study heat transport of semi-conductors and liquids. (Ge et al., 2006, Shi et al., 2012, Pham et al., 2013 and Barisik and Beskok, 2014)

In molecular dynamics simulations, Newton's equations of motion are integrated in time for a system of interacting molecules to measure the instantaneous positions and velocity of all the molecules in the system. To do that, MD calculates the forces acting on the molecules derived from the potential energy in atomic description and utilizes a time integration algorithm, namely, Velocity Verlet Algorithm.

Briefly, Verlet Algorithm evaluates current force ($f(t)$) through atomic interactions and computes position (r) at a next time step (δt). And then adds current-force term to velocity ($v(t)$), which gives the velocity at half-time step. Next, a new-force term is calculated at the new position and added to the velocity, which becomes the new velocity at full-time step. This algorithm continues for all the molecules in the system, until the specified time is reached. The characteristic time step should be smaller than the fastest vibrational frequency in the system, which is typically 1 fs, so any discretization error in the integration algorithm can be avoided.

$$r(t + \delta t) = r(t) + v(t)\delta t + \frac{1}{2m} f(t)\delta t^2 \quad (1.3)$$

$$v(t + \delta t) = v(t) + \frac{1}{2m} (f(t) + f(t + \delta t))\delta t^2 \quad (1.4)$$

Molecular dynamics simulations are based on statistical mechanics and thermodynamic states. Molecular dynamics simulations represent the ensemble average of the microscopic properties of a molecular system consists of large number of molecules, which are obtained by integrating the equations of motion at a given thermodynamic state. A set of parameters are used to describe a thermodynamic state of a system, which are temperature (T), pressure (P) and the number of particles (N), volume (V) and energy (E). Some of the common thermodynamic ensembles used in statistical mechanics are documented below.

NVE: In this ensemble, equation of motion is solved while total volume and total energy kept constant in time. It is also called as microcanonical ensemble, where there is no control of temperature and pressure.

NVT: Also called as canonical ensemble, where temperature is controlled through direct scaling of the temperature. NVT stands for constant number of particles, constant volume and constant temperature.

The forces acting on the molecules, describing how particles will move in time, are determined from the derivative of the potential energy functions. In order to represent real motions of the molecules, the potential energy function (i.e., force-fields) should be selected carefully and at the same time the model should be simple as possible to reduce computational time. In molecular modelling, general form of the force-fields is combination of non-bonded and bonded interactions.

The non-bonded potentials are intermolecular interactions, which are used to describe electrostatic and van der Waals forces. Usually, to mimic van der Waals forces Lennard-Jones (LJ) potential is used, while Coulombic interactions are used for modelling electrostatic forces.

The LJ potential is said to be one of the most accurate intermolecular potentials for simple liquids, based on the balance of repulsive and attractive forces. At the same time, the LJ potential accounts for the difference between short-range repulsive forces and long-range attractive forces (dispersion forces) that occur at larger separations. This potential is given by the following equation,

$$V_{LJ}(r_{ij}) = 4\epsilon \left[\left(\frac{\sigma_{ij}}{r_{ij}} \right)^{12} - \left(\frac{\sigma_{ij}}{r_{ij}} \right)^6 \right] \quad (1.5)$$

where r_{ij} is the distance between two molecules, ϵ is the depth of the potential used to measure how much the two particles attract each other, and σ_{ij} is the molecular

diameter, which indicates the distance at which the intermolecular potential is zero. The potential distribution of a typical LJ model as a function of intermolecular distance is shown in Figure 1.7.

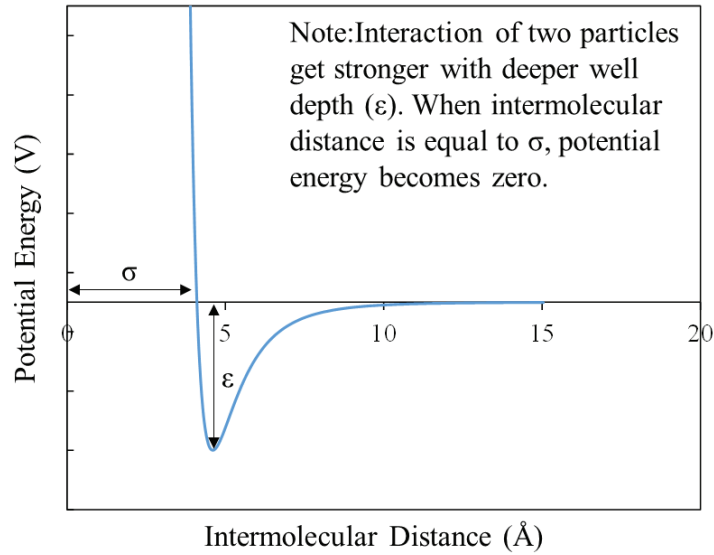


Figure 1.7. Lennard-Jones potential as a function of intermolecular distance

When there are charges present in the particles, electrostatic forces must be considered along with the van der Waals forces. As can be deduced from the Coulombic potential equation 1.6 and the typical potential energy distribution shown in Figure 1.8, if the charges have the same sign, the interaction forces are repulsive, while the charges are opposite, the interaction forces are attractive.

$$V_{Coulombic}(r_{ij}) = \frac{Cq_i q_j}{4\pi\epsilon_0 r_{ij}} \quad (1.6)$$

where ϵ_0 is the dielectric constant for vacuum, q_i values are the partial charges, r_{ij} is the distance between two charged pair.

The bonded potentials are intramolecular interactions, which models the internal energy of the interacting particles, such as covalent bonds. SPC/E water model is an example of bonded potentials, which specifies a 3-site rigid water model with LJ parameters and charges assigned to each atom (Berendsen et al., 1987). To make the model rigid, SHAKE algorithm is used to constrain the bond lengths and angle. In addition, to model the potential energy function of graphene or carbon-nanotubes, which are carbon-based nanostructures, AIREBO (the adaptive intermolecular reactive empirical bond-order) is introduced (Stuart et al., 2000).

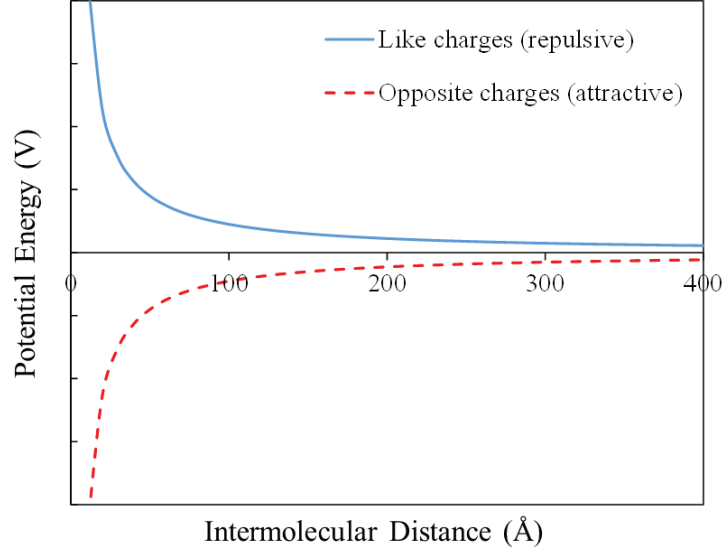


Figure 1.8. Coulombic potential as a function of intermolecular distance

After integrating the equations of motion and reaching a steady state, a statistical averaging can be done in a sufficiently long period of time to collect data. While density of the molecular systems is obtained from number of molecules inside the simulation domain, the temperature of the particles is derived from kinetic energy using the following formula,

$$T = \left\langle \frac{1}{3Nk_B} \sum_{i=1}^N m_i \bar{v}_i^2 \right\rangle \quad (1.7)$$

where k_B is the Boltzmann constant.

To compute the heat flux vector for an N particle system, Irving-Kirkwood (I-K) expression is used, while using unity differential operator approximation as follows (Irving and Kirkwood, 1950),

$$J_k = \frac{1}{Vol} \left\langle \sum_i^N V_k^i (E^i + \Phi^i) + \sum_{i,j}^N (r_k^j + r_k^i) W^{i,j} \right\rangle, \quad (1.8)$$

$$E^i = \frac{1}{2} m^i \left((V_x^i)^2 + (V_y^i)^2 + (V_z^i)^2 \right) \quad (1.9)$$

$$W^{i,j} = \frac{1}{2} \left(V_x^i f_x^{i,j} + V_y^i f_y^{i,j} + V_z^i f_z^{i,j} \right) \quad (1.10)$$

where the first term on the right-hand side of equation (1.8) is the kinetic and potential energies carried by particle i , and the second term is the energy transfer to particle i by

force interactions with the surrounding particles. In the first term, V_x^i is the peculiar velocity component of particle i in k -direction, while k is the axes of the Cartesian coordinate system; E^i is the kinetic and Φ^i is the potential energy of particle i calculated using Equations (1.5) and (1.9), respectively. In the second component of equation (1.8), $(r_k^j + r_k^i)$ is the k^{th} component of the relative distance vector between particles i and j . The $W^{i,j}$ term is given in Equation (1.10), where $f_l^{i,j}$ is the intermolecular force exerted on particle i by particle j in the Cartesian coordinate direction l . An overall heat flux is calculated in the water volume using Equation (1.8) by considering the contributions of each atom within a water molecule.

1.4. Objective of the Thesis

The aim of this thesis is to fill the gap in the literature by characterizing the nanoscale heat transfer mechanisms and provide a smart thermal management concepts for micro/nanoscale systems with high heat dissipations. Particularly, this study focuses on characterizing interfacial thermal resistance which classical continuum theories are incapable of capturing. Due to the significant contribution of interfacial thermal resistance to the total thermal resistance at nanoscale, heat transport has substantial growth capacity if the interfacial thermal resistance can be controlled. There are two significant outcomes of the literature. First, the literature mostly studied the dependence of ITR onto the material or surface properties at the interface. However, the properties of the phonon package are also expected to strongly influence the ITR, since reducing the nano-film thickness results in different phonon spectrums developing inside the sample as a function of thickness. Second, manipulation of surface wetting was conceived as the most effective way to control ITR. Increased wetting ability effects the solid/liquid coupling at the interface by creating liquid layering near the surface at nanoscale. Due to the increased coupling, the heat transfer rate is enhanced as well by the reduction in ITR. Consequently, the motivation of this study becomes to characterize the heat transfer mechanisms at nanoscale by investigating the parameters that influences ITR, which are nano-film thickness and enhanced surface wetting through electric field applications, and control ITR to control heat transfer by employing Molecular Dynamics studies.

This dissertation is divided into six chapters. In the following chapter (Chapter 2), effect of nano-film thickness on the interfacial thermal resistance is presented along with the density and temperature distributions of silicon/water couple. In Chapter 3, heat transfer control by the surface wetting boost through uniform electric field in the surface normal direction between silicon and water molecules is demonstrated. Moreover, how electric field effects the dielectric water molecules to align them in the electric field direction and alter its thermal conductivity is documented. In Chapter 4, difference between the effects of uniform and non-uniform electric field on both water molecules and interfacial thermal resistance is described. Furthermore, local heat transfer control through liquid dielectrophoresis is introduced to the literature with significant reduction in interfacial thermal resistance. In chapter 5, on the contrary to the previous chapter, liquid dielectrophoresis phenomenon is used to control the heat transfer throughout the interface with using interdigitated electrodes and ultra-low Kapitza length values ($\sim 0\text{nm}$) are achieved everywhere in the channel. Finally, the summary of the dissertation is presented in Chapter 6.

CHAPTER 2

EFFECT OF NANO-FILM THICKNESS ON THERMAL RESISTANCE AT WATER/SILICON INTERFACE

One of the most known nanoscale size effect is the decrease of solid thermal conductivity by decreasing length (Asheghi et al., 1998, Ju et al., 1999, Schielling et al., 2002, Liu et al., 2004, Sellan et al., 2010, Ma et al., 2012, Dong et al., 2014). When the nano-film thickness becomes shorter than the bulk value of the phonon mean free path (MFP), heat conduction is no longer carried out only by diffusive transport, it includes ballistic transport as well. In the ballistic transport, the spectrum of heat-carrying phonons inside the solid domain develops different than the bulk phonon propagation, and the resulted thermal conductivity decreases. Even though decrease in the effective thermal conductivity by the alteration of the phonon spectrum can be a challenge for the heat removal in the nano-systems, it can also be an interesting tool for heat transfer control by the so-called phonon engineering.

Another size effect on heat transfer comes from the increasing number of interfaces and their influences. Heat transfer between two dissimilar materials at nanoscale is greatly reduced due to the interrupted crystalline lattices between the materials, which interrupts phonon propagation and leads to phonon scattering. Such difficulty of phonon passage causes a temperature jump at the interface and it is characterized by the interface thermal resistance (ITR) which becomes the most dominant mechanism by the increase of surface-to-volume ratio. The literature mostly studied the dependence of ITR onto the material or surface properties at the interface. However, the properties of the phonon package are also expected to strongly influence the ITR, since reducing the nano-film thickness results in different phonon spectrums developing inside the sample as a function of thickness. Hence, ITR cannot be a material property only, but also should be affected by the size of the material. Such behavior is studied for solids made of grains smaller than their bulk phonon MFP that grain size dependency of ITR between solid/solid interfaces are examined before (Chang et al., 2012, Merabia and Termentzidis 2012, Jones et. al 2013, Meier et al., 2014, Yang et. al 2014 and Tao et al.,

2017). However, the size dependency of ITR at solid/liquid interfaces has been overlooked in the literature.

The objective of this chapter is to examine the heat transfer through the interface between water and silicon nano films of different thicknesses and different surface wettings. Additionally, ITR will be correlated with the thermal conductivity of corresponding silicon film and describe the influence of phonon scattering on both solid and interface thermal transport.

2.1. Simulation Details

Simulation domain consists of water confined between two silicon walls as illustrated in Figure 2.1. The silicon wall length is varied and performed measurements only on the one side while keeping the other side constant due to the computational limitations. Non-equilibrium Molecular Dynamics (NEMD) simulations are conducted with the LAMMPS (Large-scale Atomic/Molecular Massively Parallel Simulator) software. Cross sectional area of the computational domain was $3.8 \times 3.8 \text{ nm}$ in the vertical and lateral directions, where periodic boundary conditions were applied. In the longitudinal direction, thickness of the silicon (t) was varied from 5nm to 60nm while (0,0,1) crystal plane was facing the fluid. Simulated domains were very large for a classical MD simulation and required extensive computational sources and time.

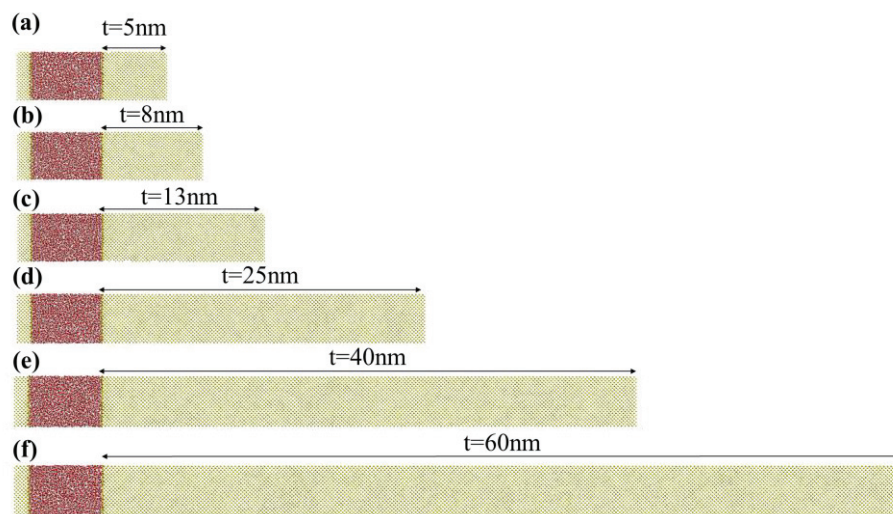


Figure 2.1. Simulation domains with different silicon thicknesses (a) 5nm, (b) 8nm, (c) 13nm, (d) 25nm, (e) 40nm and (f) 60nm.

Water density was kept at 1.006 g/cm³. SPC/E water model composed of Lennard-Jones and Coulombic potentials is used (Berendsen, 1987) with SHAKE algorithm to constrain the bond lengths and angles of this rigid model. Stillinger-Weber potential is used for the Si-Si interactions, which considers two-body interactions with an additional many-body dependence (Stillinger and Weber, 1985). The molecular interaction parameters for each molecule pair used in the simulations are given in Tables 2.1 and 2.2.

Table 2.1. Molecular interaction parameters used in the current study

Molecule Pair	σ (Å)	ϵ (eV)	q (e)
O-O	3.166	0.006739	-0.8476
H-H	0	0	+0.4238
Si-Si	2.095	2.168201	0

Table 2.2. Interaction strength values between Silicon and Oxygen

Molecule Pair	$\epsilon_{Si-O} / \epsilon_{Si-O}^*$	ϵ_{Si-O} (eV)
	1	0.12088
Si-O	0.4	0.048352
	0.125	0.015

For the silicon-oxygen interactions, parameters can be calculated by the Lorentz-Berthelot (L-B) mixing rule by

$$\sigma_{Si-O} = \frac{\sigma_{Si-Si} + \sigma_{O-O}}{2}, \epsilon_{Si-O} = \sqrt{\epsilon_{Si-Si} \times \epsilon_{O-O}} \quad (2.1)$$

Using the corresponding parameters given in Table 2.1, the L-B mixing rule predicts the interaction parameters $\sigma_{Si-O}^* = 2.6305 \text{ \AA}$ and $\epsilon_{Si-O}^* = 0.12088 \text{ eV}$. However, in an earlier wetting study based on MD, measured the contact angles of water nano-droplets, which showed that experimentally measured hydrophobic behavior of silicon surfaces can be recovered when the silicon-oxygen interaction strength is 12.5% of the value predicted using the Lorentz–Berthelot mixing rule (Barisik and Beskok, 2013). For such a case, this interaction strength value and further varied interaction strengths (0.125, 0.4 and unity ϵ_{Si-O}^*) are employed in order to examine the effect of varying surface wetting.

Atoms in the outmost layer of both Silicon walls are fixed to their original locations to maintain a fixed volume system, while the remaining atoms throughout the domain are free to move. A particle-particle particle-mesh (PPPM) solver which can

handle long-range Coulombic interactions for periodic systems with slab geometry is used. SPC/E water molecules interact with silicon surface only by van der Waals interactions of silicon and oxygen. By using the Verlet algorithm with a time step of 0.001 ps, Newton's equations of motion were integrated. Simulations were started from the Maxwell-Boltzmann velocity distribution for all molecules at 300K, while NVT ensemble was applied with Nose Hoover thermostat keeping the system at 300K. To reach an isothermal steady state, initial particle distribution was evolved 3×10^5 time-steps (0.3ns). Afterwards, the Nose Hoover thermostat was applied only on the outmost six layers of both silicon slabs on the left and right, while the remaining silicon and water molecules in between were free from thermostat at NVE ensemble. The outmost silicon layers on both sides kept at different temperatures to induce heat flux through the thermostat free liquid/solid interfaces. Simulations were performed for an additional 5×10^6 time-steps (5ns) to ensure that the system attains equilibrium in presence of the heat flux. The computational domain was divided into 100 slab bins with the size of 0.1343nm for temperature profiles. Smaller bin size, 1200 slab bins with the size of 0.0113nm, was also employed in order to resolve the fine details of the near wall water density distributions. Time averaging of desired properties are performed through 24×10^6 additional time steps (24 ns).

2.2. Results and Discussion

Due to the decreasing film thickness, the phonon spectrums developed inside those substrates' changes (i.e., MFP of the heat carrier phonons are reduced to the length scale of the nano-film). Based on this different phonon spectrums, the phonon scattering mechanism at the interface of the corresponding silicon nano-films and water also changes, which means the heat transfer through interface should be affected as well. In this study, the effect of nano-film thickness to the ITR is investigated with the sandwich structures presented in Figure 2.1. For such purpose, temperature distributions for each system size are obtained by applying hot and cold reservoirs to the two ends of the systems as shown in Figure 2.2. While the temperatures of the cold reservoirs are kept at 200K, the temperature of the hot reservoirs are varied between 548K and 595K for different system sizes, in order to keep the temperature at the silicon/water interfaces

constant at 490K for each system size. Such an action took place, because the ITR is also dependent on the surface temperature (Barisik and Beskok, 2014) and any variation on ITR caused by this effect is tried to be eliminated.

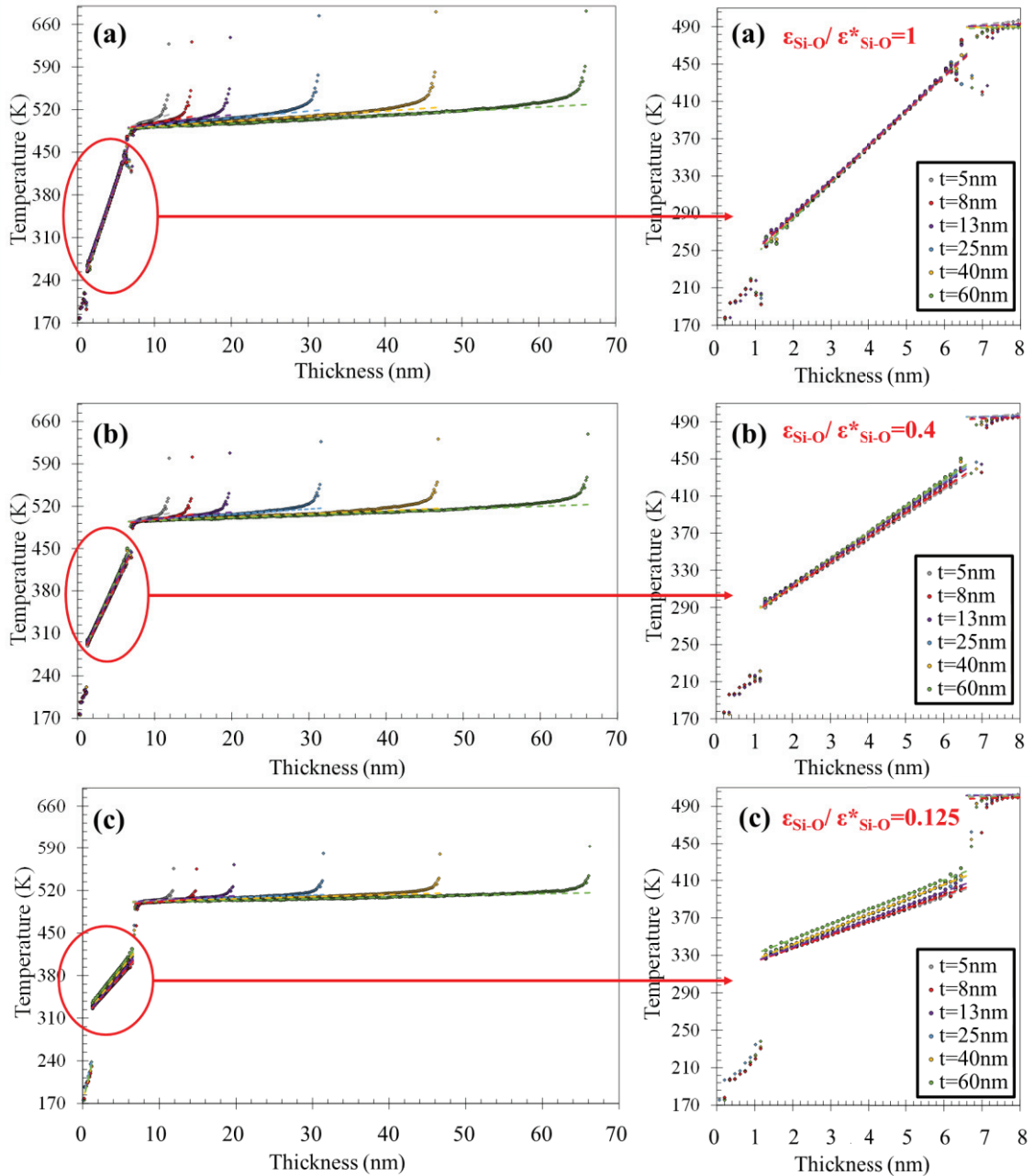


Figure 2.2. Temperature distributions of the systems with nano-film thicknesses of 5, 8, 13, 25, 40 and 60nm with (a) $1.0 \times \epsilon^*_{\text{Si-O}}$, (b) $0.4 \times \epsilon^*_{\text{Si-O}}$ and (c) $0.125 \times \epsilon^*_{\text{Si-O}}$

In the silicon domain, temperature drops are observed at the interfaces of thermostat applied regions and thermostat free regions. These temperature drops are caused by the phonon mismatches at the interfaces, which are the results of dynamic rescaling of the thermostats (Barisik and Beskok, 2014). In the thermostat free regions,

different temperature profiles are created by silicon molecules, which are interacting freely based on their phonon characteristics. As silicon nano-film thickness gets smaller the temperature gradient gets steeper, which is the result of decreasing thermal conductivity as a function of nano-film thickness. The temperature profiles sufficiently away from the interfaces are linear, which suits the Fourier's Law. However, non-linear temperature profiles are observed in the regions close to the interfaces. Non-continuum region close to the silicon/water interface tends to extend from the interface between 0.8nm and 1.3nm for two extreme cases. Furthermore, these regions extend from the applied thermostat interfaces from 0.6nm to 14.2nm, for silicon nano-film thicknesses 5nm to 60nm, respectively. Such behaviors indicate the phonon scattering mechanisms from the interfaces. Although the non-linear regions (i.e., silicon/water interface and silicon/thermostat interface) are approximately the same when the nano-film thickness is 5nm, the difference in the extents of these non-linear regions increases drastically when the system size is increased.

Thermal conductivity of silicon nano-film is determined by using direct method (Sellan et al., 2010). In the direct method, the heat flux, q , induced by the hot and cold reservoirs and the resulting temperature gradient, $\partial T/\partial z$, are calculated as documented in the previous sections. Finally, by using Fourier's Law of heat conduction, the thermal conductivity is calculated with following relation,

$$k = \frac{q}{\partial T/\partial z} \quad (2.2)$$

Calculated thermal conductivities with corresponding nano-film thicknesses are documented in Figure 2.3. As shown in Figure 2.3, thermal conductivity decreases with decreasing nano-film thickness and shows a good agreement with the literature (Sellan et al., 2010). In addition, thermal conductivity shows a non-linear relation with nano-film thickness, as the thickness gets smaller the thermal conductivity decreases even more. This non-linear behavior occurs since, in the ballistic transport, thermal transport contribution of the phonons whose MFP's are reduced to the length scale of the nano-film decreases drastically with the decreasing thickness.

We further adopted the theoretical model suggested by Sellan et al., which is based on Boltzmann transport equation and the Matthiessen rule to describe the size dependency of the thermal conductivity (Sellan et al., 2010). According to their model, there is a linear relation between $1/k$ and $1/t$. However, the function that correlates k and

t is unknown. So, they suggested to apply linear fit to their thermal conductivity measurements and extrapolate it the bulk. At the end of the process, they obtained the following relation,

$$\frac{1}{k} = \chi \left(\frac{1}{t} \right) \quad (2.3)$$

where χ was defined as an unknown function of $1/t$ that converges to $1/k_{\text{Bulk}}$ as $1/t$ goes to 0. This function was calculated using Taylor-series expansion, while the higher order terms were approximated to $1/k_{\text{Bulk}}$ after the first order term. Equation (2.3) is applied onto the results presented in Figure 2.3 and obtained the following semi-theoretical and empirical model for length dependent conductivity as,

$$\frac{1}{k} = 0.43 \frac{1}{t} + \frac{1}{k_{\text{Bulk}}} \quad (2.4)$$

where k is the thermal conductivity, k_{Bulk} is the bulk thermal conductivity, t is the thickness of the slab and (the bulk thermal conductivity of silicon at 500K is taken as 93 ± 18 W/mK (Sellan et al., 2010)). The dashed line given in Figure 2.3 represents the model derived by Sellan et al.,

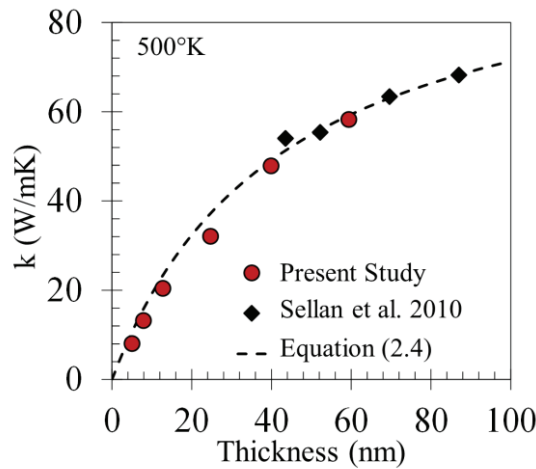


Figure 2.3. Thermal conductivity of silicon varying with nano-film thickness

In the water domain, temperature profiles are linear except the near wall regions, where temperature profile fluctuates due to the density layering created by the surface forces. This density layering is a function of surface wettability and has a strong impact on ITR (Barisik and Beskok 2014). The closer views of the near surface water density layering at different surface wetting conditions are given in Figure 2.4. The water penetrates in between the first and second silicon layers and the density in these regions decrease with the decreasing $\epsilon_{\text{Si-O}}$, which results in a weaker coupling between the water

and silicon and increase in the ITR. Additionally, these density profiles are document for systems with different nano-film thicknesses. Results show that the near wall density profiles do not depend on the nano-film thickness. Thus, any variation in ITR depending on the nano-film thickness cannot be explained with the density layering of the solid/liquid couple. In addition, water density reaches its bulk value of 1.006 g/cm³, in all cases.

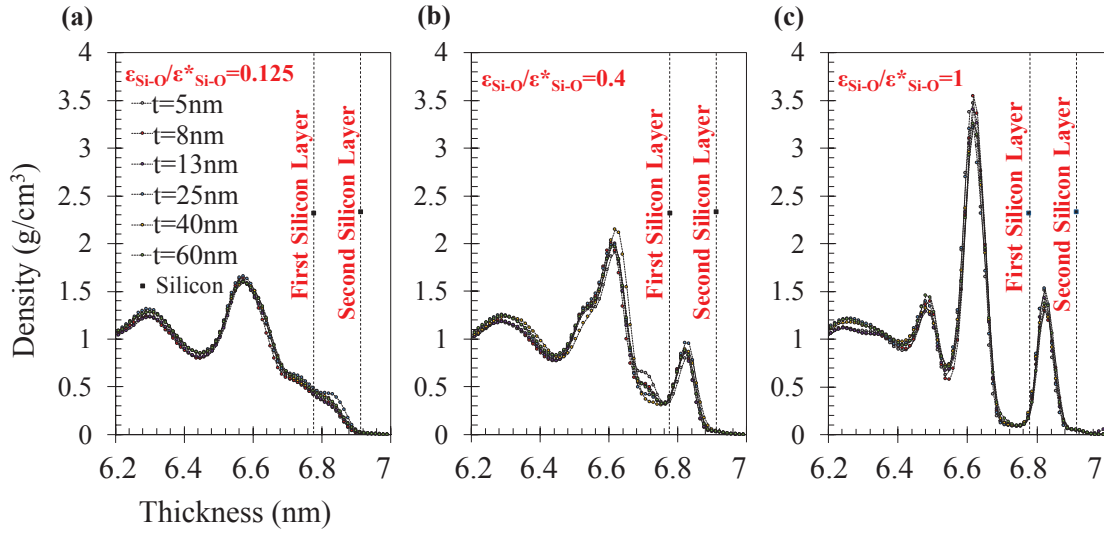


Figure 2.4. Near wall density profiles of different nano-film thicknesses at different interaction parameters of (a) $0.125 \times \epsilon^*_{\text{Si-O}}$, (b) $0.4 \times \epsilon^*_{\text{Si-O}}$ and (c) $1 \times \epsilon^*_{\text{Si-O}}$

Temperature jumps at the silicon/water interface are measured for various size silicon systems and wetting conditions. The mismatch in the phonon spectrum of silicon and water pair creates this temperature jump which can also be characterized by Kapitza Length (L_K) as in equation (2.5).

$$\Delta T = L_K \left. \frac{\partial T}{\partial n} \right|_{\text{liquid}}, \quad (2.5)$$

where $\partial T/\partial n$ is the temperature gradient of the liquid and ΔT is the temperature jump at the liquid/solid interface. Kapitza length values of different nanofilm thicknesses for different surface wettings are documented in Table 2.3.

Table 2.3. Kapitza length values measured at different nanofilm thicknesses and at different surface wettings.

Thickness (nm)	Kapitza Length (L_K) (nm)		
	$\epsilon_{Si-O} / \epsilon^*_{Si-O} = 0.125$	$\epsilon_{Si-O} / \epsilon^*_{Si-O} = 0.4$	$\epsilon_{Si-O} / \epsilon^*_{Si-O} = 1$
5	7.158	2.394	0.926
8	6.612	2.199	0.853
13	6.290	2.053	0.828
25	5.375	1.939	0.775
40	5.304	1.801	0.725
60	4.996	1.799	0.700

Thermal resistance values at the interface of silicon/water pair depending on surface energy and nano-film thicknesses are plotted in Figure 2.5, in terms of Kapitza Length. In Figure 2.5(a), Kapitza Length increases with decreasing interaction strength ϵ^*_{Si-O} , due to the weakening coupling between water and silicon pairs, which is in accordance with the near wall density profiles documented in Figure 2.4. Moreover, by decreasing the interaction strength transition from hydrophilic to hydrophobic silicon surface can also be observed in Figure 2.5(a). Finally, thermal resistance at the interface of water and silicon nano-films with different thicknesses are documented in Figure 2.5(b). The thermal resistance length of each nano-film thickness is normalized with the L_K of the structure with 60nm nano-film thickness, which has the lowest thermal resistance among them and represents the thermal resistance of the bulk silicon. As shown in Figure 2.5(b), heat transport at the water/silicon interface shows strong dependence on the nano-film thickness. It is observed that the ITR in terms of normalized Kapitza Length increases exponentially by the decrease in nano-film size. In an attempt to characterize the observed variation, we applied a mathematical fit (equation 2.6) to the normalized Kapitza length values, with an R^2 value of 0.9. A similar size dependency of thermal resistance on solid/solid interface has been reported, previously (Liang et al., 2014, Y. Tao et al., 2107). Moreover, variation of normalized L_K by the change of film thickness is found independent from surface energy. This behavior proves that any variation in the ITR by changing the nano-film size is caused by the variation in phonon scattering at the interface caused by the phonon spectrums developed inside nano-films with different thicknesses. Furthermore, L_K values predicted with the exponential model, shows an

agreement with the model generated by Barisik et al., when the correct nano-film thickness and surface temperature is inserted (Barisik and Beskok 2014). The error in L_K between the two models is 18% when the nano-film thickness is selected as 3.5nm and the surface temperature as 490K.

$$\frac{L_K}{L_{K-Bulk}} = \exp\left(\frac{1.7}{t}\right) \quad (2.6)$$

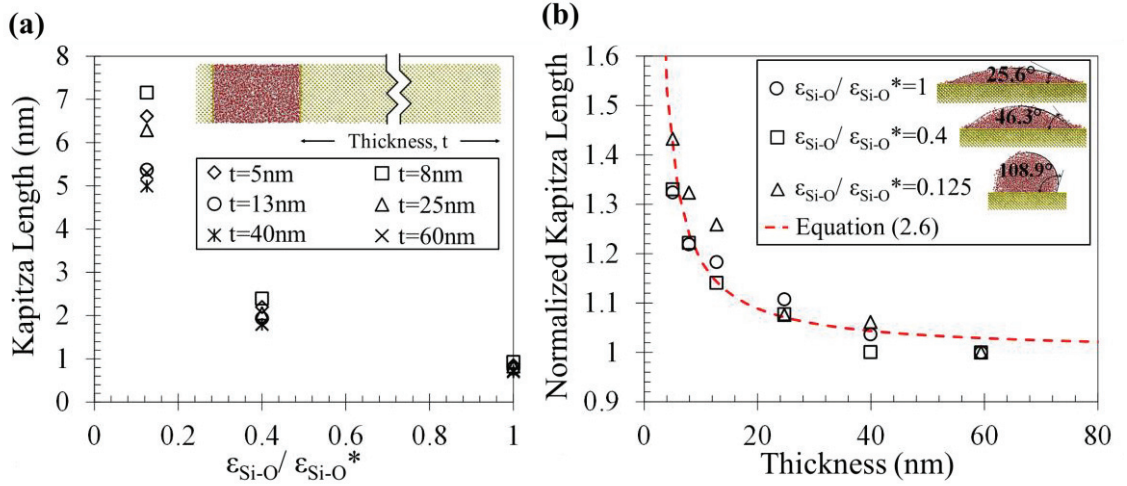


Figure 2.5. (a) Variation of Kapitza Length by interaction strength. (b) Variation of Kapitza Length normalized with bulk L_K (60nm nano-film) by nano-film thickness.

Since the observed behavior and developed model as a function of slab thickness is specific for the silicon/water couple, further characterizations are conducted by correlating the L_K with the corresponding thermal conductivity. To achieve this, the thermal conductivity model as a function of nanofilm thickness derived by Sellan et al., is integrated into the current mathematic model, which describes the variation of L_K with respect to nanofilm thickness (Sellan et al., 2010). Along with the normalized L_K values at their corresponding normalized thermal conductivities, Figure 2.6 presents the present empirical model (equation 2.7), in which they agree perfectly.

$$\frac{L_K}{L_{K-Bulk}} = \exp\left(\frac{3.94}{k_{Bulk}} \left(\frac{k_{Bulk}}{k} - 1\right)\right) \quad (2.7)$$

In Figure 2.6, it is observed that the change in phonon characteristics creates effects at different levels; the increase rate of L_K from its bulk value is much higher than decrease rate of conductivity from its bulk value. Decrease in length scales develops different effects in phonon dynamics of different materials, but variation in phonon

distribution shows itself through the variation of conductivity. Also, the size dependent behavior of L_K is independent from surface wetting that effect of altered phonon dynamics on L_K can directly be predicted from the variation in thermal conductivity. Such perspective will also be valuable since the thermal conductivity as a function of size is available for several materials that L_K can be easily calculated from them using proposed model.

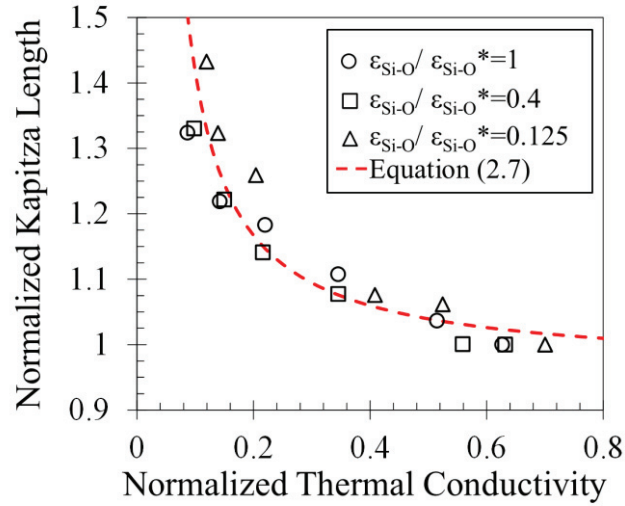


Figure 2.6. Variation of Kapitza Length normalized with bulk L_K (60nm nano-film) by thermal conductivity normalized with bulk k (Sellan et al., 2010)

2.3. Conclusion

In summary, thermal resistance across the interfaces of water and silicon nano-films with different thicknesses are investigated through MD simulations. Same factor that creates a size dependency on thermal conductivity also creates size dependency on ITR, which is different phonon spectrums developed inside various silicon nano-film thicknesses. Results show the interface thermal resistance between a liquid and solid is dominated by the thickness of the solid, due to the phonon MFP's are reduced to the solid size, hence phonons passing through the interface become different. In addition, ITR is strongly dependent on the surface energy, in other words, surface wettability. However, normalized behavior of the thermal resistance by the change of film thickness is found independent from the wetting angle. Based on the MD measurements, a phenomenological model is developed which successfully predicted L_K values from

another study. Finally, the increase of L_K is correlated with the decrease of thermal conductivity which can provide L_K values for the cases where thermal conductivity of nano-slab is known. Results and size dependency model of the ITR provided from this study are essential for designing heat removal mechanisms at nano-scale systems.

CHAPTER 3

ELECTRIC FIELD CONTROLLED HEAT TRANSFER THROUGH SILICON AND NANO-CONFINED WATER

Heat transfer control is crucial for applications where the aim is keeping temperature of the devices at desired conditions such as, thermal management of the processors (Didion, 2015) and the batteries of electric vehicles (Smith et al., 2018). Furthermore, with decrease in size heat transfer control of the micro/nano devices becomes the limitation to the further developments in the field. Consequently, researchers focus on developing new smart materials to control heat transfer at micro/nanoscale, such as employing thermal interface materials as a bridge to heat sinks (Razeeb et al., 2017), tailoring nanostructures to manipulate the phonon dynamics of the materials (Li et al., 2017, Nomura et al., 2018) or employing superbiphilic surfaces to both increase the convective and conductive heat transfer (Betz et al., 2013). However, recent technologies require more sophisticated, active control techniques for need-based heat transfer.

One of the major active heat transfer control techniques emerged from the use of an electric field to manipulate the solid and/or liquid domains, and their interface couplings. Also known as electrowetting, interface energy between solid and liquid can be actively controlled by an electric field (Mugele and Baret, 2005). Electrowetting-on-dielectric (EWOD) is its main application where the electrodes are covered by a dielectric layer acting as a capacitor. Variation of wetting angle as a function of applied electric field was examined theoretically by the Lippmann–Young equation (Daub et al., 2006, Orejon et al., 2013). In the literature, it is repeatedly shown that one of the most effective way to alter heat transfer rate at nanoscale is the manipulation of the surface wettability. Barisik et al., showed that how increased wetting ability effects the solid/liquid coupling at the interface by creating liquid layering around the surface at nano-scale (Barisik et al., 2013). Due to the increased coupling, the heat transfer rate is enhanced as well by the decrease of the interfacial thermal resistance (ITR) (Barisik et al., 2014). Multiple studies were dedicated to characterizing the effect various forms of surface modifications such as surface patterning (Liang et al., 2014, Hong et al., 2015), surface conditions (Liu et al., 2016), coating material (Pham et al., 2016, Nobakht and Shin 2016, Zhang et al., 2017)

and thickness of solid coating (Yenigun and Barisik 2019); which provide a passive ITR control. Instead, coupling at the liquid solid interface can be actively controlled using an electric field.

In this chapter, non-equilibrium molecular dynamics (NEMD) simulations are used to investigate heat transfer control of the water confined between silicon slabs under varying electric field. This study documents the resulting temperature and density profiles, thermal conductivity, interfacial thermal resistance in terms of Kapitza Length and the total heat flux of the system after carefully fixing the thermodynamic state.

3.1. Simulation Details

Water confined between two silicon slabs was simulated as illustrated in Figure 3.1. Cross sectional area of the computational domain was 3.8×3.8 nm in the surface parallel directions where periodic boundary conditions were applied. The distance between 5.4nm thick silicon slabs was 5.7nm and (0,0,1) crystal plane was facing the fluid. Non-equilibrium molecular dynamics (NEMD) simulations were performed with LAMMPS (Large-scale Atomic/Molecular Massively Parallel Simulator) algorithm.

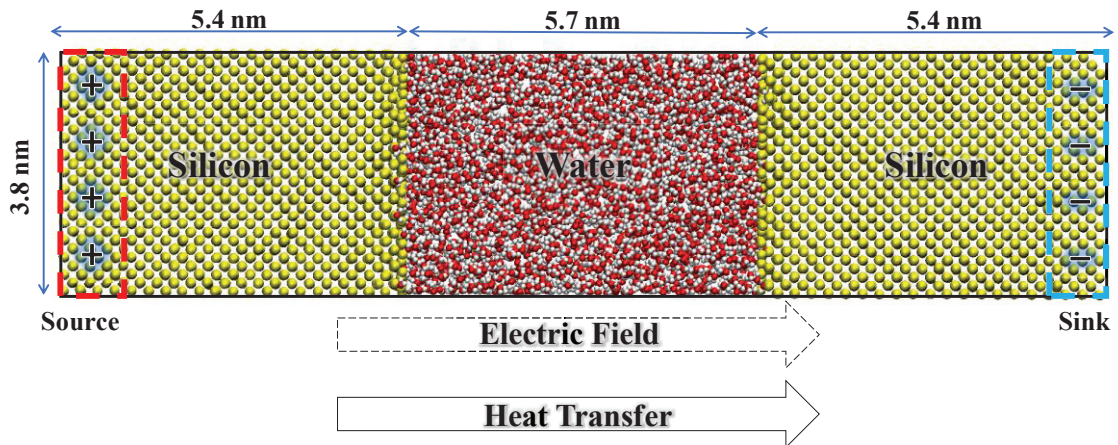


Figure 3.1. Simulation domain for silicon water system under uniform electric field

SPC/E water model composed of Lennard-Jones and Coulombic potentials is used (Berendsen et al., 1987) with SHAKE algorithm to constrain the bond lengths and angles of this rigid model. Stillinger-Weber potential is used for the Si-Si interactions, which considers two-body interactions with an additional many body dependence (Stillinger et al., 1985). Interactions between water and silicon also calculated by the combined

Lennard-Jones and Coulombic potentials. Parameters for the interactions between similar molecules such as O-O and Si-Si were taken from the corresponding models. However, the parameters determining the interactions of the specific liquid/solid couples are still under investigation. Frequently, interaction parameters for dissimilar molecules are frequently calculated using simple mixing rules as a function of parameters of the pair of identical molecules. However, the interaction parameters between identical molecules are optimized for a bulk material system that parameters calculated based on a mixing rule cannot recover the correct behavior at the given solid/liquid interface. In our earlier wetting study based on MD, measured contact angles of water nano-droplets showed that experimentally measured hydrophobic behavior of silicon surfaces can be recovered when the silicon-oxygen interaction strength is 12.5% of the value predicted using the Lorentz–Berthelot mixing rule (Barisik et al., 2013). Hence, we employed this interaction strength value in the current study. The molecular interaction parameters for each molecule pair used in the simulations were given in Table 3.1.

Table 3.1. Molecular interaction parameters used in the current study

Molecule Pair	σ (Å)	ϵ (eV)	q (e)
O-O	3.166	0.006739	-0.8476
H-H	0	0	+0.4238
Si-Si	2.095	2.168201	0
Si-O	2.6305	0.01511	Varies

Atoms in the outmost layer of both silicon slabs are fixed to their original locations to maintain a fixed volume system, while the remaining atoms throughout the domain were free to move. The fixed outmost silicon layers were selected as electrodes to apply equally distributed charge per molecule. Negative and positive charges with equal absolute value were assigned at the electrodes of right and left side. A uniform electric field develops in surface normal direction. Applied surface charge densities were varied between 0.05 and 0.6 C/m², which resulted in electric fields strengths varying between 0.09 and 0.96 V/nm, similar to earlier MD studies (Luedtke et al., 2011, Yen et al., 2012, Yan and Patey 2012, Celebi et al., 2017). Although applied electric fields seems high for experimental studies, it is not totally impractical (Wei et al., 2008). For example, the pulse discharge method engages pulse voltages through two electrodes in an aqueous environment to generate an electric field on the order of 1 V/nm (Braslavsky and Lipson 1998, Sunka 2001, Wei et al., 2008) similar to studied electric field strengths.

The particle-particle particle-mesh (PPPM) solver was used to calculate long-range Coulombic interactions of the periodic slab system. By using the Verlet algorithm with a time step of 0.001 ps, Newton's equations of motion were integrated. Simulations were started from the Maxwell-Boltzmann velocity distribution for all molecules at 323K, while NVT ensemble was applied with Nose Hover thermostat keeping the system at 323K. To reach an isothermal steady state, initial particle distribution was evolved 2×10^6 time-steps (2ns). Afterwards, one dimensional heat transfer between silicon slabs was created using the Nose Hover thermostat applied only to the outmost six layers of the both silicon slabs. Left and right-side thermostats were maintained at 363K and 283K temperatures to induce heat flux through the liquid/solid interfaces. Such high temperature gradients can be developed by using the electron beam of a transmission electron microscope (Somada et. a. 2008) or the plasmonic nanoantenna in heat-assisted magnetic recording applications (Dieny et al., 2018, Jones et al., 2018). At the same time, NVE ensemble was applied to the remaining silicon and water molecules. Simulations were performed for an additional 15×10^6 time-steps (15ns) to ensure that the system attains equilibrium in presence of the heat flux and time averaging is performed after the equilibrium is achieved. The computational domain was divided into 124 slab bins with the size of 0.1343nm for temperature profiles. Smaller bin size, 1476 slab bins with the size of 0.0113nm, was also employed to resolve the fine details of the near wall water density distributions.

3.2. Results and Discussion

Uniform surface charges are introduced to the silicon layers at the water interfaces. Positive charge is applied on the left wall, representing anode and negative charge is applied on the right wall, representing cathode. Under these conditions, an electric field is created in the system from left to right. In Figure 3.2, temperature distributions of the system under electric field strengths of 0, 0.18, 0.35 and 0.79 V/nm are documented. Even though, the temperature of the thermostat applied regions are kept constant, a variation in the heat transfer rate is observed when electric field is applied. Temperature profiles are linear in the water domain except the very near wall regions, where temperature profile fluctuates due to the density layering created by the Van der

Waals force field of surface and the electric field. Furthermore, when the electric field strength reaches to 0.79 V/nm, a layering in the temperature profile is observed. Such behavior is expected, since amplitude of the electric field is enough to cause electro freezing (Luedtke et al., 2011, Yen et al., 2012, Yan and Patey 2012, Celebi et al., 2017). When electro freezing occurs, water molecules start forming an ordered structure. Due to this ordered structures, number of molecules fluctuate in every bin, because of the fine binning of the domain. However, if the average of every 4 bin is taken, a linear temperature profile is obtained, which is documented in Figure 3.2 with big yellow box markers. This means that Fourier's Law of heat conduction is still applicable. Furthermore, there is a jump between silicon and water temperatures at the interface due to the phonon mismatch. This is the well-known interfacial thermal resistance.

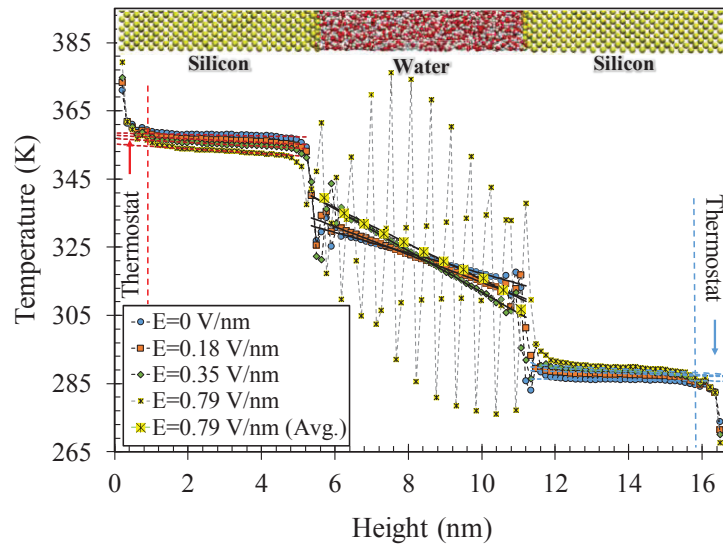


Figure 3.2. Temperature distributions at electric field strengths of 0, 0.35, 0.70 and 1.05 V/nm

Next, we studied the density distributions of water under different electric field strengths. In this study, electric fields are created in the range of zero to 0.96 V/nm and this range is divided into two, where they are going to be denoted as low and high electric field from now on. The high field denotes the range through which electro-freezing develops. In Figure 3.3, water density distributions at low electric field range varying between 0 to 0.40 V/nm were given. At near wall regions, increasing density layering as a function of wetting, which is promoted with increasing electric field exposure is observed, while the density reaches its thermodynamic value of 1 g/cm³ at the rest of the channel. Such behavior is expected, since promoting wetting with applying electric field is a well-known subject as electro-wetting (Braslavsky et al., 1998, Hu et al., 2012).

However, under oppositely charged walls, hydrogen molecules will turn and attracted towards cathode and oxygen molecules towards anode. For this reason, there is a non-symmetrical density distribution developed in the confined water. To detailly investigate differences between the density distributions under varying electric field, near wall density distributions are documented in Figure 3.4. In closer view, it is observed that with increasing electric field strength, near wall density layers are pulled towards the surface and the water molecules near the walls develop up to three density layers and penetrate between the first and second silicon layers in both walls. The nearest density peak and penetration increases by the increase of electric field strength. This can be also denoted as change of surface energy or surface wetting. By the increasing surface charges (i.e., increasing electric field strength) the number of molecules near wall regions increases, which enhances the interfacial energy of the initially hydrophobic silicon surface.

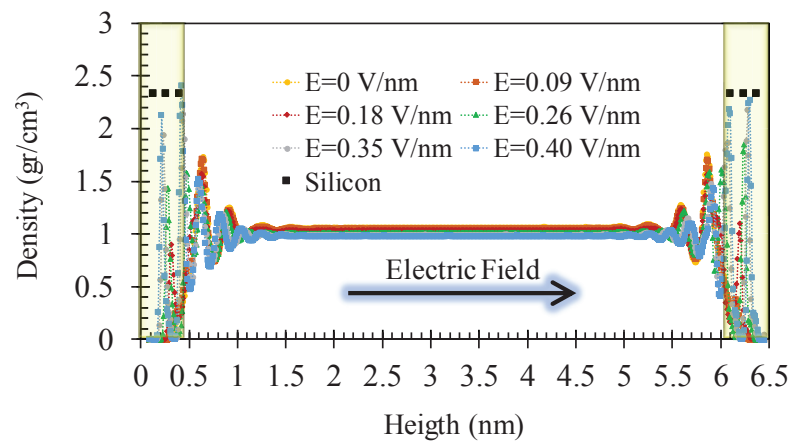


Figure 3.3. Water density distributions at different electric field strengths

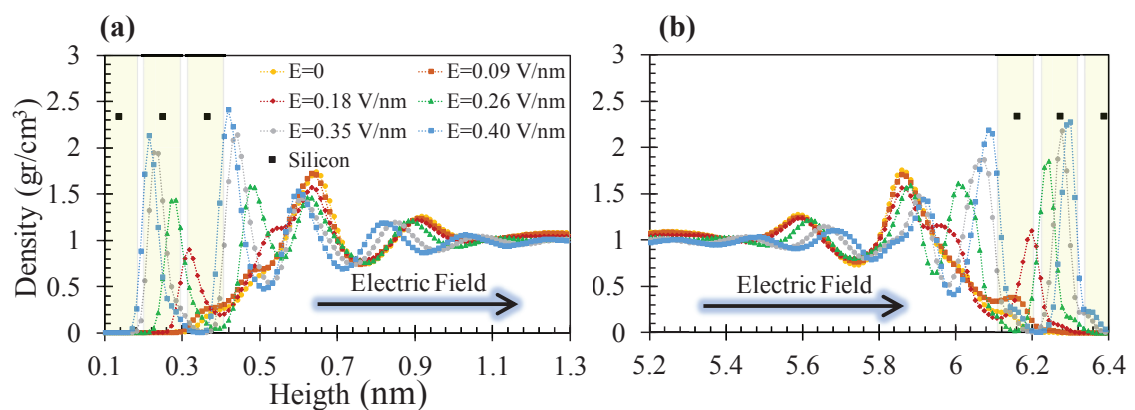


Figure 3.4. Water density distributions at different electric fields (a) near hot surface with positively charged electrode and (b) near cold surface with negatively charged electrode

Density distributions of water under high electric field range of 0.44-0.96 V/nm are given in Figure 3.5. Electro-freezing is first observed at 0.44 V/nm on the cold side of the water domain, partially. Since the phase transition of water can be shifted with electric field (Luedtke et al., 2011, Yen et al., 2012, Yan and Patey 2012, Celebi et al., 2017), it can be deduced that the applied electric field (0.44 V/nm) is able to shift solidification temperature up to a point, where it could not dominate the entire water domain. Specifically, temperature profile of 0.44 V/nm case shows that water temperature changes from 330K to 310K from left side to right side and the temperature of the location where electro-freezing starts is approximately 325K. Electric fields higher than 0.44 V/nm results in complete freezing of water that the whole water domain gets in solid like ordering. The closer view of the near wall water density distributions at high electric field range are given in Figure 3.6. Water density ordering is in transition at 0.53 V/nm, but water structure remains unchanged for higher field strengths.

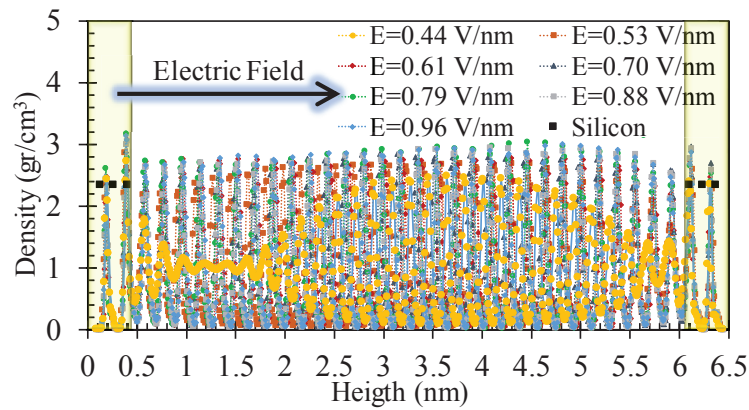


Figure 3.5. Density distributions of water under electric field varying from 0.44 to 0.96 V/nm

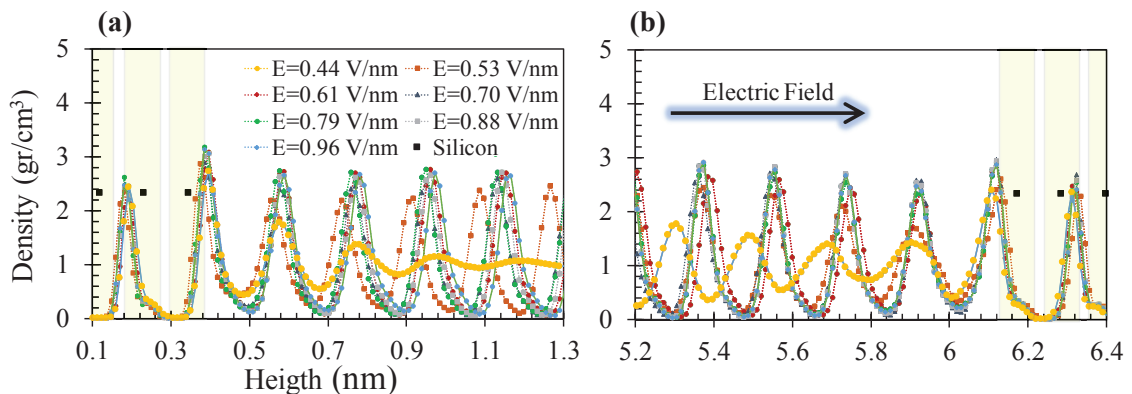


Figure 3.6. Water density distributions of high electric field range (a) near hot surface with positively charged electrode and (b) near cold surface with negatively charged electrode

Change of molecular orientations of the water molecules, under increasing electric field strengths are presented in Figure 3.7. Parallel to the density distributions showed in Figure 3.3 and 3.5, water molecules first got attracted to the silicon walls and penetrate between the first and second layer of silicon. Under specific boundary conditions, after reaching the electric field strength of 0.44 V/nm water molecules start to form hexagonal structure in some parts of the channel but not all, agreeing the with the Figure 3.5, where water density layering did not dominate the entire channel. However, after increasing the electric field strength even more, water molecules form perfect complete crystalline structure. Such crystalline structure formation is a result of electric field induced change in hydrogen bond network (Celebi et al., 2017). With strong electric field, random movements and hydrogen bond dynamics are drastically changed and got restricted. As a consequence, dipole moments are fully aligned through the electric field direction, hence perfect crystalline structure is developed as shown in Figure 3.7(f). These structures developed in the single crystalline form, except the case at electric field strength of 0.61 V/nm which created two grains with different crystal ordering. In order to observe the crystal structures, we rotated the systems to have best snapshot in Figures 3.7. Single crystalline structures can be easily seen in Figures 7(f), (i) and (j) while the view of both grains developed at 0.61V/nm are given in Figures 7(g) and (h).

A detailed characterization for crystalline planes observed were studied in Figure 3.8. Different views of the silicon/water domain at 0.88 V/nm are presented. Just simple three dimensional and side view given in Figures 3.8a and 3.8b presents the highly ordered water molecules. When the system is viewed at different angles a perfect (0,0,1) and (1,0,1) crystallographic ice planes can be observed in Figures 3.8c and 3.8d, respectively. This can validate the perfect crystalline structure as the results agree with the electro-freezing study of Yan and Patey (Yan and Patey 2012).

Next, we studied the water temperature profiles normalized with their average values under low and high electric field strengths in Figure 3.9a and Figure 3.9b, respectively. At low field range prior to electro-structuring, temperature profiles vary by applied electric field. Basically, the slopes of the temperature profiles are increasing with the increasing electric field while the temperature of the source and sink kept constant. However, temperature gradient of high electric fields cases stays constant by the increase of field strength while the same temperature difference is applied. For comparison reasons, we added low electric field case of 0.4V/nm (no freezing) in the Figure 3.9b.

After the electro-freezing developed at 0.44 V/nm case, temperature profiles of different electric fields are almost identical.

These changes in the temperature profiles are solely due to the altered total heat flux with the presence of electric field. In the current system, heat transfers components are composed of the thermal resistances to (i) heat transfer by conduction and (ii) heat transfer through interfaces. In the next sections, the variations in the thermal conductivity of water and interface thermal resistance by the applied electric field is studied.

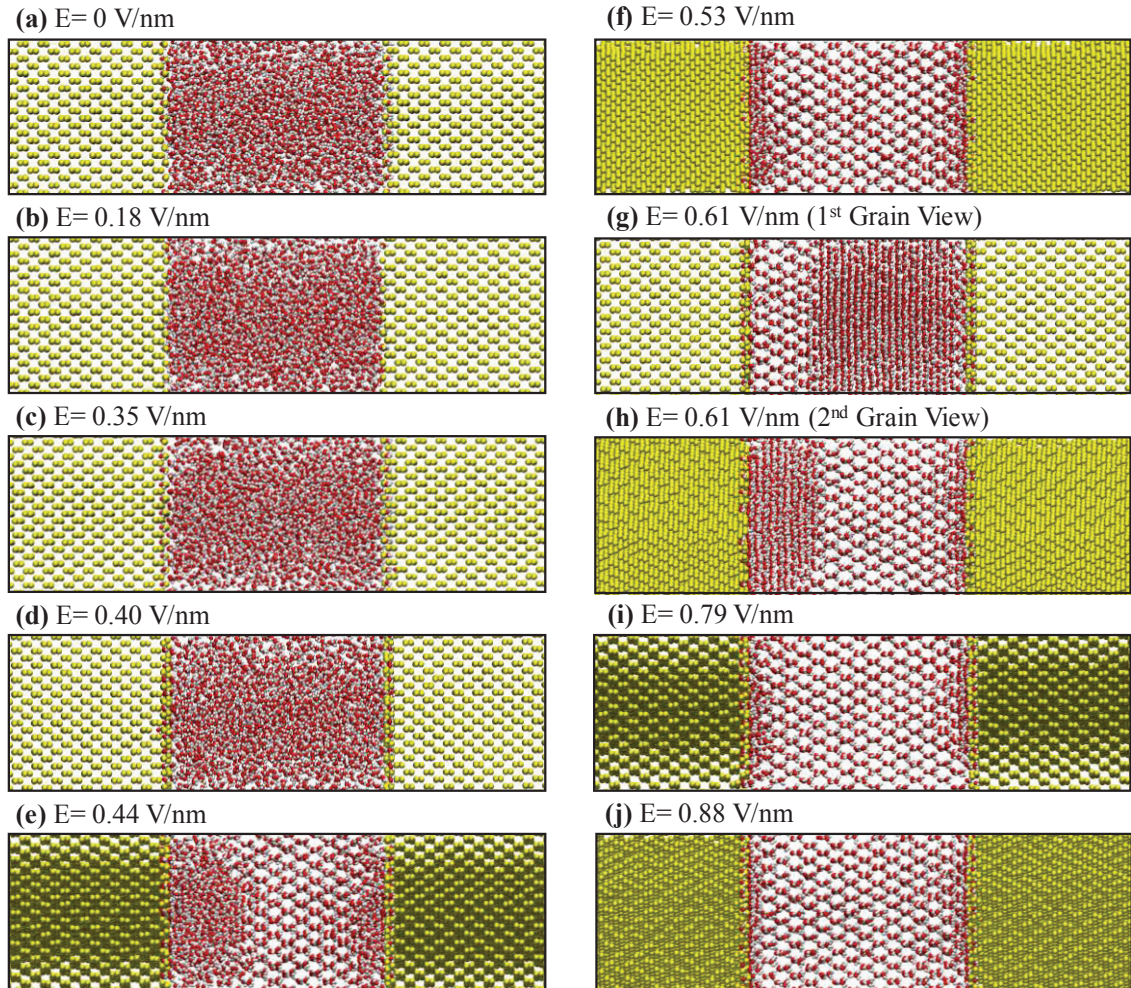
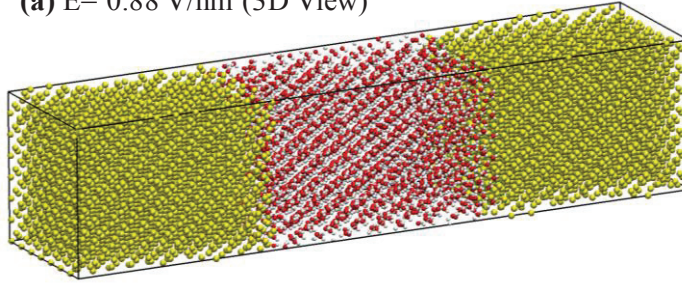
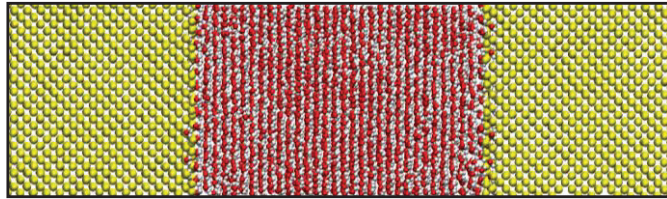


Figure 3.7. The snapshots of the silicon/water system at electric fields of (a) 0, (b) 0.18, (c) 0.35, (d) 0.40, (e) 0.44, (f) 0.53, (g) 0.61, (h) 0.61 (i) 0.79 and (j) 0.88 V/nm

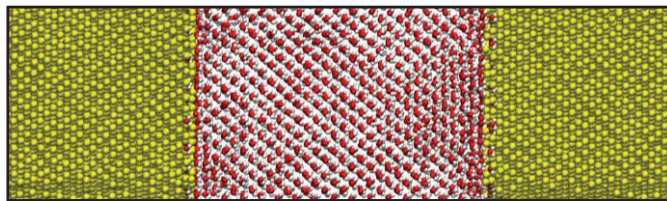
(a) $E= 0.88 \text{ V/nm}$ (3D View)



(b) $E= 0.88 \text{ V/nm}$ (Side View)



(c) $E= 0.88 \text{ V/nm}$ (Ice (0,0,1) View)



(d) $E= 0.88 \text{ V/nm}$ (Ice (1,0,1) View)

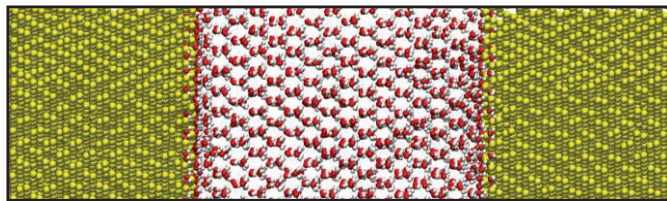


Figure 3.8. The snapshots of the silicon/water system under 0.88 V/nm electric field at (a) 3D view, (b) side view, (c) ice (0,0,1) view and (d) ice (1,0,1) view

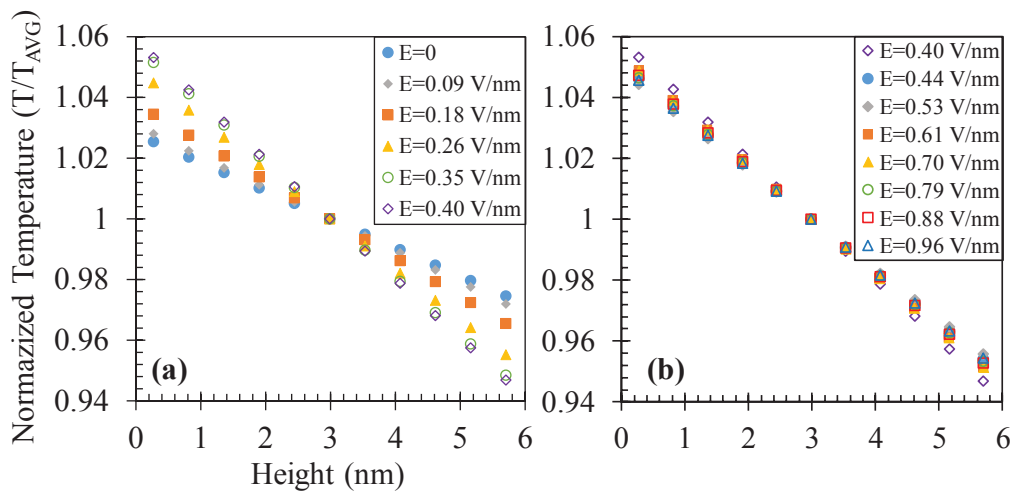


Figure 3.9. Normalized temperature profiles of water under electric fields varying from (a) 0 to 0.4 V/nm and (b) 0.4 to 0.96 V/nm

In Figure 3.10, the variations in the thermal conductivity of water and Kapitza length under different electric field strengths are presented. Since the temperature profiles of water are linear at the bulk region (Figure 3.9), Fourier's Law of heat conduction (Equation 2.2) is applicable to calculate the thermal conductivity of water. Thermal conductivity of water with SPC/E model is calculated as 0.82 W/mK at the average temperature of 325 K, when there is no electric field, which agrees with the literature (Mao and Zhang 2012). With increasing electric field, thermal conductivity of water slightly decreases with the increase of electric field strength in the low electric field range ($<0.44\text{V/nm}$). This is due to the restricted molecular diffusion and hydrogen bonding activities of water molecules under electric field. After reaching electric field strength of 0.44 V/nm, water molecules start forming crystalline structure as documented in Figure 3.7(e). Furthermore, due to water molecules having greater structural order, phonon transfer enhances, and thermal conductivity shows a sudden jump. Thermal conductivity of water increases 1.5 times when electric field strength reaches to 0.53 V/nm and then remains constant with the increased electric field, except 0.61 V/nm case, where thermal conductivity of water decreases. Interestingly, at electric field strength of 0.61 V/nm, perfect crystalline structure is disturbed (Figures 3.7(g) and (h)) and water molecules start forming multiple grain boundaries. Formation of multiple grain boundaries interrupts the phonon transfer, hence the thermal conductivity decreases.

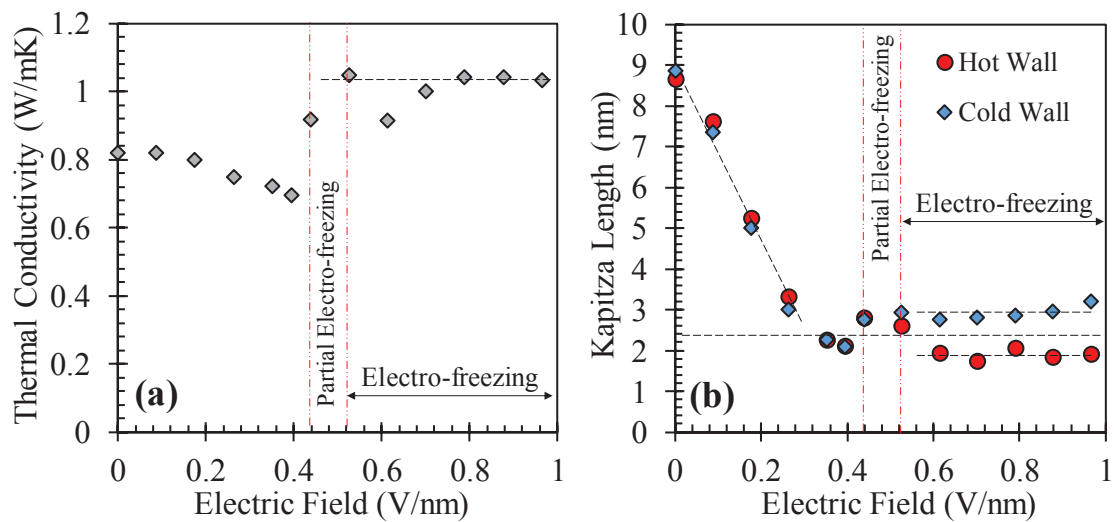


Figure 3.10. (a) Thermal conductivity of water and (b) Kapitza length as a function of electric field strength

Next, interface thermal resistances were characterized by calculating Kapitza lengths. Based on the temperature jump at the liquid/solid interfaces (ΔT) and the

temperature gradient of the liquids ($\partial T/\partial z$) documented in Figure 3.9, Kapitza length (L_K) values are calculated using equation 1.2. Results are documented in Figure 3.10(b) for both hot and cold surfaces. Interface thermal resistance is decreasing drastically with the increase of electric field strength. The increase in water density layering near the silicon walls by the increase in electric field documented in Figure 3.4, strengthens the solid/liquid coupling at the interface, thus decreases the interfacial thermal resistance. Minimum interface thermal resistance develops around 0.40 V/nm before electro freezing starts, in which L_K reduces up to 76% its original value. Furthermore, while the L_K on hot surface is lower than the L_K on cold side at the zero electric field case, L_K on hot side becomes higher than the cold side value through the low electric field range. Barisik and Beskok detailly described the temperature dependence of L_K at liquid/solid interface (Barisik and Beskok 2014). Simply, for hydrophobic surfaces, the temperature dependence of phonon dynamics determines the L_K variation by the temperature. On the other hand, for hydrophilic surfaces, variation of L_K by the temperature is dominated by the temperature dependence of liquid layering at near wall regions. So, in the low electric field range electric field alters surface wetting from hydrophobic to hydrophilic. Once the water molecules from crystalline structure, interfacial thermal resistance for both hot and cold surfaces slightly increase and then stay constant. At high electric field range, L_K values of hot and cold surfaces show a slight discrepancy. After electro-freezing took place, L_K values on the hot surface are measured lower than the L_K values on the cold surface. This behavior is in agreement with classical phonon theories of solids, where molecules with higher temperature have enhanced phonon activities. Thermal conductivities of silicon slabs are also measured for varying electric field intensities and showed no dependency on electric field while remaining constant around 9 W/mK.

The heat flux values for both low and high electric field ranges are given in Figure 3.11. Heat flux varies with the applied electric field, which changes the Kapitza length (i.e., interfacial thermal resistance) and water thermal conductivity. In an agreement with the increasing temperature gradient of the water molecules, the total heat flux increases with the increasing electric field intensity in low electric field region ($0 < E < 0.40$ V/nm). The drastic decrease in interfacial thermal resistance doubles the total heat flux compared to the zero electric field case, even though the thermal conductivity of water decreases slightly. Increasing the electric field intensity even further results in slight increase in the total heat flux until electro-freezing dominates the entire channel at 0.53 V/nm. The total heat flux reaches 2.25 times of zero-electric field value at 0.53V/nm and further increase

in the electric field intensity does not affect the total heat flux, since after perfect crystalline structure is achieved neither interface thermal resistance nor water thermal conductivity changes with the electric field strength.

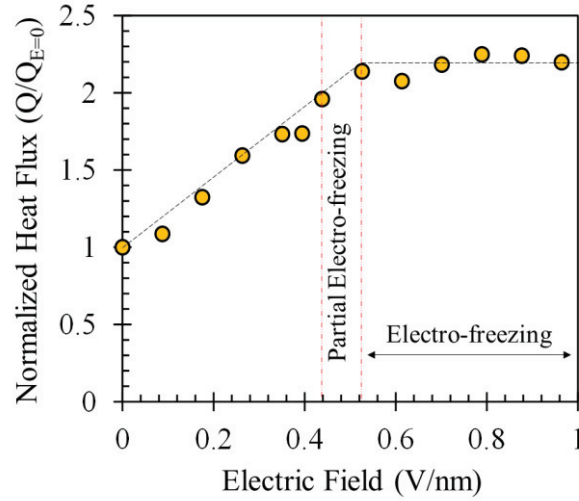


Figure 3.11. Total heat flux through the nano-confined water as a function of applied electric field strength

3.3. Conclusion

The manipulation of heat transfer through nanoscale fluidic systems through an applied uniform electric field is introduced and demonstrated. By applying uniform electric field in the surface normal direction, the total heat flux can be more than doubled. The resulting effects of electric field on the heat transfer mechanics are detailly characterized. Basically, dipole orientations of water molecules are altered by the electrostatic forces created with uniform electric field application. Consequently, as a function of electric field intensity, surface wetting and molecular distribution of water is shown to be controlled. Fundamentally, increasing the electric field intensity improves the solid/liquid coupling at the interface and reduces the interface thermal resistance substantially until electro-freezing occurs, after which it almost remains constant. On the other hand, increasing the electric field slightly decreases the thermal conductivity of water until the electro-freezing starts due to restrained molecular dynamics in the water domain. Once the electro-freezing occurs, water molecules possess greater structural order, which improves the phonon transfer, thus increases the water thermal conductivity. As a result of these phenomena, heat flux increases with the increase of electric field up

to full formation of electro-freezing. At a constant temperature difference, heat transfer rate increased 2.25 times from zero electric field to 0.53V/nm field strength.

CHAPTER 4

LOCAL HEAT TRANSFER CONTROL USING LIQUID DIELECTROPHORESIS AT GRAPHENE/WATER INTERFACES

Thermal management is crucial for the continuing progress in micro/nanoscale electronic, optoelectronic and photonic devices (Yan et al., 2012). The non-uniform heat dissipation common in most of these applications induces local hotspots, which effects the reliability of the device operation and lifetime of the components. Among the heat transfer control techniques, the two-dimensional graphene with superior thermal conductivity has been considered as a promising material to address the heat dissipation issues of the next generation devices (Balandin et al., 2008, Wu et al., 2018) such that graphene-based smart systems with heat transfer control features have attracted considerable attention (Shahil et al., 2012, Yan et al., 2012, Renteria et al., 2014 and Yu et al., 2017, Fu et al., 2020). However, graphene's large interface thermal resistance creates a bottleneck for a possibly required heat transfer route from graphene to ambient fluid or coolant (Chen et al., 2016, Qian et al., 2018, Cao et al., 2018, Ma et al., 2018, Chen et al., 2019).

When two dissimilar materials are in contact with each other, a temperature jump occurs at the interface due to the phonon mismatch known as interfacial thermal resistance (ITR). Especially with increased surface to volume ratio at micro/nano scales, ITR severely interrupts the heat transfer process. Among many ITR studies, modulating the surface wetting has been found as the most effective approach to regulate the ITR (Barisik and Beskok 2012, Pham et al., 2013, Pham et al., 2014, Barisik and Beskok 2014, Vo et al., 2016). In the literature, multiple studies were dedicated to enhancing the interface heat transfer of hydrophobic graphene by increasing the surface wettability using surface functionalization (Cao et al., 2018, Chen et al., 2019) and surface charge patterning (Ma et al., 2018), all which provide a passive control of surface wetting. However, recent technologies require more sophisticated, active control techniques for need-based heat transfer.

As demonstrated in the previous study (Yenigun and Barisik 2019), surface wetting can be manipulated by an applied electric field and the ITR can be controlled actively. However, applying uniform electric field can only apply a torque on the dipolar water molecules to orient them along the applied electric field direction, while the non-uniform electric field can exert an additional force on the dipoles of the molecules, which is also known as liquid dielectrophoresis (LDEP). LDEP is frequently employed as an alternative driving technique for microfluidics to execute various operations with bulk dielectric liquids, including the well-known dielectrowetting (Edwards et al., 2018). While these current studies employ LDEP mostly for liquid actuation, LDEP can also be used for local manipulation of the solid/liquid coupling and resulting ITR. Such an idea will be innovative for heat transfer control at micro/nanoscales to steer heat transfer from a hotspot or toward a heat sink.

In this chapter, a graphene-based smart system for thermal management purposes is studied, where the heat transfer rate can be controlled actively and locally by an applied uniform and non-uniform electric field. Molecular Dynamics (MD) simulations are employed to calculate heat transfer at atomic level while corresponding electric fields will be resolved by solving the Laplace equation numerically to support MD findings. First, a one-dimensional heat conduction through water confined in a graphene channel under a uniform electric field is explored. Later, the spatial effects of non-uniform electric field and resulting two-dimensional heat transfer will be investigated. Electric field induced effects in terms of change in electrohydrodynamics of water and coupling at the water/graphene interface for varying charge of electrodes is characterized.

4.1. Simulation Details

Non-equilibrium molecular dynamics (NEMD) simulations of water confined between multilayer graphene walls as described in Figure 4.1 are performed. First, a uniform electric field was developed in between two parallel multilayer graphene walls by defining the outmost graphene sheet at each side as electrodes and applying equally distributed charge per carbon molecule. Negative and positive charges at equal magnitudes were assigned at these opposing electrodes each side. Applied charges per atoms were varied between 0.018 and 0.12 e per atom, which are in the range presented

in the literature (Kalluri et al., 2011, Qian et al 2019). A computational domain with a cross-sectional area of 3.9×3.9 nm in the surface parallel directions with periodic boundary conditions was found adequate to capture corresponding physics, as the uniform electric field system develops a one-dimensional variation (Figure 1(a)). The thickness of multilayer graphene was optimized to obtain a bulk behavior in solid temperature, which was optimized to be 2 nm at each side. While the height of channel was varied as 2.8, 4, 5.7 and 7 nm, it was kept at 5.7 nm in detailed investigations. The number of water molecules were adjusted to obtain a 1 g/cm^3 of bulk water density. For example, 2690 water molecules were simulated in for 5.7 nm height channel.

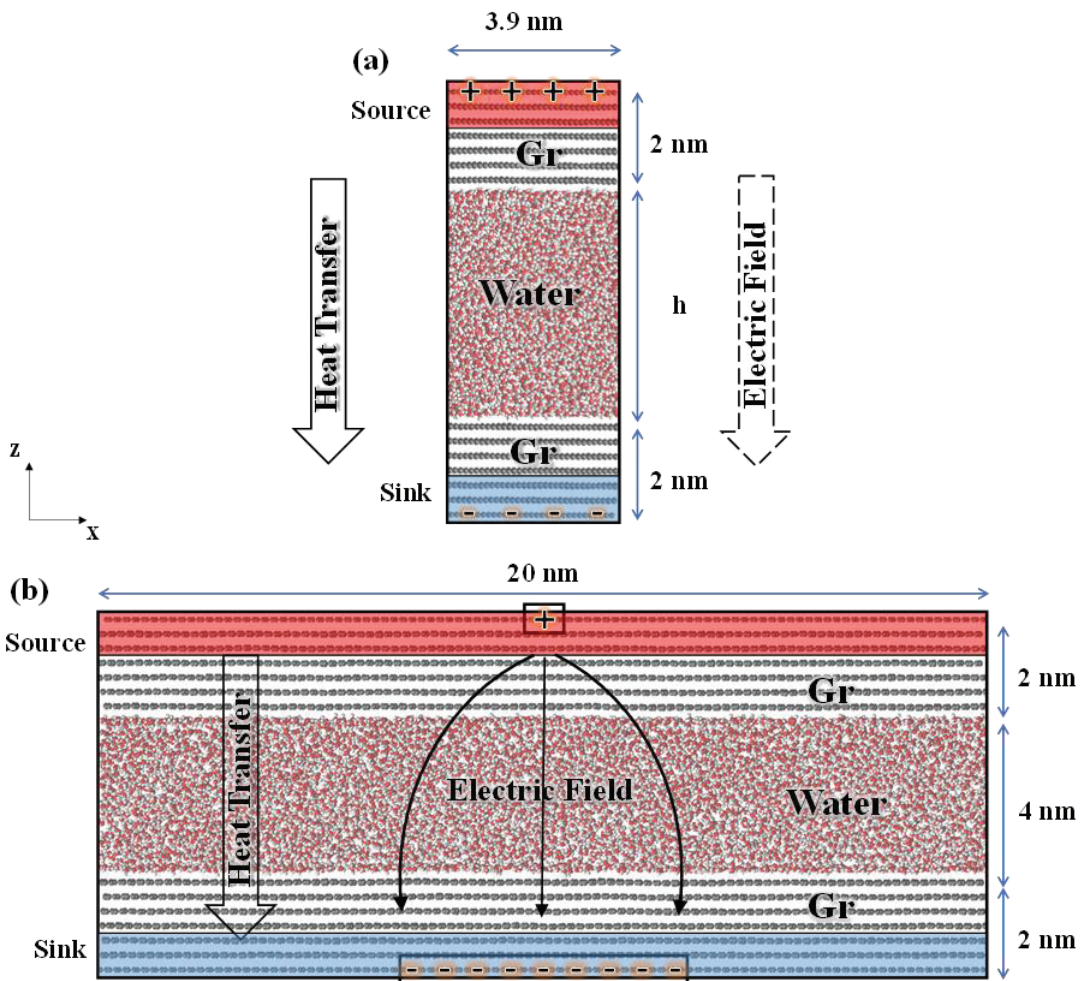


Figure 4.1. Simulation domain of graphene/water system for (a) uniform and (a) non-uniform electric field studies.

Second, a two-dimensional non-uniform electric field was developed between the parallel surfaces by creating a small “pin” electrode and a large “plate” electrode at the outmost graphene sheets on both side (Figure 1(b)). These electrodes were centered in x-direction. For this investigation, we expanded the width of simulation domain as large as

possible allowed by our computational resources. Here, the objective is to develop a large enough non-uniform electric field section to capture two-dimensional variation well, while maintaining regions free from electric field effects at both ends of the simulation domain near to periodicity. Based on many trials, a cross-sectional area of 20×2.5 nm with a channel height of 4 nm were selected while the sizes of electrodes in x-direction were optimized to 0.85 nm and 7.65 nm for pin and plate electrodes, respectively. In addition to computational limitations, these electrode sizes also were optimized to maintain a physically relevant charge density values while creating a non-uniform electric field section adequate to observe and characterize electric field effects properly. The simulation width was almost three times bigger than the size of large plate electrode such that electric field free regions near periodic boundary conditions at both ends were properly formed. Different than uniform case, non-uniform electric field created a body force on the water molecules towards the high electric field intensity regions, which increased the water density as a function of electric field. For such a case, water molecules drawn closer to the near electrode regions resulted in decrease of density in the rest of the system. In order to maintain a bulk density of 1 gr/cm^3 at the electric field free regions, we increased the water molecules iteratively at each case. Table 4.1 lists the number of water molecules simulated at different electrode charges. Charge per atom in pin and plate electrodes were varied in a range similar with the literature (Brukhno et al., 2010, Zhu et al., 2014, Ma et al 2018). Up to 8424 water molecules were modeled. Including the more than 27000 carbon atoms forming the multi-layered graphene walls, simulation domains were formed by 47000 to 52000 number of atoms. Simulations of such magnitude required extensive computational resources and computational times.

Table 4.1. Electric charges assigned on pin and plate electrodes and number of water molecules simulated at each case

Case #	Q_{plate} (e per atom)	Q_{pin} (e per atom)	# of Water Mol.
1	0	0	6678
2	-0.025	0.225	6758
3	-0.05	0.45	6943
4	-0.075	0.675	7401
5	-0.1	0.9	8056
6	-0.12	1.08	8424

SPC/E water model (Berendsen et al., 1987) composed of Lennard-Jones and Coulombic potentials is used with SHAKE algorithm which constrains the bond lengths and angles of this rigid model. In addition, Coulombic potentials are used to model

electrostatic forces. The Adaptive Intermolecular Reactive Empirical Bond Order (AIREBO) (Stuart et al., 2000) potential is used to model the carbon atoms and their interactions. Interactions between water and graphene also calculated by the combined Lennard-Jones and Coulombic potentials. Parameters for the interactions between similar molecules such as O–O and C–C were taken from the corresponding models. However, the parameters determining the interactions of the specific liquid/solid couples are still under investigation in literature. Frequently, interaction parameters for dissimilar molecules are calculated using simple mixing rules as a function of parameters of the pair of identical molecules. However, the interaction parameters between identical molecules are optimized for a bulk material system that parameters calculated based on a mixing rule cannot recover the correct behavior at the given solid/liquid interface. This issue was addressed by Werder et al., through a systematic study (Werder et al., 2003). The graphene/water interaction parameters calibrated by Werder et al., are employed, and later validated by many others (Chen et al., 2016, Cao et al., 2018, Ma et al., 2018) (Table 4.2).

Table 4.2. Molecular interaction parameters used in the current study

Molecule Pair	σ (Å)	ϵ (eV)	q (e)
O-O	3.166	0.006739	-0.8476
H-H	0	0	+0.4238
C-O	3.19	0.0040627	Varies

Atoms in the outmost layer of both sides were fixed to their original locations to maintain a fixed volume system, while the remaining atoms throughout the domain were free to move. To calculate long-range Coulombic interactions of the periodic slab system, the particle-particle particle-mesh (PPPM) solver was used. The applied electrode charges densities were adjusted to obtain equal amount of charge with opposite signs at pin and plate electrodes to obtain a neutral net charge in the system in order to satisfy algorithmic requirements of PPPM solver. Newton’s equations of motion were integrated, by employing the Verlet Algorithm with a time step of 0.001 ps. Simulations were started from the Maxwell-Boltzmann velocity distribution for all molecules at 323K. Initial particle distribution was evolved for 2×10^6 time-steps (2ns) under NVT condition at 323K to reach an isothermal steady state. Afterwards, one dimensional heat transfer between graphene sheets was created using the Nose Hover thermostat applied only to the outmost two graphene sheets of the both few-multilayer graphene walls. Hot and cold reservoirs were thermostated at 363K and 283K to induce heat flux through the

liquid/solid interfaces. The NVE ensemble was applied to the remaining carbon and water molecules. Simulations were performed for an additional 3×10^6 time-steps (3ns) to develop a steady-state heat transfer, after which simulations were performed for 25×10^6 time-steps (25ns) to obtain an adequate time averaging. Considering the large number of atoms simulated, 30ns simulation times required weeks of calculations using average of 350CPUs in high performance computing per case.

For the cases with uniform electric field, one-dimensional variation of temperature was measured by dividing the computational domain into 100 rectangular bins extending through periodic y- and x-direction with a thickness of 0.097 nm in z-direction. Smaller bin thickness of 0.012 nm was also employed to resolve the fine details of the near wall water density distributions with 800 slab bins. On the other hand, simulation domain was resolved in two-dimension for the non-uniform electric field cases. For such a case, the computational domain was divided into rectangular bins extending through periodic y-direction with the size of 0.077 nm in xz- and 0.818 nm in zx-direction to measure temperature. Smaller bins with the size of 0.0077 nm in xz- and 0.818082 nm in zx-direction were used to calculate water density distributions.

For the characterization of MD results, theoretical electric field calculations are also performed. Here, the objective is to describe the variation of electric field for a given MD simulation case, in order to explain and support the observed electrohydrodynamics of water better. Laplace equation (equation 4.1) is solved using finite-element scheme with COMSOL Multiphysics to calculate the spatial non-uniform electric field (equation 4.2) induced in the water domain in Cartesian coordinates as ϕ is the electrical potential and E is the electric field strength.

$$\nabla^2 \phi = 0 \quad (4.1)$$

$$E = -\nabla \phi \quad (4.2)$$

A two-dimensional rectangular domain composed of graphene walls and water was designed at the same size with MD simulations, as shown in Figure 4.2. Pin and plate electrodes were embedded at the outermost regions of solid domains similar to MD system and electrode charges documented in Table 4.1 were studied while the rest of the graphene walls were appointed as zero charge boundary condition. Periodic boundary conditions were applied to the two far outmost boundaries in x-direction. The mesh

independent results were carefully obtained by while using the model parameters of relative permittivity of water as 70.7 similar to value determined for SPC/E water earlier (Reddy and Berkowitz 1989), electrical conductivity of water as 5.5×10^{-6} S/m and density of water as 0.9982 gr/cm³ at the temperature of 293.15 K.

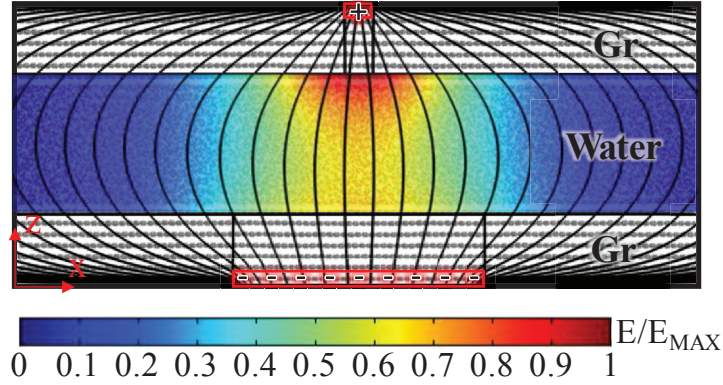


Figure 4.2. Simulation domain of graphene water system under non-uniform electric field for numerical calculation by COMSOL

4.2. Results and Discussion

4.2.1. Uniform Electric Field

A uniform electric field was created through the system shown in Figure 4.1(a) by applying uniform surface electrode charges on opposing electrodes at equal magnitudes but opposite signs. Resulting water density distributions at different electrode charges are given in Figure 4.3. The charge values are varied between 0 to 0.12 e per atom. The well-known density layering with two distinct density peaks extending couple of molecular diameter length from the surfaces develops while density reaches its thermodynamic value of 1 g/cm³ at the center of channel away from surface effects. These density layerings are formed due to the Van der Waals force field of surface and the electric field. With the increase of electrode charge, the near wall density layers are pulled towards the surface. This is the sign of the change in surface energy or surface wetting. By increasing the electrode charge, the number of molecules in near wall regions increases, which enhances the interfacial energy of the initially hydrophobic graphene surface. Furthermore, at electrode charge value of 0.053 e per atom, a solid like density distribution develops observed as density fluctuations through the whole channel as a

result of electro-freezing (Luedtke et al., 2011, Yen et al., 2012). This behavior can be easily seen from the simulation snapshots presented in Figure 4.4(a) to (f). For the electrode charge of 0.053 e and above, a hexagonal structure of (1,0,1) crystallographic ice plane (Yan and Patey 2012) can be observed through x-z plane. The applied electric field changes the hydrogen bond network forcing water to form a crystalline structure by electro-freezing.

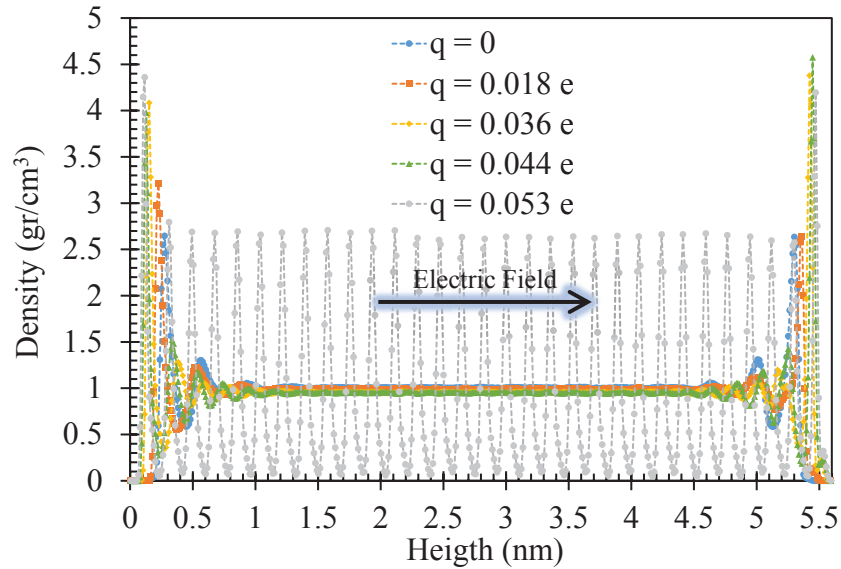


Figure 4.3. Density distributions at electrode charges of 0, 0.018, 0.036, 0.044 and 0.053 e per atom

As explained in previous sections, the main influence of a uniform electric field on a polar dielectric liquid is by affecting their orientations. In order to quantify this, the orientations of the water molecules at varying electrode charges are measured. The probability distributions are calculated by defining an angle (θ) between the dipole moment vector of the water molecule and the surface normal vector as shown in Figure 4.4(g). Simply, the cosine of the angle θ is equal to -1 when the dipole moment vector is facing towards the wall and the cosine of the angle θ is equal to 1 when it is pointing away from the wall. These calculations focused on the first hydration shell within the 0.5 nm distance from the wall, similar to earlier descriptions (Ho et al., 2014, Celebi et al., 2017). Variation of probabilities of cosine of each angle presented in Figure 4.4(g) for different electrode charges. For the zero electric field, the probability of the orientations shows almost a random and symmetrical behavior. On the other hand, when an electric field is applied, the water molecules are forced to align in electric field direction as a function of magnitude of the electric field. Hence, the probability of water molecules facing the surface increases by increasing electrode charge. Specifically, when the electro-freezing

develops at 0.053 e and higher electrode charges, nearly all water dipole moment vectors align with the electric field direction.

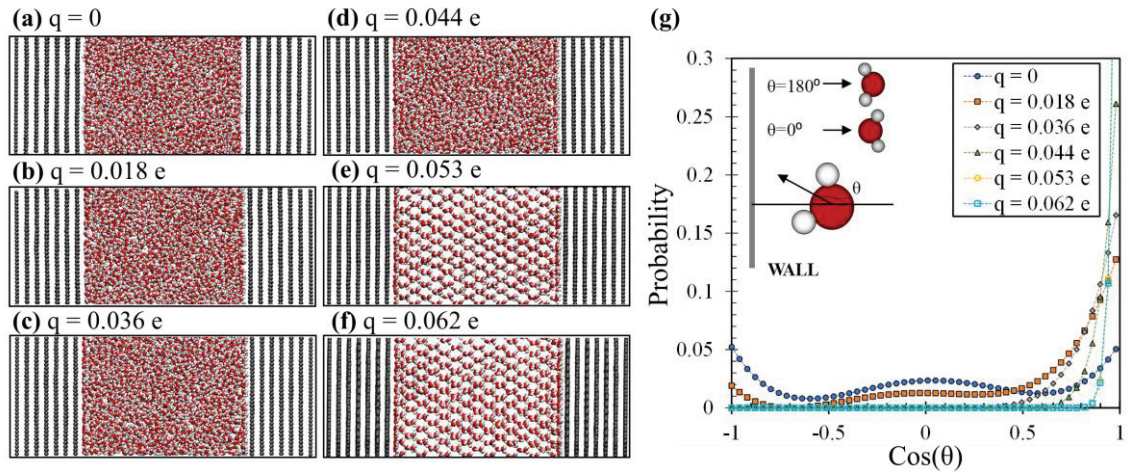


Figure 4.4. The snapshots of the water confined in graphene under uniform electric field with electrode charges of (a) 0, (b) 0.018, (c) 0.036, (d) 0.044, (e) 0.053, (f) 0.062 e per atom and (g) the corresponding probability distributions of water dipoles

Next, one-dimensional heat conduction is created through these systems by assigning 363K and 283K at the opposing hot and cold reservoirs. The resulting temperature distributions are given in Figure 4.5 under varying electrode charges. A linear variation of temperature through the water domain is observed, except the very near wall regions, where the temperature fluctuates due to the density layering. These temperature profiles show variation by the applied electric field. Basically, the slopes of the temperature profiles increase by increasing the electrode charge. Temperature distributions of systems under electro-freezing are given separately in Figure 4.5(b). In these solid like systems, strong temperature fluctuations are measured with small averaging bin size. On the other hand, when a larger averaging applied, linear temperature profiles can be easily observed. It is an important outcome that even in a system with highly ordered water molecules, Fourier's Law of heat conduction is still applicable.

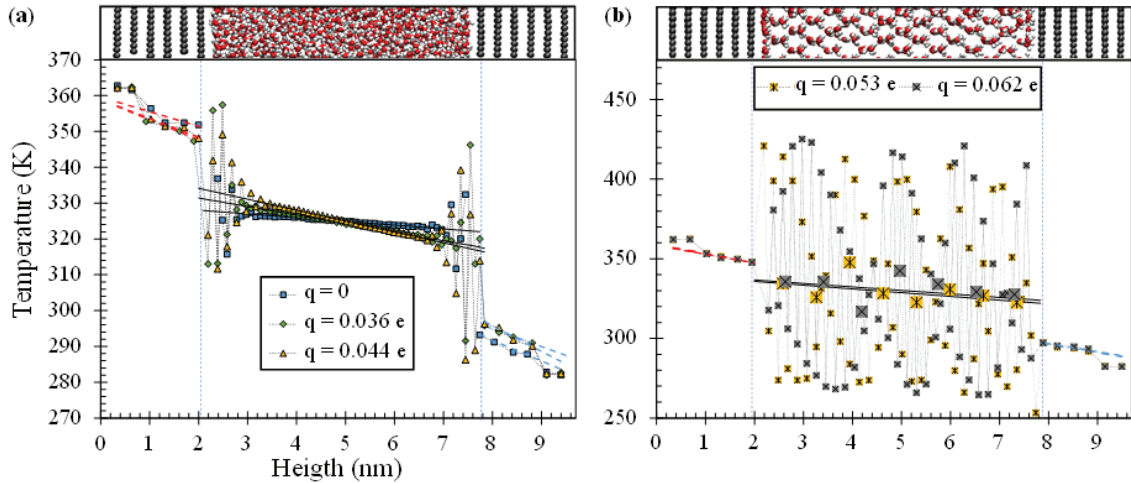


Figure 4.5. Temperature distributions of graphene/water system (a) before electro-freezing and (b) after electro-freezing (larger markers indicate averaged temperature profile)

Through these heat transfer processes; sudden temperature jumps between water and graphene are observed at the interfaces due to the phonon mismatch. This is the well-known interfacial thermal resistance (ITR) which is frequently characterized by the Kapitza Length (L_K) based on temperature jump at the liquid/solid interface and the temperature gradient of the liquid. Linear temperature fits are applied onto temperature distribution of water and graphene in both hot and cold side. Between these linear temperature fits, temperature jumps are measured at both hot and cold interfaces. Variation of ITR in terms of L_K under varying electrode charges are studied and documented in Figure 4.6(a). For no electric field case, a high L_K value of ~ 25 nm is measured on the slightly hydrophobic graphene surface similar to literature (Alexeev et al., 2015). The current interfacial parameters were shown to develop 86° wetting angle (Werder et al., 2003) validating weak thermal coupling. By the application of electric field, L_K shows a drastic decrease until reaching to a constant value through electro-frozen cases. This is a very important outcome; prior to electro-freezing, L_K decreases up to 83% of its no electric field value. This substantial reduction of ITR is due to enhanced solid/liquid coupling at the interface or surface wetting. It was also mentioned in literature that the Coulombic interactions between the charged carbon atoms and water molecules supports heat dissipation (Ma et al., 2018). Temperature dependence of ITR is also observed. The L_K values on the hot surface are lower than the L_K values on the cold surface. This is a similar output with previous chapter. Two different temperature dependent variation in ITR was observed for hydrophobic and hydrophilic surfaces. While L_K increased by increasing temperature on a hydrophilic surface as a result of

lessening density layering on surface by increasing temperature, an opposed behavior was observed for hydrophobic surfaces. Over a hydrophobic surface, the weak density layering develops negligible temperature dependence that L_K decreased by increasing temperature due to dominant enhanced phonon dynamics at higher temperatures. The graphene develops lower L_K values on hot surface; but by the increasing electrode charge, wetting increases that the difference between the L_K values of hot and cold surface lessens. Interestingly, L_K values of hot surface still do not exceed the values on cold surface, since the amount of electric field applied is not enough for to complete the transition of graphene from hydrophobic to hydrophilic (Jiang et al., 2012). When the system reaches to electro-freezing, the liquid domain shrinks at the crystalline form which increases the L_K values. More importantly, the thermal coupling between the solid-like crystalline water and graphene develops stronger dependence onto phonon dynamics, almost similar to the theoretically described solid-solid ITR (Duda et al., 2012). The classical theories of phonon dynamics of solids explain enhanced phonon activities at higher temperatures well. At electro-frozen condition, crystalline water vibrates less increasing the phonon mismatch at cold surface higher than its value at liquid case.

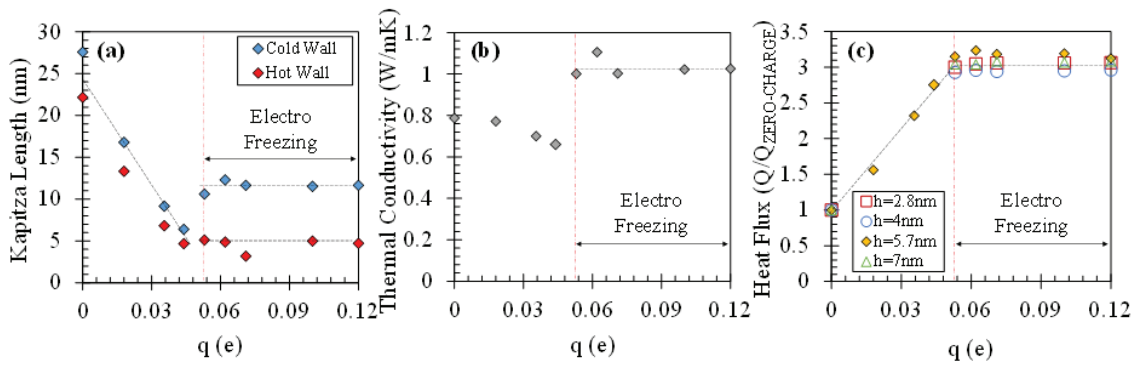


Figure 4.6. (a) Kapitza length and (b) Thermal conductivity of water and (c) non-dimensional heat flux as a function of electrode charge

In addition to ITR, the electric field effects on thermal conduction through the water domain is studied as well. The thermal conductivities of water under different electric fields were calculated from the liquid temperature gradients using Fourier's Law. Figure 4.6(b) presents the thermal conductivity values for different electrode charges. At zero electric field, thermal conductivity is calculated as 0.8 W/mK at the average temperature of 325 K, which agrees with the literature (Mao et al., 2012). Conductivity slightly decreases prior to electro-freezing due to the restricted molecular diffusion and hydrogen bonding activities of water molecules under electric field. After reaching the

crystalline structure, conductivity shows a sudden jump and then remains constant with the increased electric field. Change in water thermal conductivity is not as dominant as the change in ITR under increasing electric field.

As a result, the total heat transfer through water/graphene system varies by electric field; the heat flux substantially increases up to 3 times by an applied electric field as shown in Figure 4.6(c). This major enhancement is basically due to large decrease in ITR under electric field. Heat flux reaches this value right at electro-freezing after which it remains constant. This behavior is further explored at different height confinements, where channel heights of 2.8, 4 and 7 nm are modeled. For these cases, only focus was given to no electric charge case and each electrode charge value correspond to electro-freezing conditions. Different height systems develop different heat flux values for the same temperature difference applied between the hot and cold reservoirs. For comparison, each case is normalized by its value at no-charge. A universal behavior is observed in normalized heat flux behavior presenting negligible confinement height dependence at these scales.

4.2.2. Non-uniform Electric Field

Up to this point, uniform manipulation and control of the of ITR and resulting heat transfer between graphene and water are described. From here, the local control of heat transfer by a non-uniform electric field is practiced. For this purpose, a smaller pin electrode and a larger plate electrode centered at the width of graphene/water system is defined as shown in Figure 4.1(b). The simulated domain is extended to obtain regions with negligible electric field near periodic boundaries at both ends. By this way, a proper periodic effect is attained on heat transfer physics to measure only influence of the given non-uniform electric field. The simulation and electrode sizes were optimized to cover an adequate resolution of non-uniformity in two-dimension allowed by the computational capabilities. Different than the uniform case, a net electrostatic force develops on water molecules under non-uniform electric field. We should note here that similar electrostatic forces develop in the earlier uniform electric field cases as well, but forces on negative and positive poles of water molecules are equal to each other yielding zero net force; they only create a torque which eventually is the reason for the alignment of dipoles in electric

field direction. For non-uniform electric field, forces developing on opposite sides of a water molecule become different as the electric field is non-homogeneous. Such a net electric field force on a dipole can be approximated as $\vec{F} = \vec{p} \cdot \vec{\nabla} \vec{E}$ as a function of the water dipole moment vector (\vec{p}) and the gradient of electric field in tensor form ($\vec{\nabla} \vec{E}$). While the water dipoles tend to get in line with electric field direction, a net body force is expected to develop on a water molecule in electric field gradient direction towards the higher electric intensity regions.

First, the theoretical electric field distributions in the system at the studied electrode charges are characterized. To specify a simulation case, charge value of its plate electrode is set while the charge on corresponding pin electrode was assigned inversely proportional to electrode size at opposite sign. By this way, the total charge on the plate and pin electrodes were equal to each other to maintain a zero-net charge in the system required by LAMMPS calculations. Figure 4.7(a)-(f) presents the electric field contours and lines as the solution of the Laplace equation using the finite element solver COMSOL. Electric field results at different electrode charges were normalized with the maximum electric field strength measured through all these cases, which is at 0.12 e plate electrode charge. At each case, highest electric field strength develops near to pin electrodes. Electric field decreases away from both electrodes towards periodic boundaries. Results present the non-uniform electric field and the resulting two-dimensional variation of electric field intensity through simulation domain. The electric field lines describe the direction of the electric field vectors in each system. The molecular snapshots of the MD simulations under the corresponding non-uniform electric fields are presented in Figure 4.7(g)-(l) at different electrode charges. First, it can be easily observed that an LDEP force develops near electrode regions and increasing the water population. By the increasing electric field, the bending of graphene layers at both pin and plate electrode sides is observed. This behavior becomes evident starting with the electrode charge of $q_{\text{plate}}=0.05$ e. Next, water dipole vectors are calculated in two-dimensional space. Figure 4.7(m)-(r) presents directions of water dipole vectors as blue arrows on the top of corresponding simulation snapshots. The influence of electric field can be observed easily as the random distribution of dipole vectors at no electric charge changes quickly by application of electrode charges. At $q_{\text{plate}}=0.05$ e, line-up of dipole vectors in electric field directions between the electrodes becomes obvious. This shows that the system is undergoing an electro-freezing like ordering, even the molecular picture of the system does not show a

crystal structures due to the non-uniform electric field. These results are also consistent with the uniform electric field conditions as the electro-freezing started at a similar $q=0.053$ e. By the increase of electrode charges, more dipole moment vectors align with the electric field lines given through Figure 4.7(a)-(f). The solid-like ordering of water is clearer for these cases in simulation snapshots. These are not like perfect crystal structures formed under uniform electric field, but they are mostly appeared as multi grain structures compressed towards the regions with high electric field intensities. Away from electrodes, mostly random dipole distributions are observed near the periodic boundaries, except the highest electrode charge of $q_{\text{plate}}=0.12$ e. The effect of LDEP forces can also be seen clearly from the density contours in two-dimension given in Figure 4.7(s)-(x). Water density of 1 gr/cm^3 is measured in the bulk of the channel except the near interface regions developing well-known density layering. By the increase of electrode charges, this solid-like water layering increases and grows towards channels bulk. Local water densities higher than 2.8 gr/cm^3 are observed near interface similar to density layering observed over highly hydrophilic surfaces by earlier studies (Huxtable et al., 2003, Janeček and Netz 2007, Pham et al., 2016). As the non-uniform electric field forces water molecules to move towards the high electric field intensity region, ice-like average density values are observed similar to literature reporting density values as high as 2.51 g/cm^3 bulk density (Hemley et al., 1987, Huang et al., 2016). The electro-freezing formation starting from near electrode regions towards the bulk liquid can be easily observed by solid like water density variation. This local density structuring is very similar with the local variation of the non-uniform electric field shown in Figure 7(a)-(f). As explained earlier, LDEP forces pull water molecules towards the near electrode regions which yields increase of density as a function of electric field, and depletion in the rest of the simulation domain. This phenomenon is compensated by adding further water molecules in simulation domain until the regions near periodicity reaches to bulk value of 1g/cm^3 . It should also be noted that the water density increases near both pin and plate electrodes, but pin electrode region develops a higher density increment. While water molecules away from electrodes were unaffected, the local water density and resulting pressure were varied in two dimensions as a function of the non-uniform electric field.

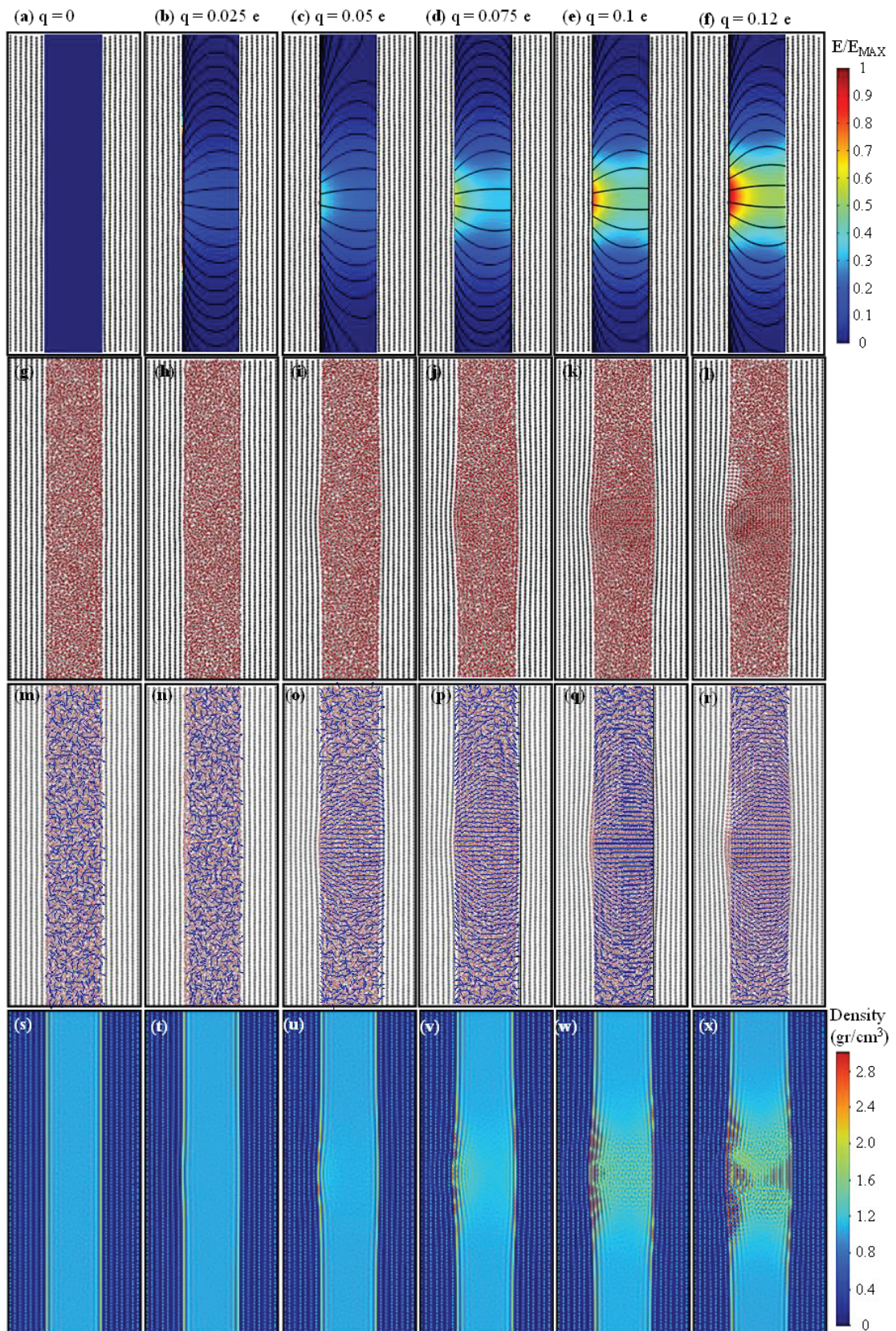


Figure 4.7. (a-h) Electric field contours, (g-l) molecular orientations, (m-r) dipole moment vectors of water molecules and (s-x) density contours at different electrode charges

Next, heat transfer is developed between the thermostat regions employed at the two outmost layer of graphene walls with the temperatures of 363K and 283K. Temperature contours of the water domain for different electrode charge values are documented in Figure 4.8, while the heat transfer and the electric field is in the same direction. Temperature of the graphene layers in x-direction remain constant due to the extremely high thermal conductivity of graphene. Temperature gradient only exist in cross-plane graphene (i.e., interface normal direction). To illustrate the graphene temperature levels, temperature of each graphene layer is written in the corresponding line in Figure 4.8. In Figure 4.8(a), 1D distribution in water domain between the thermostated graphene walls under zero-electric field is documented. As electric field intensity increasing in the water domain, 2D variations are observed in temperature distributions, especially near electrode regions; where temperature increases near hot reservoir side with pin electrode and decreases with cold reservoir side with plate electrode. Consequently, high amount of reduction in temperature jumps at the graphene/water interfaces are observed as a function of electric field. Due to the higher LDEP forces, higher thermal coupling at graphene/water interface is created, locally. As a result, temperature discontinuity near pin electrode region diminishes. In the case of hot-spot cooling or heat flow guiding application, such local thermal coupling control would be desirable.

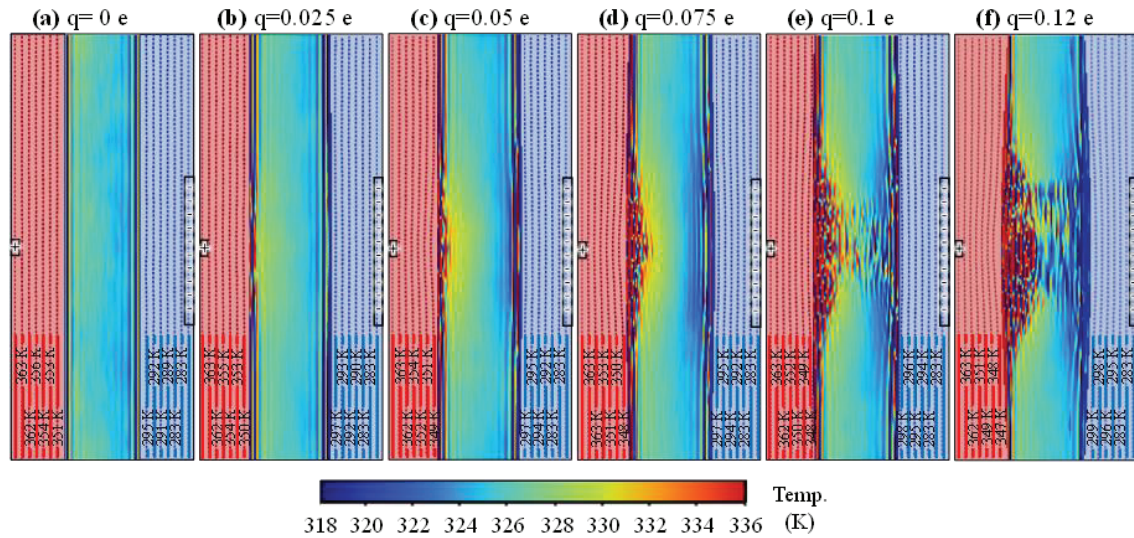


Figure 4.8. Temperature contours at different electrode charges of (a) $q_{\text{plate}}=0$, (b) 0.025 e, (c) 0.05 e, (d) 0.075 e, (e) 0.1 e and (f) 0.125 e

Local Kapitza length values are calculated in order to characterize the non-uniform heat transfer induced by non-uniform electric field. Bins with the size of the pin

electrode throughout the channel in x-direction are defined as shown in Figure 4.9(a). Average temperature gradients in z-direction are obtained for each bin in x-direction. The obtained one-dimensional temperature profiles are very close to linear behavior, even though the current system has two-dimensional temperature distribution. After this point, Kapitza length values are calculated with the same methodology as before, for each bin in x-direction and each wall. The resulting L_K values are documented in Figure 4.9(b) and Figure 4.9(c) for hot and cold wall, respectively. Weak thermal couplings of 22.5nm and 27.5nm are documented for zero-electric field and the results are in agreement with the uniform electric field case. L_K values are reduced significantly at regions close to pin and plate electrodes with the application of electric field. While getting away from the electrode regions, reduction in L_K lessens due to the decreased electric field levels and LDEP forces. No change in L_K is observed at $q_{\text{plate}}=0.025 e$ case, while getting away from the electrodes, but with increased electrode charge, L_K near periodic regions are slightly decreases. However, this change in L_K is not as dominant as in electrode regions. Therefore, the effect of non-uniform electric field is captured without disturbing the periodic conditions in axial direction. There are three main factors that contribute to the heat transfer while applying non-uniform electric field; first, through improved coulombic interaction between charged carbon atoms and water molecules; second, electro-stretching caused by the alignment of the dipoles of water molecules; and third, by exerting a bulk force on the dipoles of water molecules toward higher electric field regions (i.e., LDEP forces). Due to these three mechanisms L_K values show strong variation as a function of non-uniform electric field. In addition, average water density values in each bin are calculated in order to characterize the LDEP forces increasing the pressure at near electrode regions, which are documented in Figure 4.9(d). Even though the density change is negligible in low electrode charge range, L_K reduction still exist due to enhanced coulombic interactions. However, as electrode charge increases to 0.075e, density increases 20% and L_K reduces 90% in pin electrode region. By further increase in electrode charge increases the density even more and L_K reaches almost 0nm ~ultra-low L_K at pin electrode region. These results are also in agreement with pressure and density dependence of the interfacial thermal resistance studies in the literature (Pham et al., 2013, Han et al., 2017).

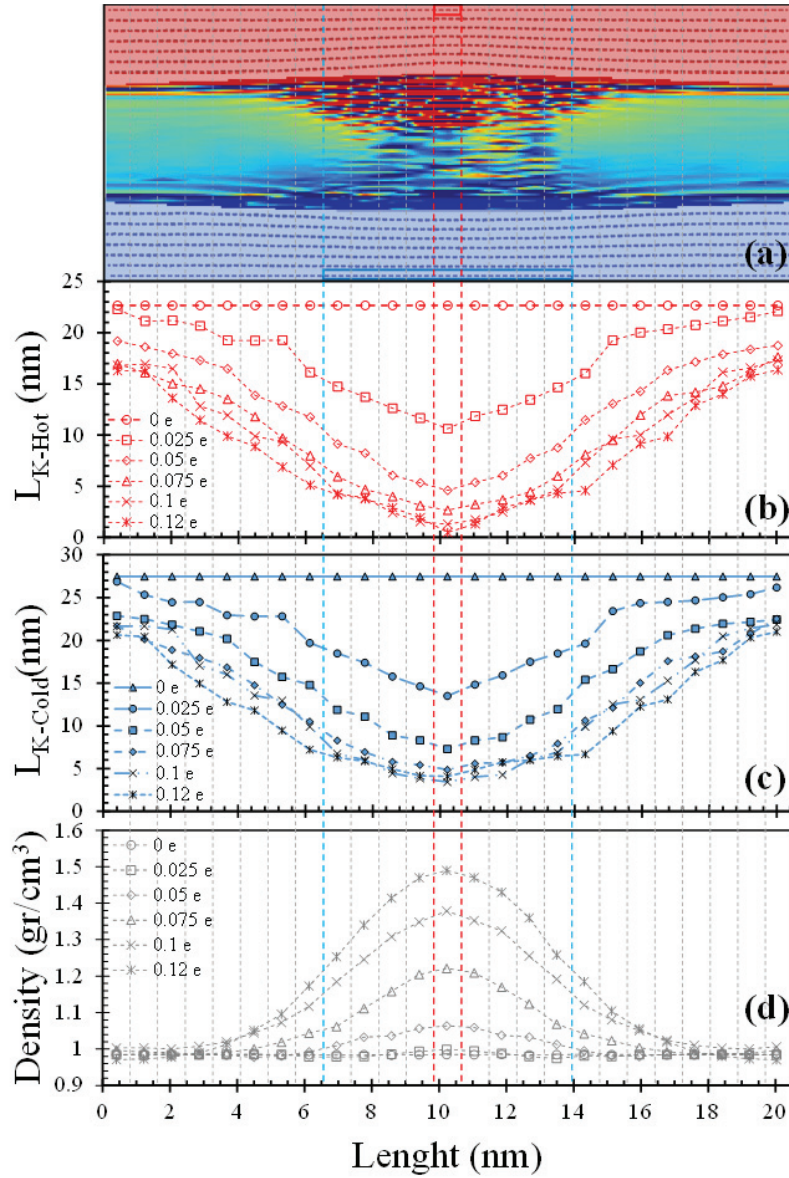


Figure 4.9. (a) Representation of the regions for local measurements. Temperature counter of $q_{plate}=0.12e$ case was used in figure. Local variation of (b) L_{K-Hot} , (c) L_{K-Cold} , and (d) water density measured at each local region for different electrode charges

Next, L_K values as a function of applied charge at pin and plate regions are characterized. Local L_K values correspond to pin and plate regions in hot and cold wall are averaged and from now on will be referred to as L_{K-Pin} and $L_{K-Plate}$, respectively. Variation of L_{K-Pin} and $L_{K-Plate}$ as a function of electrode charge is compared with L_K results of uniform electric field study ($L_{K-Uniform}$) from the previous section and documented in Figure 4.10(a). Until electro-freezing develops at $q_{plate}=0.05e$, $L_{K-Uniform}$, L_{K-Pin} and $L_{K-Plate}$ present a very similar trend and decreases approximately 83%. This similar trend is due to lower LDEP forces creating lower pressure on the interfaces. At

low electrode charge regions, uniform electric field between the finite and equal sized electrodes can also be employed for local heat transfer control applications. However, non-uniform electric field has an advantage on controlling local heat transfer between unequal sized regions, which allows the collection and distribution of heat to/from a smaller region from/to a larger region. Furthermore, increasing electrode charge from $q_{\text{Plate}}=0.05e$, $L_{K\text{-Uniform, Hot}}$ remains approximately around 5nm, while non-uniform electric field reduces ITR even more. $L_{K\text{-Pin}}$ undergoes a 99% decrease at $q_{\text{Plate}}=0.1e$ and becomes almost zero at $q_{\text{Plate}}=0.12e$, which shows the real advantage that LDEP develops at these electrode charge ranges. Non-uniform electric field application shows another advantage that on the contrary to uniform electric field, L_K values at cold surface continues to decrease even after electro-freezing starts. Under uniform electric field, interface thermal resistance undergoes a strong temperature dependence at cold wall while electro-freezing took place and result in a L_K increase from 6nm to 12nm. On the contrary, non-uniform electric field develops very low L_K values at cold wall due to the body forces created by LDEP. Specifically, the lower phonon activities at cold surface are offset by the LDEP forces so that L_K values at cold wall becomes slightly higher than the hot wall. Finally, to characterize the variation of $L_{K\text{-Pin}}$ and $L_{K\text{-Plate}}$ as a function of applied charge, an exponential fit is applied in each of them.

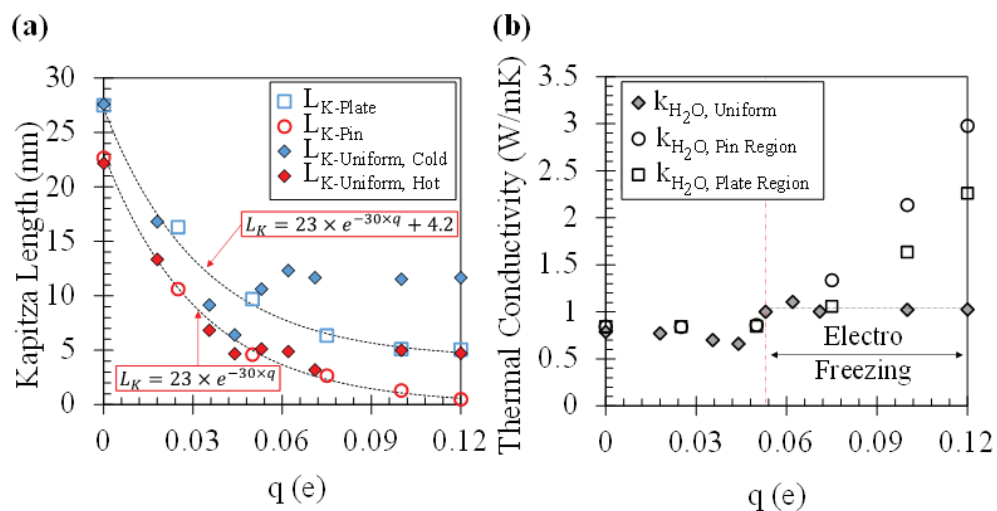


Figure 4.10. (a) Kapitza Length values at hot and cold interfaces under varying uniform and non-uniform electric fields. (b) Local water thermal conductivities in line with pin and plate electrodes compare to water thermal conductivity under uniform electric field

Next, thermal conductivity of water is characterized under non-uniform electric field. Thermal conductivity on each bin is calculated based on literature (Caretto et al.,

2005, Chen et al., 2011, Iriarte-Carretero et al., 2018) and density measurements documented in Figure 4.9(d). Basically, local thermal conductivity of water is calculated for each region from thermodynamic tables (Caretto et al., 2005), for low electrode charge region. For high densities ($\rho_{\text{Water}} > 1.2 \text{ kg/m}^3$) developed near electrode regions at high electrode charges ($q_{\text{Plate}} \geq 0.075 \text{ e}$), data provided for solid-like compressed water is used to calculate thermal conductivity (Chen et al., 2011, Iriarte-Carretero et al., 2018). Local water thermal conductivity for pin and plate regions are documented in Figure 4.10(b) along with thermal conductivity of water under uniform electric field. Slight decrease in thermal conductivity is observed prior to electro-freezing. However, the decrease is smaller than uniform electric field study, since molecular diffusion of water is less than the uniform electric field case. After increasing the electrode charge even further, density increases due to the pressure created by LDEP forces, so the thermal conductivity increases. Thermal conductivity of water under uniform electric field increases substantially, due to single crystalline structure formation. However, non-uniform electric field creates multiple grain boundaries so around $q_{\text{Plate}} = 0.05 \text{ e}$ thermal conductivity does not show any significant increase. Moreover, under non-uniform electric field, thermal conductivity increases gradually due to increased density and higher molecular ordering. Eventually, water thermal conductivity becomes higher than uniform electric field case for $q_{\text{Plate}} \geq 0.075 \text{ e}$. In addition, due to the increased LDEP forces thermal conductivity is higher at pin electric electrode region.

At this point, it is considered that there is possibly an influence on the direction of heat transfer comparing to the direction of electric field and the pin electrode's location. Up to here, the studied cases were showing that both heat transfer and electric field were in the same direction as well as pin electrode was on hot reservoir side. Nevertheless, it is known that different configurations are possible. The description in literature for directional dependence of the heat transfer through a non-homogeneous domain is "thermal rectification", which has been studied for numerous systems that also includes graphene. As an example of strong directional dependence, it was shown that in-plane heat transfer of graphene layer consisting non-uniform/asymmetric structural defects (Nobakht et al., 2018) or solid stiffness (Wei et al., 2019). Basically, the asymmetry of a system allows easier heat transfer in one direction compared to heat transfer in the same axis but in the opposite way. In this case, the non-uniform electric field creates non-homogenous interface coupling and water structuring that wanted to be tested for possible heat transfer rectification. First of all, it is observed that there is no effect on direction on

heat transfer related with direction of the electric field. The water dipole orientation changes according to electric field direction, however very likely structuring of water and ITR develop through the system, that is independent from the direction of the electric field. In plain manner, regardless of field direction, under non-uniform electric field, bipolar water molecules perceive forces towards the higher electric field region. Considering this situation, the system is tested by changing the heat transfer direction when the pin electrode located on cold reservoir side. The $q_{\text{plate}}=0.1$ e applied since it yields a distinct non-uniformity as the electric field dominated region in between the pin and plate electrodes develops an almost “triangular shape” non-uniform electric field while the periodic regions evidently free from electric field effects. In addition, it is fair to state there is a distinct inhomogeneity exists in the system. For lower electrode charges the non-uniformity is not strong while the electric field dominated region and resulting solid-like ordering grows in the channel into a “trapezoidal shape” decreasing the non-uniformity at higher electrode charges. Temperature counters of two alignment presented in Figure 4.11: the pin electrode is on hot side (Figure 4.11(a)) and pin electrode is on cold side (Figure 4.11(b)). Between these two cases two-dimensional variation of water temperature differs. In case the pin electrode was on hot reservoir side, water temperature near the pin electrode remained higher than the rest of the system due to substantially decreased temperature jump (or increased thermal coupling) between the hot reservoir graphene and water (Figure 4.11(a)); on the other side of this system, plate electrode creates comparably lower decrease of temperature jump on cold surface, but water near cold plate electrode remained in a lower temperature than the rest. An opposite but very similar behavior developed when the heat transfer direction is changed (Figure 4.11(b)). Near the pin electrode, which is on cold reservoir side, substantially lower water temperature values occurred due to the reduced temperature jump between the cold reservoir graphene and water, and slightly higher temperatures near plate electrode at hot reservoir side due to exact same reasons. While the behavior observed is similar, the quantitative characterization of heat transfer is the main focus in these two cases. Firstly, the $L_{K-\text{Pin}}$ and $L_{K-\text{Plate}}$ values are compared: $L_{K-\text{Pin-Hot}}=2.66$ nm and $L_{K-\text{Plate-Cold}}=6.34$ nm were measured when the pin is on hot side, and $L_{K-\text{Pin-Cold}}=3.72$ nm and $L_{K-\text{Plate-Hot}}=4.59$ nm were developed if the pin is on cold side. Considering these outcomes, temperature dependent ITR shows itself. Basically, $L_{K-\text{Pin}}$ increases when it is on the cold side due to temperature dependence of phonon dynamics, and similarly, $L_{K-\text{Plate}}$ decreases when it is on the hot side with enhanced phonon activities. The first effect of changing the heat

transfer direction is decreasing the difference between L_{K-Pin} and $L_{K-Plate}$. However, increase of L_{K-Pin} and decrease of $L_{K-Plate}$ are almost in the same order that the total ITR in the system remains same. Hence, ITR mechanisms of the current system under a non-uniform electric field does not create any rectification. Second, thermal conductivity of the water is focused on these two cases. Even though there is a difference between LDEP forces and resulting water densities and thermal conductivities of opposing pin and plate electrode regions, it is observed that this difference is not strong enough to create any rectification. Ultimately, the heat flux is measured in both configuration using Equations (1.8)-(1.10) and calculated very similar heat transfer rates on the order of 2 GW/m^2 . As a result, current heat transfer under non-uniform electric field does not show dependence on the direction of heat transfer.

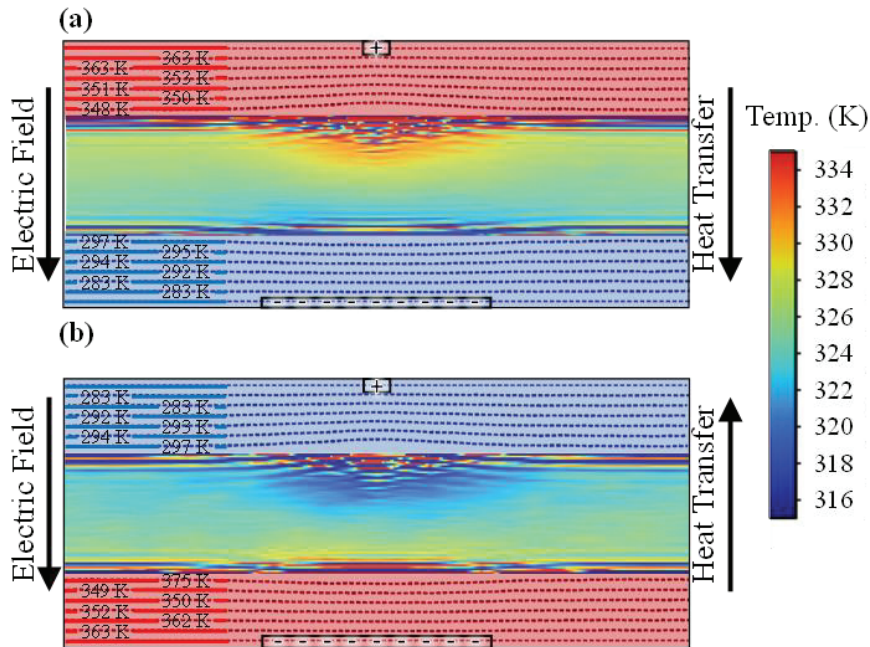


Figure 4.11. Temperature contours of $q_{Plate}=0.075 \text{ e}$ case with different heat transfer directions as the pin electrode on (a) hot and (b) cold reservoir side

As a final step, the local variation of heat transfer rates through the system under varying non-uniform electric field is characterized. An average heat transfer rate of the whole system is calculated based on Equation (1.8)-(1.10) at different electrode charges. Then, the local heat flux values are calculated through each region (described in Figure 4.9) based on their total thermal resistance as $Q_{Local} = (T_{Hot} - T_{Cold}) / R_{Local-Total}$. Basically, the total thermal resistance of each local region can be written as $R_{Local-Total} = R_{Gr-H} + R_{K-H} + R_{H_2O} + R_{K-C} + R_{Gr-C}$ where R_{Gr-H} and R_{Gr-C} are the thermal

resistances of graphene walls at hot and cold reservoir sides, R_{K-H} and R_{K-C} are the interfacial thermal resistances of the graphene/water interfaces at hot and cold reservoir sides, and R_{H_2O} is the thermal resistance of water in the middle of the two graphene slabs. The local thermal resistance of water ($R_{H_2O} = L_{H_2O} / k_{H_2O}$) is calculated from the thickness of water slab (L_{H_2O}) and its local thermal conductivities (k_{H_2O}). Similarly, graphene thermal resistance ($R_{Gr} = L_{Gr-\parallel} / k_{Gr-\parallel}$) is determined using the local cross-plane thickness ($L_{Gr-\parallel}$) and thermal conductivities of graphene walls in surface normal direction ($k_{Gr-\parallel}$). Moreover, the high electrode charges ($q_{Plate} \geq 0.75 e$) creating bending of graphene at high electric intensity regions due to LDEP forces result in local increase of cross-plane thermal conductivity of graphene. The thermal resistance of interface is the function of local temperature jump and heat transfer rate as $R_K = \Delta T_{Interface} / q_{Local}$. It should be underlined that it is important to calculate the interface temperature jump from the temperature fits describing the bulk behavior of both solid and liquid sides. Especially, if any electric charge is applied on just the graphene layer facing the liquid, behavior and the resulting temperature of this graphene layer differentiate from the bulk behavior of few-layer graphene. Calculating a temperature jump between this nearest graphene layer and liquid yields a very erroneous ITR and/or L_K and a misleading characterization of heat transport as done by Ma et al., 2018. Instead, local temperature jumps are calculated from bulk profiles of solid and liquid sides. As the temperature jumps are known, the local thermal resistance of interface and the heat transfer rate at the corresponding region by a coupled iterative solution are calculated. Finally, local heat transfer rates in each region along the x-direction for every different electrode charge are obtained. These local heat flux values are validated by comparing their average with the total heat flux calculation of Equation (1.8)-(1.10) and obtained an exact match.

Next, average heat flux values at pin and plate regions are determined based on the previous findings. In Figure 4.12, local heat transfer rates at pin (Q_{Pin}) and plate (Q_{Plate}) regions are documented along with heat flux of uniform electric field cases ($Q_{Uniform}$). Q_{Pin} , Q_{Plate} and $Q_{Uniform}$ increases with similar trend until electro-freezing develops inside the water domain. In this electrode charge range, heat transfer rate increases three times when compared to zero-electric field case. These results are in agreement with the variation in L_K and thermal conductivity measurements. As mentioned before, advantage of using

non-uniform electric field at low electrode charge range is its ability to focus or distribute heat flow, locally. After electro-freezing develops ($q_{\text{plate}} \geq 0.05 \text{ e}$), heat flux remains constant for uniform electric field case, while the local heat fluxes at pin and plate regions of non-uniform electric field cases continue to increase significantly due to the further thermal coupling improvement and water thermal conductivity enhancement with the help of LDEP. Consequently, up to nine times increase is observed at Q_{Pin} , while Q_{Plate} remains lower than Q_{Pin} due to comparably lower LDEP forces acting on the plate electrode region.

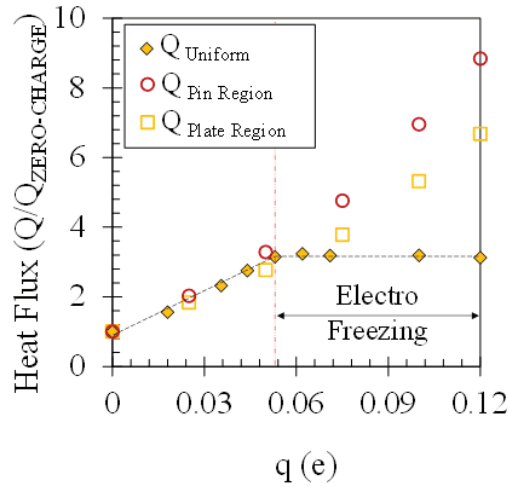


Figure 4.12. Variation of local heat rates at pin and plate electrode regions under non-uniform electric field as a function of electrode charge. Results of uniform electric field case are given for comparison

4.3. Conclusion

In summary, the effect of uniform and non-uniform electric field on the heat transport of graphene/water interface through NEMD simulations is investigated. Both uniform and non-uniform electric fields modified the graphene/water interface energy through the electrostatic interactions and created orientation polarization of water by aligning dipoles to the direction of the electric field. In addition to these effects, a non-uniform electric field also created a net force on water molecules towards higher electric field gradient region due to liquid dielectrophoresis (LDEP). It is found that, interfacial thermal resistance, thermal conductivity, and the resulting heat transfer can be altered by these mechanisms. By increasing the electric field intensity, Kapitza length near electrodes under both uniform and non-uniform electric fields prior to electro-freezing

were decreased 86%; in this electrode charge range, heat transfer increases up to 3.2 times through electrode regions. By employing non-uniform electric field, further reduction in interface resistance can be achieved with the help of LDEP, and ultra-low Kapitza resistance values with up to 99% reduction near pin electrode interface can be obtained. In addition, thermal conductivity of water increases gradually as well, with the non-uniform electric field compressing the water so that heat transfer increases up to 9 times at pin electrode region. As a result, active and local the heat transfer control between water and graphene is demonstrated in two-dimensional space by an applied non-uniform electric field.

CHAPTER 5

HEAT TRANSFER CONTROL BY INTERFACE- LOCALIZED LIQUID DIELECTROPHORESIS USING INTERDIGITATED ELECTRODES

Interdigitated electrodes (IDEs) are used in various technological application such as optical and electrochemical studies to measure the impedance, capacitance and conductivity of a droplet or a gas (Vakilian and Majlis 2014). Essentially, IDEs are consisting of opposingly charged microelectrode arrays embedded together, which can create non-uniform electric field. Besides measurement purposes, IDEs are widely used in microfluidics application such as fluid actuation, particle trapping and surface wetting control (Edwards et al., 2018). Surface wetting control of a dielectric liquid via IDEs are known as dielectrowetting applications (McHale et al., 2011). Different than electro-wetting on dielectrics (EWOD), dielectrowetting has the capability of resolving contact-angle saturation problems occurred in EWOD applications and spreading dielectric droplets into thin films, achieving perfect wetting (Barman et al., 2019). In previous chapters it is shown that the solid/liquid interface coupling can be actively controlled by using an electric field. Therefore, the concept is implemented for manipulation of the ITR at graphene/water interface by an applied uniform and non-uniform electric field and achieved control of the heat transfer rate. Findings of previous studies (Yenigun and Barisik 2019, Yenigun and Barisik 2021) show that use of non-uniform electric field can increase the heat transfer even more, due to the dielectrophoretic forces applied on the water dipoles increasing the pressure at the heat transfer surface. However, non-uniform electric field is only localized where a pin type electrode is inserted. Instead, by using nano-interdigitated electrodes non-uniform electric field can be created everywhere at the surface, so heat transfer enhancement at surface will be localized throughout the interface of solid/liquid. To the best of our knowledge, interface localized heat transfer control via nano-interdigitated electrodes has never been investigated in literature.

In this chapter, graphene-based smart material for thermal management purposes will be investigated, where the heat transfer rate can be controlled actively by applied non-uniform electric field onto the micro/nano-fluidic system through employing interdigitated electrodes. In the following sections, the effect of non-uniform electric field

created by IDEs on the interfacial heat transfer will be investigated by means of water density layering, water dipole moment vectors, and interface thermal resistance as a function of electric field strength. In addition, effect of surface charge density and electrode length on the ITR will be characterized.

5.1. Simulation Details

Water confined between few-layer graphene walls with embedded interdigitated electrodes was simulated as illustrated in Figure 5.1. Cross sectional area of the computational domain was varied between 3.9×3.9 nm to 3.9×20.4 nm in the surface parallel directions where periodic boundary conditions were applied. The channel height (h) between 2 nm thick few-layer graphene walls was varied between 5.7 nm and 9 nm. Width of the electrodes that generate non-uniform electric field in the surface normal direction were selected as 0.5, 1, 1.5, 3 and 5 nm. The heights of the channels were specifically chosen for two different reasons. Firstly, to be able to monitor both the graphene-water interface phenomenon and continuity behavior at the bulk of the channel. Therefore, the simulation area is large enough to observe bulk thermodynamic properties at the center of the channel and the density layers are occurred due to the wall force-field effects and non-uniform electric field effects. Consequently, water density is kept at 1 g/cm^3 at the bulk of the channel while the number of water molecules is varied between 2690 and 15211. Secondly, to accommodate the non-uniform electric field created by the interdigitated electrodes with different widths within the water domain, according to Van Gerwen et al., 99% of the electric field is generated in the surface normal with the distance of 1.5 times the electrode width (Van Gerwen et al., 1997). Thus, keeping the height of the channel above multiple of the electrode width with 1.5 creates an interface localized electric field region. Non-equilibrium molecular dynamics (NEMD) simulations were performed with LAMMPS (Large-scale Atomic/Molecular Massively Parallel Simulator) algorithm.

SPC/E water model (Berendsen et al., 1987) composed of Lennard-Jones and Coulombic potentials is used with SHAKE algorithm which constrains the bond lengths and angles of this rigid model. The Adaptive Intermolecular Reactive Empirical Bond Order (AIREBO) (Stuart et al., 2000) potential is used to model the covalent bonds

between carbon atoms. The molecular interaction parameters between C-C pair were taken from the corresponding model. Interactions between water and carbon molecules also calculated by the combined Lennard-Jones and Coulombic potentials. The molecular interaction parameters for each molecule pair used in the simulations were given in Table 5.1.

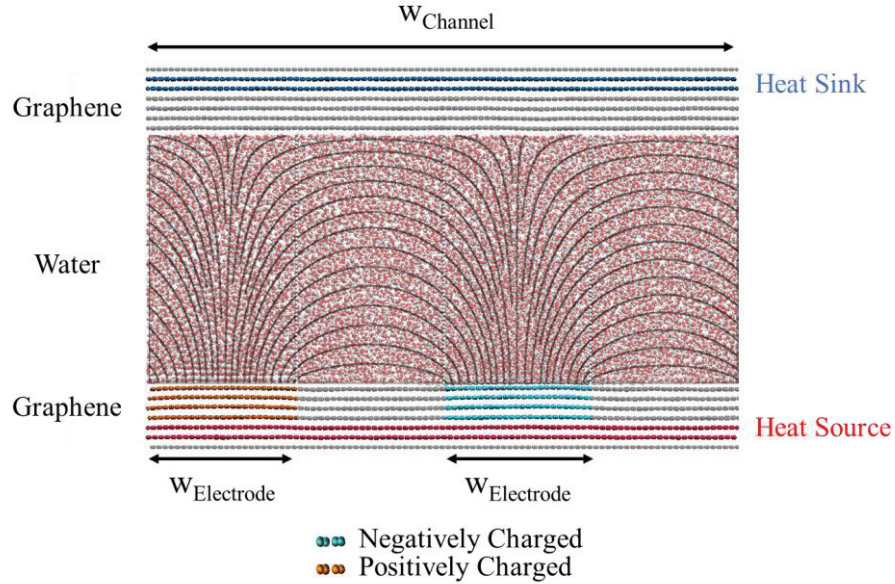


Figure 5.1. Molecular dynamics simulation domain for nano-interdigitated electrodes

Table 5.1. Molecular interaction parameters used in the current study

Molecule Pair	σ (Å)	ϵ (eV)	q (e)
O-O	3.166	0.006739	-0.8476
H-H	0	0	+0.4238
C-O	3.19	0.0040627	Varies

Atoms in the outmost layer of both few-layer graphene walls are fixed to their original locations to maintain a fixed volume system, while the remaining atoms throughout the domain were free to move. To develop non-uniform electric field in the surface normal direction, interdigitated electrodes were assigned to the graphene walls as shown in Figure 5.1. Equally distributed charge per molecule were assigned to the negative and positive electrodes with absolute values of 0.0125, 0.02 and 0.025e and their resulting surface charge densities were 0.3, 0.5 and 0.6 C/m², respectively. These surface charge density values are carefully selected in order to have maximum electric field without exceeding breakdown current of graphene sheets (Zhu et al., 2014). Applied surface charge densities are in accordance with the earlier MD studies (Luedtke et al.,

2011, Yen et al., 2012, Yan and Patey 2012, Celebi et al., 2017) and experimental studies (Braslavsky and Lipson 1998, Sunka 2001, Wei et al., 2008).

To calculate long-range Coulombic interactions of the periodic slab system, the particle-particle particle-mesh (PPPM) solver was used. Newton's equations of motion were integrated, by employing the Verlet Algorithm with a time step of 0.001 ps. Simulations were started from the Maxwell-Boltzmann velocity distribution for all molecules at 323K, while NVT ensemble was applied with Nose Hoover thermostat keeping the system at 323K. Initial particle distribution was evolved for 2×10^6 time-steps (2ns) to reach an isothermal steady state. Afterwards, one dimensional heat transfer between graphene sheets was created using the Nose Hoover thermostat applied only to the outmost two graphene sheets of the both few-layer graphene walls. Top and bottom side thermostats were maintained at 363K and 283K temperatures to induce heat flux through the liquid/solid interfaces. At the same time, NVE ensemble was applied to the remaining carbon and water molecules. Simulations were performed for an additional 15×10^6 time-steps (15ns) to ensure that the system attains equilibrium in presence of the heat flux and time averaging is performed after the equilibrium is achieved.

The computational domain was divided into 100 and 130 slab bins with the size of 0.1nm for temperature profiles. Smaller bin size of 0.012nm is achieved with 800 and 1100 slab bins, which were also employed to resolve the fine details of the near wall water density distributions.

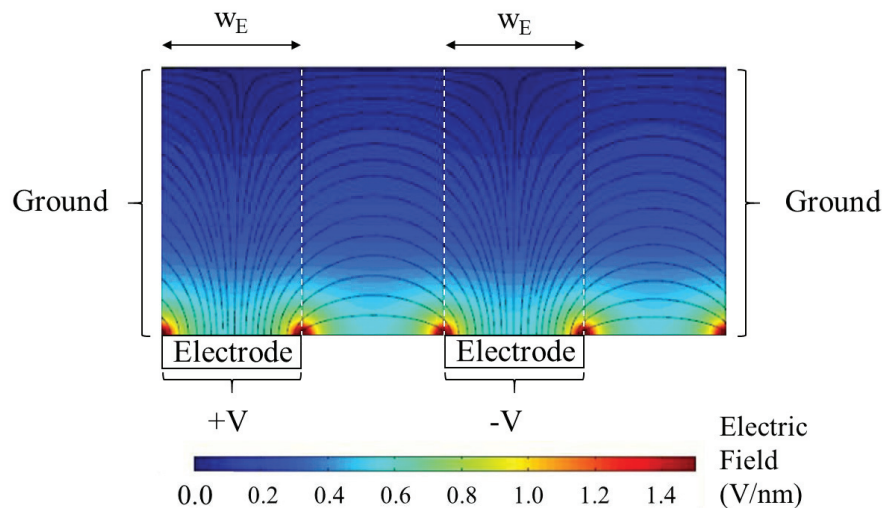


Figure 5.2. Finite element simulation domain for nano-interdigitated electrodes with electric field contour and electric field lines

Further investigations on predicting the spatially non-uniform electric field induced in the water domain were conducted by a commercially available finite element

software. Laplace equation (equation 4.1) was solved using finite-element scheme to calculate the spatial non-uniform electric field (equation 4.2) induced in the water domain in Cartesian coordinates as ϕ is the electrical potential and E is the electric field strength.

As shown in Figure 5.2, a 2D rectangular domain representing the water molecules of the MD simulations was employed. On the bottom wall of the channel multi co-planer electrodes were employed, which were assigned positive and negative electric potentials in sequence. Electrode widths were varied from 0.25nm to 12nm while the applied electric potential is changed directly proportional to the electrode width, to create equal surface charge density. The spacing between two consecutive electrodes was kept same with the corresponding electrode width. Right and left sides of the channel were assigned with ground boundary condition, and the rest of the boundaries were applied as zero charge boundary conditions. In addition, electric field contour and electric field lines of IDEs are documented in Figure 5.2. Electric field gradient towards the surface is created by the presence of two co-planer electrodes and electric field lines are generated between the electrodes. Such a non-homogenous electric field is generated between the edges of the electrodes are described with fringe electric fields. Maxwell first analyzed the fringe electric field of the finite flat plates by defining implicit mapping of the electric field at the edges of the two facing plates charged with positive and negative potential of V_0 , as described in equations 5.1 and 5.2,

$$x = \frac{d}{2\pi} (u + 1 + e^u \cos v) \quad (5.1)$$

$$y = \frac{d}{2\pi} (v + 1 + e^u \sin v) \quad (5.2)$$

where, x is the longitudinal direction to the plates, while y is the perpendicular direction to the plates. Implicitly defined coordinates u varies between $-\infty$ and $+\infty$ and v varies between $-\pi$ and $+\pi$, while d is the spacing between the plates (Metodiev et al., 2014).

By employing this parametric definition, a normalized potential (equation 5.3) can be formed by the implicitly defined coordinate $v(x, y)$.

$$v(x, y) = \frac{\pi V(x, y)}{V_0} \quad (5.3)$$

Then the electric field must follow this potential due to uniqueness theorem. The resulting electric field components in x and y direction are defined by the following formula:

$$E_x = \frac{2V_0}{d} \frac{1 + e^u \sin v}{(1 + 2e^u \cos v + e^{2u})} \quad (5.4)$$

$$E_y = -\frac{2V_0}{d} \frac{1 + e^u \cos v}{(1 + 2e^u \cos v + e^{2u})} \quad (5.5)$$

which can be expressed as $E_x = E \sin \Phi$ and $E_y = E \cos \Phi$, where

$$E = -\frac{2V_0}{d} \frac{1}{\sqrt{1 + 2e^u \cos v + e^{2u}}} \quad (5.6)$$

and

$$\Phi = \arctan \left(\frac{-e^u \sin v}{1 + e^u \cos v} \right). \quad (5.7)$$

The mesh independent results were carefully obtained while using the model parameters of relative permittivity of water as 70.7 similar to value determined for SPC/E water earlier (Reddy and Berkowitz, 1989), electrical conductivity of water as 5.5×10^{-6} S/m and density of water as 0.9982 gr/cm³ at the temperature of 293.15 K.

5.2. Results and Discussion

Electric field contours generated with finite element solver are presented with average electric field intensities calculated 1nm distance away from the surface in Figure 5.3. Increased electrode widths with constant surface charge density created almost equal electric field intensity near wall regions, while getting away from the surface affected area of electric field is increased with the increased electrode width. Such discrepancy is occurred due to increased electric field fringing effect. When two co-planer electrodes with opposite charges were employed, electric field is generated in between them and as getting away from the plane where electrodes are located, the electric field intensity diminishes with respect to the applied charge, electrode width and the distance between

the electrodes. Moreover, high electric field strength values are observed at the corners of the electrodes, which is called edge effect. Basically, surface charge density increases at the edges due to charges moving towards the corners of the electrodes, resulting in increased electric field intensity (Barrachina et al., 2012). However, in molecular dynamics simulations, charges do not transfer between molecules. So, no edge effect is expected to be observed in electric field simulated in the current molecular dynamics system. Moreover, in order to characterize the electric field intensity levels with varying electrode lengths, electric field intensity values in the region 1nm away from the surface are averaged and documented in Figure 5.3(p). 1nm distance is chosen specifically, because in molecular dynamics studies first hydration shell of water molecules falls within this region. In addition, as expected electric field intensity increases with increased surface charge density and electrode width at 1nm distance away from the surface. However, increasing the electrode width after 3nm does not change the electric field intensity at 1nm distance away from the surface, since the electric field intensity reaches saturation point with the applied surface charge density. One important outcome of Figure 5.3 is that the electric field intensity diminishes before it reaches the encountering surface. Therefore, using IDEs enabled to create non-uniform electric field with an increasing electric field intensity gradient towards the surface, which promotes an interface localized force through liquid dielectrophoresis.

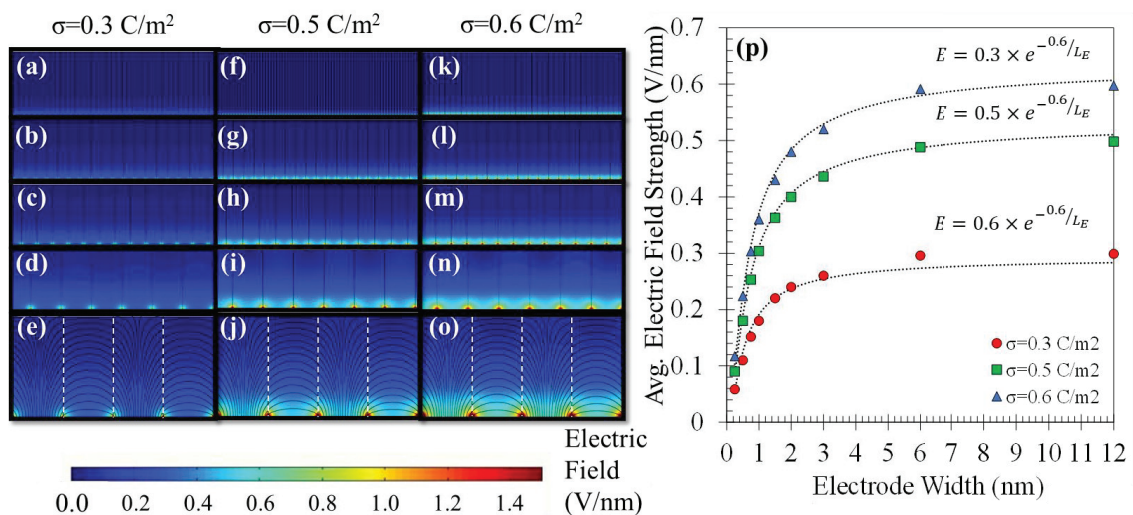


Figure 5.3. Electric field contours for surface charge densities of (a-e) 0.3, (f-j) 0.5 and (k-o) 0.6 C/m² with electrode widths of 0.5, 1, 1.5, 3 and 5nm and (p) average electric field strength values at 1nm away from the surface for varying electrode widths

The resulting density contour of the spatially non-uniform electric field created by the interdigitated electrodes of 3nm width case with surface charge density of 0.6 C/m^2 is documented in Figure 5.4. Density contour shows the well-known density layers at both near wall regions created by Van der Waals force field of the surface and the electric field. While two distinct density peaks are observed at each wall, the density of the water molecules sufficiently away from the wall reaches its thermodynamic value of 1 gr/cm^3 . There is no evidence of local density variations in the longitudinal direction where multiple electrodes are placed even with a high electric field gradient case. The density peak near IDE is constant along the wall and higher than the density peak near the opposing wall, which agrees with the electric field contour documented in Figure 5.3(n). The electric field gradient is in surface normal direction, which is why the water molecules are drawn to the IDE surface equally by the liquid dielectrophoresis phenomena. After revealing that the density distributions are identical all along the channel wall, it is safe to resume the investigations with 1-D density distributions.

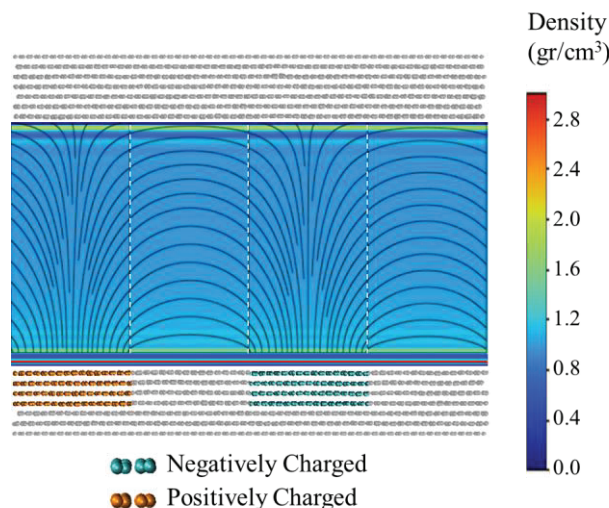


Figure 5.4. Density contour of water molecules for IDE with 3nm electrode width and 0.6 C/m^2 surface charge density

After proving that density contour documented in Figure 5.4 shows no local change in density and the density of the water sufficiently away from the surface reaches thermodynamics density value, only the variation of the near wall density of the water molecules under different electrode widths of 0, 0.5, 1, 1.5, 3 and 5 nm and surface charge density of 0.3, 0.5 and 0.6 C/m^2 are documented in Figure 5.5. Well known density layering effect increases with both increased electrode width and surface charge density. Increased electrode width increases the area affected from the electric field intensity at near wall region, so higher dielectrophoretic force is applied on the water molecules

towards the surface with IDEs. Hence, more water molecules are drawn closer to the surface. In addition, as expected the density peaks are higher for higher surface charge density cases. As a result of increased electrode width and surface charge density, the number of molecules in near wall regions increase, which enhances the interfacial energy of the initially hydrophobic graphene surface. Quantitatively, while the density peak caused only by the van der Waals forces between the carbon and water molecules is 2.5 gr/cm^3 , when dielectrophoretic forces are incorporated into the phenomenon density peak increases up to 4.8 gr/cm^3 . However, after increasing the electrode width up to 5 nm , first density peak does not change, which is in accordance with the electric field intensity level reaching its saturation point as documented in Figure 5.3(p). However, with increased electrode width, electric field intensity levels are increasing after passing beyond 1 nm distance, thus even though the first density peaks stay constant, second density peaks are increasing when the electrode width is increased from 3 nm to 5 nm for every surface charge density value investigated.

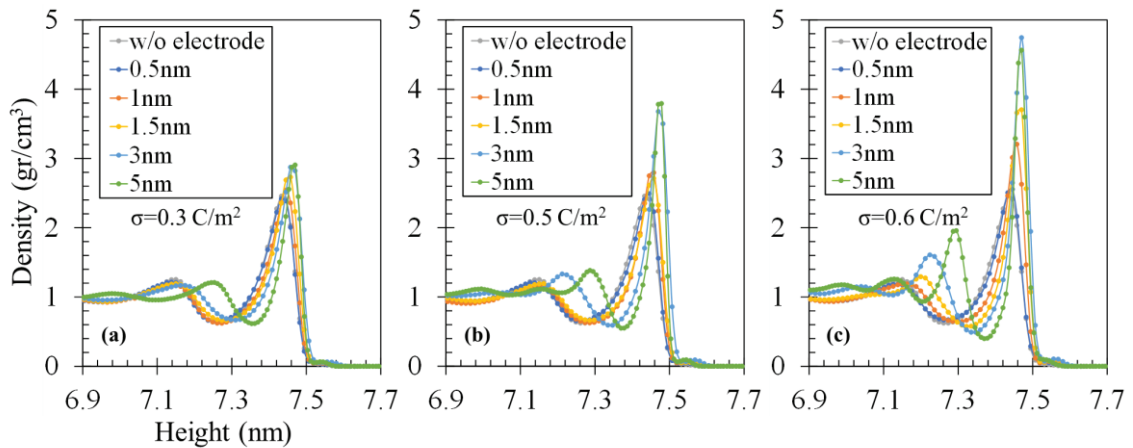


Figure 5.5. Near wall density distributions of water molecules for different electrode widths and for surface charge densities of (a) 0.3 C/m^2 , (b) 0.5 C/m^2 and (c) 0.6 C/m^2

To further investigate the effects of electric field generated by the IDEs, water dipole moment vectors are calculated in two-dimensional space and their directions are documented in Figure 5.6 for varying electrode width and surface charge density. Since liquid dielectrophoresis is an interface localized phenomenon, only the bottom wall and the water molecules near it are documented in Figure 5.6. In agreement with electric field contours given in Figure 5.4, dipole moment vectors of water molecules are distributed randomly when away from the IDEs, since they are outside of the effective range of electric field. On the contrary, water dipole moment vectors are following electric field

lines near the bottom wall, where IDEs are placed. Furthermore, with increased electrode width and surface charge density, more dipole vectors are affected from the electric field and followed the electric field lines showed in Figure 5.3. In addition, in accordance with density profiles, the origins of dipole vectors are in line with each other at near wall locations, but their orientations are in line with electric field lines. These findings support the fact that in the presence of non-uniform electric field, water molecules both attracted towards the higher electric field gradient and orient along the electric field lines.

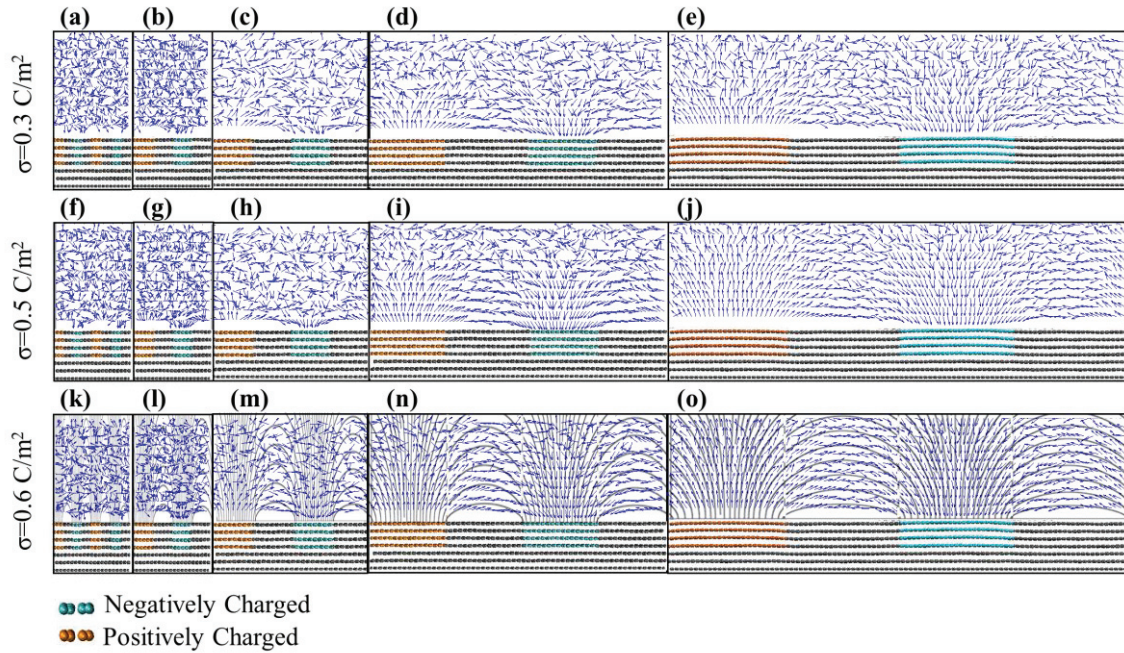


Figure 5.6. Dipole vectors of water molecules for nano-interdigitated electrodes with surface charge densities of (a-e) 0.3 C/m^2 , (f-j) 0.5 C/m^2 and (k-o) 0.6 C/m^2 with 0.5, 1, 1.5, 3 and 5nm electrode widths, respectively

Next, by assigning 283K and 363K to the top and bottom outmost graphene sheets respectively, one-dimensional heat transfer is developed. Figure 5.7 presents the two-dimensional temperature contour of the water domain with the 3nm electrode width and 0.6 C/m^2 surface charge density. In agreement with density contour of the corresponding case, water temperature distribution shows one-dimensional variation in the heat transfer direction. There is no local variation in the temperature in the longitudinal direction, so the temperature distributions can be examined one dimensionally. Therefore, we studied the temperature distributions of graphene and water under different surface charge densities and electrode widths one-dimensionally. In Figure 5.8, resulting temperature distributions at different electrode widths of 0, 0.5, 1, 1.5, 3 and 5 nm were plotted for surface charge densities of 0.3, 0.5 and 0.6 C/m^2 for only near wall region where IDEs

are placed. Temperature profiles are linear in the water domain except the very near wall regions, where temperature profile fluctuates due to the density layering. In addition, sudden temperature jumps are observed at the graphene/water interface, which are caused by a very well-known phenomenon, interfacial thermal resistance (ITR). The ITR is a result of phonon mismatch at the graphene/water interface, and it can be characterized by a thermal resistance length (L_K), known as Kapitza Length. The definition of Kapitza Length (L_K) is the extrapolation of the temperature profile of the liquid in to the solid, where the wall temperature is reached. Moreover, as electrode width and surface charge density are increasing, the temperature jump at the graphene/water interface is decreased in accordance with the electric field gradients and density peaks shown in Figures 5.3 and 5.5. Specifically, the temperature jump at the graphene/water interface is decreased from 23.5 K to 1.5 K. Such a drastic reduction in temperature jump is solely due to the liquid dielectrophoretic forces acting on the water molecules as a bulk force towards the higher electric field gradient region and increasing the pressure at the surface, thus increasing the interface energy between the surface and the liquid. In order to point out the effectiveness of non-uniform electric field, a comparison can be made with the effect of uniform electric field studied in Chapter 4. While the temperature jump between the graphene and water molecules is approximately 10 K with uniform electric field application, it is 1.5 K for the same effective electric field intensity value with non-uniform electric field. The discrepancy comes from the fact that while the uniform electric field can only exert a torque on the water molecules and increased the electrostatic interactions at graphene/water interface, non-uniform electric field can apply an additional bulk force on the water molecules towards the higher electric field gradient region, which occurs towards graphene surface with nano-interdigitated electrodes.

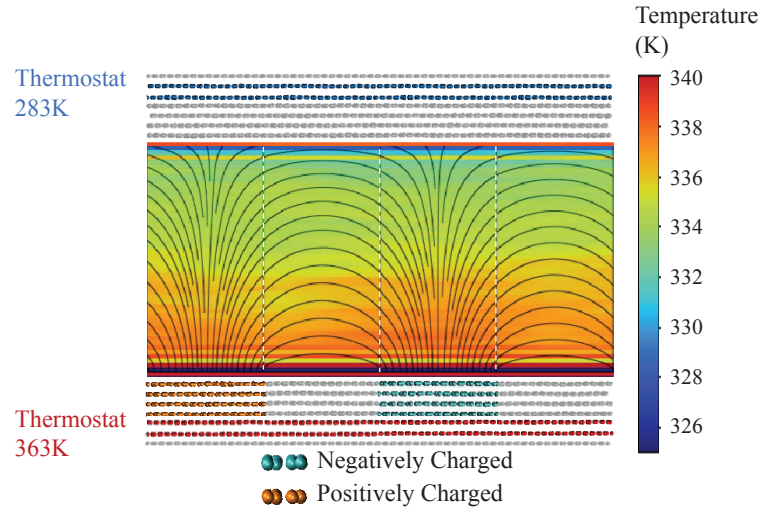


Figure 5.7. Temperature contour of water molecules for IDE with 3nm electrode

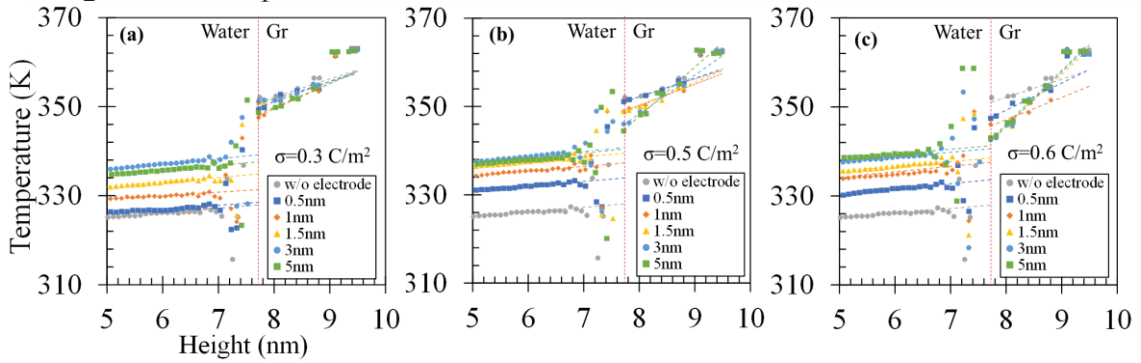


Figure 5.8. Temperature distribution of water and carbon molecules for different electrode widths and for surface charge densities of (a) 0.3 C/m^2 (b) 0.5 C/m^2 and (c) 0.6 C/m^2

The interface thermal resistances were characterized by calculating Kapitza Lengths. Kapitza length (L_K) was calculated using the following relation,

$$L_K = \frac{\Delta T}{\left(\frac{\partial T}{\partial z}\right)_{\text{liquid}}} \quad (5.8)$$

where, ΔT is the temperature jump at the liquid/solid interface and $\partial T/\partial z$ the temperature gradient of the liquid. Results of ITR in terms of Kapitza Length are represented in Figure 5.9 for cold wall, where no electric field effect is present and for hot wall, where IDEs are placed. Figure 5.9 documents the variation of Kapitza Length with respect to electrode width and surface charge density. In the cold wall side, the changes in the Kapitza Length are insignificant, since in all the cases the electric field intensity near the cold wall is negligible. These insignificant changes are caused by the nature of the statistical mechanics. Such results are designed intentionally, to localize the electric field effects on only one surface. Furthermore, on the hot wall side where nano-interdigitated electrodes are located, with increasing electrode width, Kapitza Length

shows a drastic exponential decrease and with increased surface charge density Kapitza Length reaches ultra-low values. Specifically, at 5nm electrode length, Kapitza Length reduces by 57%, 82% and 95% when compared to the Kapitza Length of zero-electric field case, with surface charge densities of 0.3 C/m^2 , 0.5 C/m^2 and 0.6 C/m^2 , respectively. The reducing interface thermal resistance is the result of improved surface wetting created by the liquid dielectrophoresis phenomenon (i.e., increased near surface water density as a function of surface charge density enhances solid/liquid coupling) and an additional heat dissipation channel created by the Coulombic interactions between the charged carbon atoms and water molecules. Moreover, increasing electrode width from 3 to 5nm does not affect the interface thermal resistance, which is in accordance with the same level of first density peak of the water molecules near wall region. However, it points out a different phenomenon, as documented in Figure 5.5, with increased electrode width from 3 to 5nm, second density peak increases, which means that second density peak does not affect the interface energy between graphene and water, only the first density peak affects.

In addition, Kapitza Length values of the corresponding surface charge densities from previous chapter, where we implemented two oppositely charged electrodes at two facing graphene walls to create uniform electric field, were inserted for comparison. In the previous study, it was shown that applying uniform electric field can only decrease the ITR down to a point until electro-freezing occurs at the water domain and limits the heat transfer process. However, by applying non-uniform electric field via IDEs, the effective range of electric field is limited at the interface so that water molecules do not enter a crystal-like structure. In addition, with applying non-uniform electric field throughout the surface, a bulk force is generated towards the surface, which increased the pressure at the surface. As a result, further increase in the heat transfer is achieved. Specifically, while applying uniform electric field can decrease the interface thermal resistance down to 5 nm, applying non-uniform electric field via IDEs decreases it down to 1.2 nm.

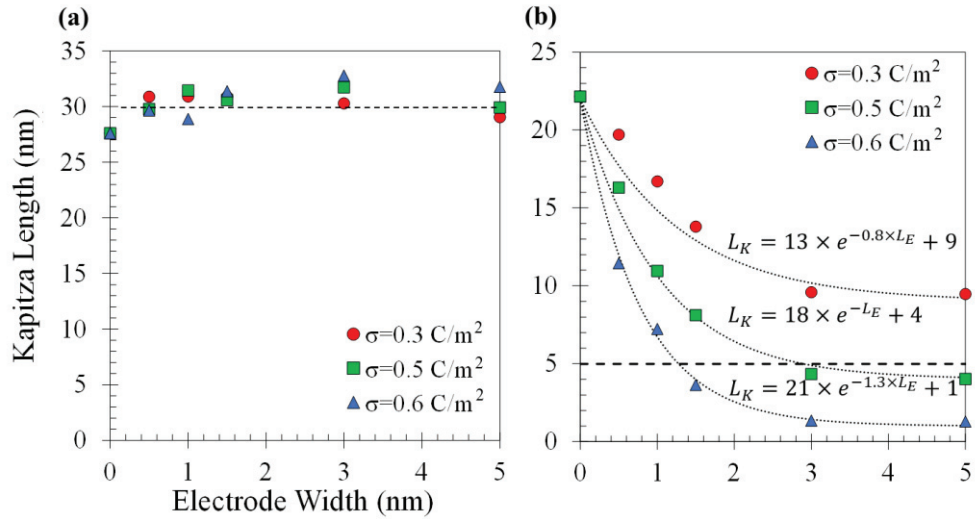


Figure 5.9. Kapitza Length values for different electrode widths and surface charge densities for (a) hot wall, where IDEs are placed and (b) cold wall

Next, a further characterization of the effect of electric field created by the nano-interdigitated electrodes on Kapitza Length is conducted. An attempt is made to correlate the empirical results of Kapitza Length and average electric field intensity 1nm away from the surface by eliminating the electrode width. The purpose of this attempt is to create a complete understanding for the interface-localized heat transfer process independent from electrode dimensions. In Figure 5.10, variation of Kapitza Length with average electric field strength 1 nm away from the surface is documented for different surface charge densities. As expected Kapitza Length values became independent from electrode widths and surface charge densities; all Kapitza Length values follow the same linear relation depending on electric field intensity. Figure 5.10 represents the physics behind the electrode configurations; no matter what the electrode dimension or applied surface charge density is, electric field intensity generated near the surface is the main driving factor for heat transfer enhancement. Furthermore, the obtained linear variation is caused by the fact that both Kapitza Length and average electric field intensity was exponentially dependent on electrode width as documented in Figures 5.3(p) and 5.9(b). Moreover, the linear variation of the Kapitza Length shows agreement with the studies documented in Chapters 3 and 4, where with applied uniform electric field throughout the channel, Kapitza Length was decreasing linearly with increasing electric field strength until electro-freezing occurs. The main difference of the present study is that, since the electric field generated by the IDEs is interface-localized, it does not affect all water molecules to align them in a solid-like ordering, hence electro-freezing never occurs. Consequently, heat transfer process is not interrupted by the electro-freezing phenomenon

and the Kapitza Length is able to be decreased even further with increased electric field strength.

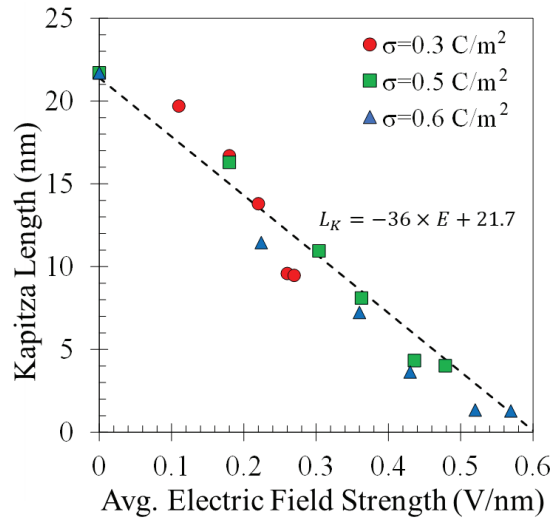


Figure 5.10. Kapitza Length variation with average electric field strength 1nm away from the surface for different surface charge densities

As a result, heat flux values vary with average interface electric field intensity and normalized heat fluxes are documented in Figure 5.11 for different surface charge densities. Heat flux values are normalized with the heat flux of the zero-charge system and with increasing average interface electric field intensity heat flux of the system increases above 1.5 times. Such increase in the heat transfer rate is owed to the decrease of ITR under non-uniform electric field created by nano-interdigitated electrodes. As Kapitza Length, variation of normalized heat flux depending on average interface electric field intensity is linear. This result supports the concept of interface-localized heat transfer enhancement through nano-interdigitated electrodes, since it points out that the only change in the system resistance is the interface thermal resistance at IDE surface.

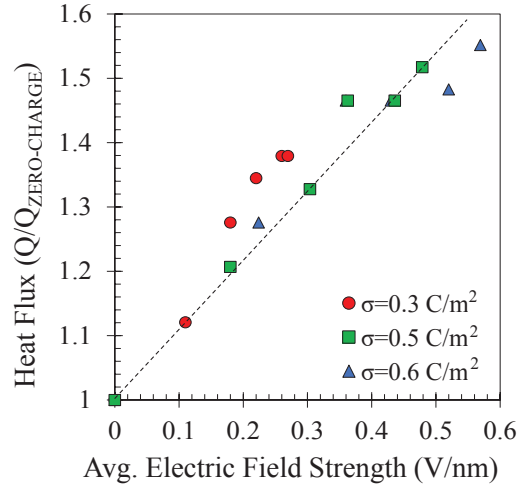


Figure 5.11. Normalized heat flux values for average interface electric field strength for different surface charge density and electrode widths

In order to verify these findings, thermal resistance of the system and its components are calculated and documented in Table 5.2 for different surface charge density and electrode widths. Basically, total thermal resistance of the system can be written as,

$$R_{TOTAL} = R_{GR-COLD} + R_{INT-COLD} + R_{WATER} + R_{INT-HOT} + R_{GR-HOT} \quad (5.9)$$

Total thermal resistance of the system is calculated with equation 5.10, where ΔT_{TOTAL} is the total temperature difference between the thermostats of the system and Q is the total heat flux of the system. Thermal resistance created by the water is calculated by equation 5.11, where H is the channel height, k is the thermal conductivity of water. Thermal resistance at graphene/water interfaces (i.e., Kapitza Resistance) is calculated with equation 5.12, where $\Delta T_{INTERFACE}$ is the temperature jump at graphene/water interface. In addition, thermal resistance of graphene walls is obtained from subtracting the other thermal resistance components from the total thermal resistance, which also includes the artificial thermal resistance at the graphene/thermostat interface, created by the applied thermostats (Barisik and Beskok, 2012). As documented in Table 5.2, the only significant difference in the thermal resistances by the change of surface charge density and electrode width is the variation in Kapitza Resistance at hot surface, expect the thermal resistance of water with 5nm electrodes. The reason for the sudden change in the thermal resistance of water with 5nm electrodes is that the channel height of the water

domain was increased to accommodate the electric field created by 5nm electrodes within the interface of IDE wall. Furthermore, the significance of the interface thermal resistances for the current system are documented in Table 5.2 as well. When there is no effect of electric field, interface thermal resistances compose the 29% and 36% of the total thermal resistance for hot and cold surfaces, respectively. Moreover, with non-uniform electric field is introduced to the system via IDEs, interface thermal resistance of the hot surface is reduced 96%, hence almost cancelled out its effect on the total thermal resistance of the system. Consequently, total thermal resistance of the system is decreased to 66% of its initial value. It is evident that this reduction is solely caused by the reduction of interface thermal resistance of hot surface, which formed the 29% of the total thermal resistance in the first place. As a result, the increase of the heat flux of the system with the significant reduction in the ITR is confirmed.

$$R_{TOTAL} = \frac{\Delta T_{TOTAL}}{Q} \quad (5.10)$$

$$R_{WATER} = \frac{H}{k} \quad (5.11)$$

$$R_{INTERFACE} = \frac{\Delta T_{INTERFACE}}{Q} \quad (5.12)$$

Based on these finding, it is necessary to show the effect of the interface thermal resistance on bigger systems by extrapolating the thermal resistance of the system. Total thermal resistance of the system with varying system height and corresponding proportions of hot and cold surfaces ITR's are documented in Figure 5.12. Increased total thermal resistance is obtained by increasing the thermal resistance of water with channel height and keeping the rest of the resistance components constant. While the channel height is 5nm, interface thermal resistance is 7 times higher than the water's thermal resistance, which shows how dominant interfacial thermal resistance in the current system. However, as channel height increases the effect of interface thermal resistance quickly decreases. As a result, effective range of ITR in terms of system height is observed as ITR of the hot wall is decreased from 29% to 4% and combined ITR of both hot and cold wall is decreased from 66% to 11% as the system height is increased to 500nm. These findings give a complete understanding on the effectiveness of the use of nano-interdigitated electrodes. While using IDE on both walls of the channel can reduce

the 65% of the total thermal resistance on small scale systems, use of IDEs loses its significance over increased system height.

Table 5.1. Total and component-wise thermal resistance of the current system

σ (C/m ²)	w_E (nm)	Q (GW/ m ²)	R_{TOTAL} $\times 10^8$ (m ² K/W)	R_{WATER} $\times 10^8$ (m ² K/W)	$R_{INT-HOT}$ $\times 10^8$ (m ² K/W)	$R_{INT-COLD}$ $\times 10^8$ (m ² K/W)	R_{GR} $\times 10^8$ (m ² K/W)	$R_{INT-HOT}/R_{TOTAL}$ (%)
0	0	0.58	14	0.71	4.0	5.0	2.1	28.9
0.3	0.5	0.65	12	0.71	3.3	4.6	1.9	26.7
	1	0.79	10	0.72	2.1	3.7	1.8	20.7
	1.5	0.8	10	0.7	2.0	4.2	1.6	19.6
	3	0.84	9.5	0.7	1.4	4.3	1.6	14.4
	5	0.84	9.5	1.1	1.3	3.9	1.6	13.4
0.5	0.5	0.7	11	0.71	2.5	4.5	1.9	21.6
	1	0.77	10	0.71	1.5	4.4	1.9	14.7
	1.5	0.85	9.4	0.7	1.1	4.2	1.7	11.3
	3	0.857	9.3	0.73	0.6	4.4	1.8	6.4
	5	0.88	9.1	1.1	0.92	3.9	1.6	10.2
0.6	0.5	0.74	11	0.7	1.9	4.3	1.9	17.4
	1	0.85	9.4	0.72	0.96	4.1	1.8	10.2
	1.5	0.86	9.3	0.71	0.47	4.3	1.9	5.0
	3	0.85	9.4	0.71	0.18	4.4	2.0	1.9
	5	0.88	9.1	1.1	0.16	4.2	1.8	1.8

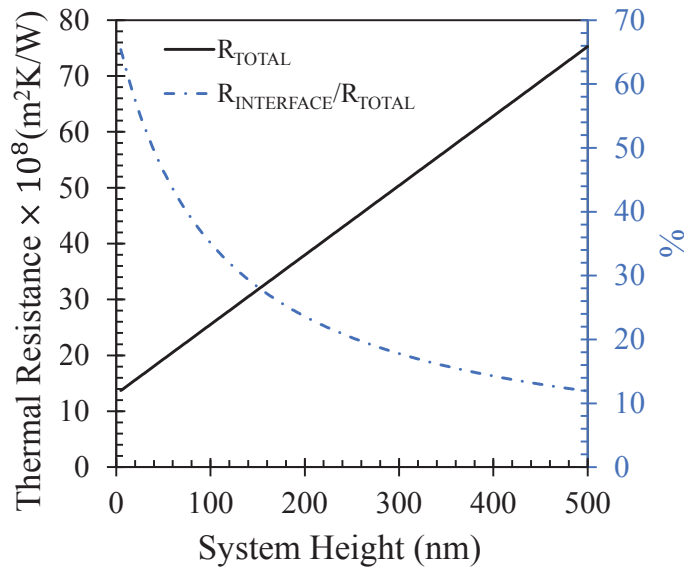


Figure 5.12. Total thermal resistance of the system with varying system height and corresponding proportion of Interface Thermal Resistance of both hot and cold surfaces to the total thermal resistance

5.3. Conclusion

In this chapter, interface-localized heat transfer enhancement by employing interdigitated electrodes (IDEs) over graphene/water interface is studied. Embedding interdigitated electrodes to the surface is created a non-uniform electric field within the channel with an electric field gradient increasing towards the surface. Such phenomenon provided a suitable environment for creating a bulk force over the water molecules, which is called liquid dielectrophoresis (LDEP) and increased the pressure at the surface, where IDEs are located. Both through electrostatic interactions and LDEP phenomenon the graphene/water interface energy is altered. Different configurations of electrode width and surface charge density are studied to characterize the average interface electric field intensity generated by the IDEs. By increasing the near interface electric field intensity with increased electrode width and surface charge density, a reduction of 96% is observed on ITR. As a result, 1.5 times increase is achieved in heat flux by the application of IDEs on one interface. Furthermore, total thermal resistance and its components are calculated for each electrode width and surface charge density values and it is documented that the combined effect of two interface thermal resistance composes 66% of the total thermal resistance on a given system. In addition, system size dependency of the ITR and effective range of IDE usage is investigated. While the combined ITR of two interfaces on a sandwich structure as given in this study forms 66% of the total thermal resistance in 1-10 nm scale, its significance is reduced to order of 10% when the system is in 500nm scale.

CHAPTER 6

SUMMARY

This dissertation employs atomistic level simulations to characterize and control heat transfer mechanisms at the interfaces of liquids and nano-sized channels. Heat transport in nanoscale is investigated with molecular dynamics simulations by characterizing density ordering near interfaces, dipole vector orientations, temperature distributions, interface thermal resistance and thermal conductivity variations and finally heat flux of the systems. Based on these investigations semi-theoretical and empirical relations are proposed to model the interface thermal resistance depending on different parameters.

In Chapter 1, a broad introduction about nano-scale heat transfer and dominant mechanism that governs it are discussed. Different material and surface properties that affect interfacial thermal resistance that discussed in the literature are examined and liquid ordering near the solid interface found to be the most effective parameter. Furthermore, various electric field applications that can possibly alter the solid/liquid coupling are reviewed. Finally, theoretical background on molecular dynamics simulations is documented.

In Chapter 2, effect of solid thickness on interfacial thermal resistance is investigated. The results showed that modified phonon spectrum developing inside the solid substrate as a function of thicknesses creates a size dependency on thermal conductivity. For such a case, it is demonstrated that the variation in phonon distribution is affected the heat transport at the interface as well. The thermal resistance at the interface is characterized by the Kapitza length, which experienced an exponential increase by the decrease of nano-film thickness. Finally, the increase of L_K is correlated with the decrease of thermal conductivity which can provide L_K values for the cases where thermal conductivity of the substrate is known. The results of this study are essential for designing heat removal mechanisms at nano-scale systems.

In Chapter 3, a new nanoscale heat transfer control mechanism is introduced with applying uniform electric field across silicon/water. Under electric field, electrostatic interactions are improved, thus solid/liquid coupling at the interface is enhanced.

Improved solid/liquid coupling at the interface results in substantial decrease of 76% in the interfacial thermal resistance until electric field strength is strong enough to cause electro-freezing. After electro-freezing dominates the entire water domain, Kapitza length remains constant but thermal conductivity of water increases 1.5 times due to enhanced phonon dynamics of highly ordered water molecules. As a result of these two occurrences, heat flux is increased 2.25 times with under uniform electric field while constant temperature difference is applied.

In Chapter 4, a bottleneck for the heat transport across graphene and possible ambient fluid or coolant (i.e., large interface thermal resistance) is resolved with applied uniform and non-uniform electric field. Substantial increases of heat fluxes are observed through applying uniform and non-uniform electric field, due to 86% and 99% reduction on interface thermal resistances, respectively. Prior to electro-freezing both uniform and non-uniform electric field results in similar L_K reduction and heat transfer enhancement. However, ability to collect and distribute heat flow to/from a smaller location from/to a larger region gives an advantage to the non-uniform electric field application at low charge cases. After electro-freezing occurs, heat flux remains constant for uniform electric field application, while increasing electrode charge even further creates higher LDEP forces in the water domain for non-uniform electric field, which increases heat flux even more. Higher LDEP forces create water concentration increase in near electrode regions, which both enhance thermal coupling at the interface and thermal conductivity of water. This study demonstrates a smart thermal management concept that is crucial for local heat transfer control at nanoscale.

In Chapter 5, heat transfer control across graphene/water interface with liquid dielectrophoresis phenomenon is examined from a different perspective, where non-uniform electric field is created throughout the channel by implementing interdigitated electrodes. Interdigitated electrodes with opposite charges create electric field gradient in the surface normal direction throughout the channel, which creates equal LDEP forces everywhere at the surface. As a result, an interface-localized behavior is observed. Due to the fact that LDEP forces are concentrated at the interface, electro-freezing did not occur, hence did not limit the heat transfer enhancement. Furthermore, 96% reduction in interface thermal resistance is documented with a much smaller electrode charge applied in pin and plate electrode configuration. In addition, effective system size range that interdigitated electrodes can be employed is documented. With increasing system

size up to 500nm, total thermal resistance can be decreased between 66% and 10% with the application of LDEP via interdigitated electrodes.

REFERENCES

- Alexeev, D.; Chen, J.; Walther, J. H.; Giapis, K. P.; Angelikopoulos, P.; Koumoutsakos, P., Kapitza Resistance between Few-Layer Graphene and Water: Liquid Layering Effects. *Nano Lett* 2015, 15 (9), 5744-9.
- Asheghi, M.; Touzelbaev, M. N.; Goodson, K. E.; Leung, Y. K.; Wong, S. S., Temperature-Dependent Thermal Conductivity of Single-Crystal Silicon Layers in SOI Substrates. *Journal of Heat Transfer* 1998, 120 (1), 30-36.
- Balandin, A. A.; Ghosh, S.; Bao, W.; Calizo, I.; Teweldebrhan, D.; Miao, F.; Lau, C. N., Superior thermal conductivity of single-layer graphene. *Nano Lett* 2008, 8 (3), 902-7.
- Banpurkar, A. G.; Nichols, K. P.; Mugele, F., Electrowetting-based microdrop tensiometer. *Langmuir* 2008, 24 (19), 10549-51.
- Barisik, M.; Beskok, A., Boundary treatment effects on molecular dynamics simulations of interface thermal resistance. *Journal of Computational Physics* 2012, 231 (23), 7881-7892.
- Barisik, M.; Beskok, A., Wetting characterisation of silicon (1,0,0) surface. *Molecular Simulation* 2013, 39 (9), 700-709.
- Barisik, M.; Beskok, A., Temperature dependence of thermal resistance at the water/silicon interface. *International Journal of Thermal Sciences* 2014, 77, 47-54.
- Barman, J.; Shao, W.; Tang, B.; Yuan, D.; Groenewold, J.; Zhou, G., Wettability Manipulation by Interface-Localized Liquid Dielectrophoresis: Fundamentals and Applications. *Micromachines (Basel)* 2019, 10 (5).
- Barman, J.; Swain, D.; Law, B. M.; Seemann, R.; Herminghaus, S.; Khare, K., Electrowetting actuated microfluidic transport in surface grooves with triangular cross section. *Langmuir* 2015, 31 (3), 1231-6.
- Berendsen, H. J. C.; Grigera, J. R.; Straatsma, T. P., The missing term in effective pair potentials. *The Journal of Physical Chemistry* 2002, 91 (24), 6269-6271.
- Betz, A. R.; Jenkins, J.; Kim, C.-J. C.; Attinger, D., Boiling heat transfer on superhydrophilic, superhydrophobic, and superbiphilic surfaces. *International Journal of Heat and Mass Transfer* 2013, 57 (2), 733-741.
- Braslavsky, I.; Lipson, S. G., Electrofreezing effect and nucleation of ice crystals in free growth experiments. *Applied Physics Letters* 1998, 72 (2), 264-266.

Bueno Barrachina, J. M.; Cañas Peñuelas, C. S.; Catalán Izquierdo, S., FEM edge effect and capacitance evaluation on cylindrical capacitors. *Journal of Energy and Power Engineering* 2012, 6 (12), 2063-2069.

Byun, S. H.; Yuan, J.; Yoon, M. G.; Cho, S. K., Wirelessly powered electrowetting-on-dielectric (EWOD) by planar receiver coils. *Journal of Micromechanics and Microengineering* 2015, 25 (3).

Cao, B.-Y.; Zou, J.-H.; Hu, G.-J.; Cao, G.-X., Enhanced thermal transport across multilayer graphene and water by interlayer functionalization. *Applied Physics Letters* 2018, 112 (4).

Celebi, A. T.; Barisik, M.; Beskok, A., Electric field controlled transport of water in graphene nano-channels. *J Chem Phys* 2017, 147 (16), 164311.

Celestini, F.; Kirstetter, G., Effect of an electric field on a Leidenfrost droplet. *Soft Matter* 2012, 8 (22).

Chae, J. B.; Kwon, J. O.; Yang, J. S.; Kim, D.; Rhee, K.; Chung, S. K., Optimum thickness of hydrophobic layer for operating voltage reduction in EWOD systems. *Sensors and Actuators A: Physical* 2014, 215, 8-16.

Chang, S. W.; Nair, A. K.; Buehler, M. J., Geometry and temperature effects of the interfacial thermal conductance in copper- and nickel-graphene nanocomposites. *J Phys Condens Matter* 2012, 24 (24), 245301.

Chen, B.; Hsieh, W.-P.; Cahill, D. G.; Trinkle, D. R.; Li, J., Thermal conductivity of compressed H₂O to 22 GPa: A test of the Leibfried-Schlömann equation. *Physical Review B* 2011, 83 (13).

Chen, J.; Walther, J. H.; Koumoutsakos, P., Ultrafast cooling by covalently bonded graphene-carbon nanotube hybrid immersed in water. *Nanotechnology* 2016, 27 (46), 465705.

Chen, L.; Bonaccorso, E., Electrowetting -- from statics to dynamics. *Adv Colloid Interface Sci* 2014, 210, 2-12.

Chen, S.; Wang, J.; Ma, T.; Chen, D., Molecular dynamics simulations of wetting behavior of water droplets on polytetrafluorethylene surfaces. *J Chem Phys* 2014, 140 (11), 114704.

Chen, S.; Yang, M.; Liu, B.; Xu, M.; Zhang, T.; Zhuang, B.; Ding, D.; Huai, X.; Zhang, H., Enhanced thermal conductance at the graphene-water interface based on functionalized alkane chains. *RSC Advances* 2019, 9 (8), 4563-4570.

Daub, C. D.; Bratko, D.; Leung, K.; Luzar, A., Electrowetting at the Nanoscale. *The Journal of Physical Chemistry C* 2007, 111 (2), 505-509.

Dieny, B.; Chshiev, M.; Charles, B.; Strelkov, N.; Truong, A.; Fruchart, O.; Hallal, A.; Wang, J.; Takahashi, Y. K.; Mizuno, T.; Hono, K., Impact of Intergrain Spin-Transfer Torques Due to Huge Thermal Gradients in Heat-Assisted Magnetic Recording. *IEEE Transactions on Magnetics* 2018, 54 (12), 1-11.

Dong, Y.; Cao, B.-Y.; Guo, Z.-Y., Size dependent thermal conductivity of Si nanosystems based on phonon gas dynamics. *Physica E: Low-dimensional Systems and Nanostructures* 2014, 56, 256-262.

Duda, J. C.; Kimmer, C. J.; Soffa, W. A.; Zhou, X. W.; Jones, R. E.; Hopkins, P. E., Influence of crystallographic orientation and anisotropy on Kapitza conductance via classical molecular dynamics simulations. *Journal of Applied Physics* 2012, 112 (9).

Edwards, A. M. J.; Brown, C. V.; Newton, M. I.; McHale, G., Dielectrowetting: The past, present and future. *Current Opinion in Colloid & Interface Science* 2018, 36, 28-36.

Evans, W.; Fish, J.; Keblinski, P., Thermal conductivity of ordered molecular water. *J Chem Phys* 2007, 126 (15), 154504.

Fu, Y.; Hansson, J.; Liu, Y.; Chen, S.; Zehri, A.; Samani, M. K.; Wang, N.; Ni, Y.; Zhang, Y.; Zhang, Z.-B.; Wang, Q.; Li, M.; Lu, H.; Sledzinska, M.; Torres, C. M. S.; Volz, S.; Balandin, A. A.; Xu, X.; Liu, J., Graphene related materials for thermal management. *2D Materials* 2019, 7 (1).

Gatapova, E. Y.; Graur, I. A.; Kabov, O. A.; Aniskin, V. M.; Filipenko, M. A.; Sharipov, F.; Tadrist, L., The temperature jump at water – air interface during evaporation. *International Journal of Heat and Mass Transfer* 2017, 104, 800-812.

Ge, Z.; Cahill, D. G.; Braun, P. V., Thermal conductance of hydrophilic and hydrophobic interfaces. *Phys Rev Lett* 2006, 96 (18), 186101.

Giri, A.; Hopkins, P. E., Role of interfacial mode coupling of optical phonons on thermal boundary conductance. *Sci Rep* 2017, 7 (1), 11011.

Gubskaya, A. V.; Kusalik, P. G., The total molecular dipole moment for liquid water. *The Journal of Chemical Physics* 2002, 117 (11), 5290-5302.

Han, H.; Merabia, S.; Muller-Plathe, F., Thermal Transport at Solid-Liquid Interfaces: High Pressure Facilitates Heat Flow through Nonlocal Liquid Structuring. *J Phys Chem Lett* 2017, 8 (9), 1946-1951.

Hemley, R. J.; Jephcoat, A. P.; Mao, H. K.; Zha, C. S.; Finger, L. W.; Cox, D. E., Static compression of H₂O-ice to 128 GPa (1.28 Mbar). *Nature* 1987, 330 (6150), 737-740.

Ho, T. A.; Striolo, A., Molecular dynamics simulation of the graphene–water interface: comparing water models. *Molecular Simulation* 2014, 40 (14), 1190-1200.

Hong, Y.; Li, L.; Zeng, X. C.; Zhang, J., Tuning thermal contact conductance at graphene-copper interface via surface nanoengineering. *Nanoscale* 2015, 7 (14), 6286-94.

Hu, H.; Hou, H.; Wang, B., Molecular Dynamics Simulations of Ice Growth from Supercooled Water When Both Electric and Magnetic Fields Are Applied. *The Journal of Physical Chemistry C* 2012, 116 (37), 19773-19780.

Hu, M.; Zhang, X.; Poulikakos, D.; Grigoropoulos, C. P., Large “near junction” thermal resistance reduction in electronics by interface nanoengineering. *International Journal of Heat and Mass Transfer* 2011.

Huang, Y.; Zhu, C.; Wang, L.; Cao, X.; Su, Y.; Jiang, X.; Meng, S.; Zhao, J.; Zeng, X. C., A new phase diagram of water under negative pressure: The rise of the lowest-density clathrate s-III. *Sci Adv* 2016, 2 (2), e1501010.

Huxtable, S. T.; Cahill, D. G.; Shenogin, S.; Xue, L.; Ozisik, R.; Barone, P.; Usrey, M.; Strano, M. S.; Siddons, G.; Shim, M.; Keblinski, P., Interfacial heat flow in carbon nanotube suspensions. *Nat Mater* 2003, 2 (11), 731-4.

Iriarte-Carretero, I.; Gonzalez, M. A.; Bresme, F., Thermal conductivity of ice polymorphs: a computational study. *Phys Chem Chem Phys* 2018, 20 (16), 11028-11036.

Janecek, J.; Netz, R. R., Interfacial water at hydrophobic and hydrophilic surfaces: depletion versus adsorption. *Langmuir* 2007, 23 (16), 8417-29.

Jiang, Q. G.; Ao, Z. M.; Chu, D. W.; Jiang, Q., Reversible Transition of Graphene from Hydrophobic to Hydrophilic in the Presence of an Electric Field. *The Journal of Physical Chemistry C* 2012, 116 (36), 19321-19326.

Jones, R. E.; Duda, J. C.; Zhou, X. W.; Kimmer, C. J.; Hopkins, P. E., Investigation of size and electronic effects on Kapitza conductance with non-equilibrium molecular dynamics. *Applied Physics Letters* 2013, 102 (18).

Jones, S.; Andr n, D.; Karpinski, P.; K ll, M., Photothermal Heating of Plasmonic Nanoantennas: Influence on Trapped Particle Dynamics and Colloid Distribution. *ACS Photonics* 2018, 5 (7), 2878-2887.

Jones, T. B., Liquid dielectrophoresis on the microscale. *Journal of Electrostatics* 2001, 51-52, 290-299.

Ju, G.; Peng, Y.; Chang, E. K. C.; Ding, Y.; Wu, A. Q.; Zhu, X.; Kubota, Y.; Klemmer, T. J.; Amini, H.; Gao, L.; Fan, Z.; Rausch, T.; Subedi, P.; Ma, M.; Kalarickal, S.; Rea, C. J.; Dimitrov, D. V.; Huang, P.-W.; Wang, K.; Chen, X.; Peng, C.; Chen, W.; Dykes, J. W.; Seigler, M. A.; Gage, E. C.; Chantrell, R.; Thiele, J.-U., High Density Heat-Assisted Magnetic Recording Media and Advanced Characterization—Progress and Challenges. *IEEE Transactions on Magnetics* 2015, 51 (11), 1-9.

Ju, Y. S.; Goodson, K. E., Phonon scattering in silicon films with thickness of order 100 nm. *Applied Physics Letters* 1999, 74 (20), 3005-3007.

Kalluri, R. K.; Konatham, D.; Striolo, A., Aqueous NaCl Solutions within Charged Carbon-Slit Pores: Partition Coefficients and Density Distributions from Molecular Dynamics Simulations. *The Journal of Physical Chemistry C* 2011, 115 (28), 13786-13795.

Kapitza, P., Heat transfer and superfluidity of helium II. *Physical Review* 1941, 60 (4), 354.

Kim, B., Thermal resistance at a liquid–solid interface dependent on the ratio of thermal oscillation frequencies. *Chemical Physics Letters* 2012, 554, 77-81.

Kwon, T. W.; Jang, J.; Ambrosia, M. S.; Ha, M. Y., Molecular dynamics study on the hydrophobicity of a surface patterned with hierarchical nanotextures. *Colloids and Surfaces A: Physicochemical and Engineering Aspects* 2018, 559, 209-217.

Landry, E. S.; McGaughey, A. J. H., Thermal boundary resistance predictions from molecular dynamics simulations and theoretical calculations. *Physical Review B* 2009, 80 (16).

Larry Caretto, D. M., Tom Mincer, Spreadsheet Calculations of Thermodynamics Properties. *Proceeding of the 2005 American Society for Engineering Education Annual Conference and Exposition* 2005.

Lee, J.; Moon, H.; Fowler, J.; Schoellhammer, T.; Kim, C.-J., Electrowetting and electrowetting-on-dielectric for microscale liquid handling. *Sensors and Actuators A: Physical* 2002, 95 (2-3), 259-268.

Lee, M. W.; Latthe, S. S.; Yarin, A. L.; Yoon, S. S., Dynamic electrowetting-on-dielectric (DEWOD) on unstretched and stretched teflon. *Langmuir* 2013, 29 (25), 7758-67.

- Li, B.; Tan, K. T.; Christensen, J., Tailoring the thermal conductivity in nanophononic metamaterials. *Physical Review B* 2017, 95 (14).
- Li, J.; Zhou, L.; Yang, N.; Gao, C.; Zheng, Y., Robust superhydrophobic coatings with micro- and nano-composite morphology. *RSC Advances* 2017, 7 (70), 44234-44238.
- Liang, Z.; Keblinski, P., Finite-size effects on molecular dynamics interfacial thermal-resistance predictions. *Physical Review B* 2014, 90 (7).
- Liang, Z.; Sasikumar, K.; Keblinski, P., Thermal transport across a substrate-thin-film interface: effects of film thickness and surface roughness. *Phys Rev Lett* 2014, 113 (6), 065901.
- Liu, W.; Asheghi, M., Phonon–boundary scattering in ultrathin single-crystal silicon layers. *Applied Physics Letters* 2004, 84 (19), 3819-3821.
- Liu, W.; Asheghi, M., Phonon–boundary scattering in ultrathin single-crystal silicon layers. *Applied Physics Letters* 2004, 84 (19), 3819-3821.
- Liu, W.; Asheghi, M., Phonon–boundary scattering in ultrathin single-crystal silicon layers. *Applied Physics Letters* 2004, 84 (19), 3819-3821.
- Liu, X.; Zhang, G.; Zhang, Y. W., Topological Defects at the Graphene/h-BN interface Abnormally Enhance Its Thermal Conductance. *Nano Lett* 2016, 16 (8), 4954-9.
- Luedtke, W. D.; Gao, J.; Landman, U., Dielectric Nanodroplets: Structure, Stability, Thermodynamics, Shape Transitions and Electrocrystallization in Applied Electric Fields. *The Journal of Physical Chemistry C* 2011, 115 (42), 20343-20358.
- Lundgren, M.; Allan, N. L.; Cosgrove, T.; George, N., Molecular Dynamics Study of Wetting of a Pillar Surface. *Langmuir* 2003, 19 (17), 7127-7129.
- Ma, Y., Size-dependent thermal conductivity in nanosystems based on non-Fourier heat transfer. *Applied Physics Letters* 2012, 101 (21).
- Ma, Y.; Zhang, Z.; Chen, J.; Sääskilähti, K.; Volz, S.; Chen, J., Ordered water layers by interfacial charge decoration leading to an ultra-low Kapitza resistance between graphene and water. *Carbon* 2018, 135, 263-269.
- Mao, Y.; Zhang, Y., Thermal conductivity, shear viscosity and specific heat of rigid water models. *Chemical Physics Letters* 2012, 542, 37-41.
- McCoustra, M. R., Water at interfaces. *Phys Chem Chem Phys* 2008, 10 (32), 4676-7.

McHale, G.; Brown, C. V.; Newton, M. I.; Wells, G. G.; Sampara, N., Dielectrowetting driven spreading of droplets. *Phys Rev Lett* 2011, 107 (18), 186101.

Meier, T.; Menges, F.; Nirmalraj, P.; Holscher, H.; Riel, H.; Gotsmann, B., Length-dependent thermal transport along molecular chains. *Phys Rev Lett* 2014, 113 (6), 060801.

Merabia, S.; Termentzidis, K., Thermal conductance at the interface between crystals using equilibrium and nonequilibrium molecular dynamics. *Physical Review B* 2012, 86 (9).

Metodiev, E. M.; Huang, K. L.; Semertzidis, Y. K.; Morse, W. M., Fringe electric fields of flat and cylindrical deflectors in electrostatic charged particle storage rings. *Physical Review Special Topics - Accelerators and Beams* 2014, 17 (7).

Motezakker, A. R.; Sadaghiani, A. K.; Akkoc, Y.; Parapari, S. S.; Gozuacik, D.; Kosar, A., Surface modifications for phase change cooling applications via crenarchaeon *Sulfolobus solfataricus* P2 bio-coatings. *Sci Rep* 2017, 7 (1), 17891.

Mugele, F.; Baret, J.-C., Electrowetting: from basics to applications. *Journal of Physics: Condensed Matter* 2005, 17 (28), R705-R774.

Murad, S.; Puri, I. K., Molecular simulation of thermal transport across hydrophilic interfaces. *Chemical Physics Letters* 2008, 467 (1-3), 110-113.

Nomura, M.; Shiomi, J.; Shiga, T.; Anufriev, R., Thermal phonon engineering by tailored nanostructures. *Japanese Journal of Applied Physics* 2018, 57 (8).

Orejon, D.; Sefiane, K.; Shanahan, M. E. R., Young-Lippmann equation revisited for nano-suspensions. *Applied Physics Letters* 2013, 102 (20).

Pellat, H., Mesure de la force agissant sur les diélectriques liquides non électrisés placés dans un champ élitrique. *CR Acad. Sci. Paris* 1895, 119, 691-694.

Pham, A.; Barisik, M.; Kim, B., Pressure dependence of Kapitza resistance at gold/water and silicon/water interfaces. *J Chem Phys* 2013, 139 (24), 244702.

Pham, A. T.; Barisik, M.; Kim, B., Molecular dynamics simulations of Kapitza length for argon-silicon and water-silicon interfaces. *International Journal of Precision Engineering and Manufacturing* 2014, 15 (2), 323-329.

Pham, A. T.; Barisik, M.; Kim, B., Interfacial thermal resistance between the graphene-coated copper and liquid water. *International Journal of Heat and Mass Transfer* 2016, 97, 422-431.

Plimpton, S., Fast Parallel Algorithms for Short-Range Molecular Dynamics. *Journal of Computational Physics* 1995, 117 (1), 1-19.

Pollack, G. L., Kapitza Resistance. *Reviews of Modern Physics* 1969, 41 (1), 48-81.

Pollack, M. G.; Fair, R. B.; Shenderov, A. D., Electrowetting-based actuation of liquid droplets for microfluidic applications. *Applied Physics Letters* 2000, 77 (11), 1725-1726.

Qian, C.; Wang, Y.; He, H.; Huo, F.; Wei, N.; Zhang, S., Lower Limit of Interfacial Thermal Resistance across the Interface between an Imidazolium Ionic Liquid and Solid Surface. *The Journal of Physical Chemistry C* 2018, 122 (38), 22194-22200.

Rami Reddy, M.; Berkowitz, M., The dielectric constant of SPC/E water. *Chemical Physics Letters* 1989, 155 (2), 173-176.

Razeeb, K. M.; Dalton, E.; Cross, G. L. W.; Robinson, A. J., Present and future thermal interface materials for electronic devices. *International Materials Reviews* 2017, 63 (1), 1-21.

Renteria, J.; Nika, D.; Balandin, A., Graphene Thermal Properties: Applications in Thermal Management and Energy Storage. *Applied Sciences* 2014, 4 (4), 525-547.

Sadaghiani, A. K.; Motezakker, A. R.; Kasap, S.; Kaya, II; Kosar, A., Foamlike 3D Graphene Coatings for Cooling Systems Involving Phase Change. *ACS Omega* 2018, 3 (3), 2804-2811.

Saleman, A. R. b.; Chilukoti, H. K.; Kikugawa, G.; Shibahara, M.; Ohara, T., A molecular dynamics study on the thermal energy transfer and momentum transfer at the solid-liquid interfaces between gold and sheared liquid alkanes. *International Journal of Thermal Sciences* 2017, 120, 273-288.

Sam Huang, H.; Varshney, V.; Wohlwend, J. L.; Roy, A. K., Heat Transfer at Aluminum–Water Interfaces: Effect of Surface Roughness. *Journal of Nanotechnology in Engineering and Medicine* 2012, 3 (3).

Schelling, P. K.; Phillpot, S. R.; Keblinski, P., Comparison of atomic-level simulation methods for computing thermal conductivity. *Physical Review B* 2002, 65 (14).

Sellan, D. P.; Landry, E. S.; Turney, J. E.; McGaughey, A. J. H.; Amon, C. H., Size effects in molecular dynamics thermal conductivity predictions. *Physical Review B* 2010, 81 (21).

Seon, Y.; Chang, J.; Yoo, C.; Jeon, J., Device and Circuit Exploration of Multi-Nanosheet Transistor for Sub-3 nm Technology Node. *Electronics* 2021, 10 (2).

- Shahil, K. M. F.; Balandin, A. A., Thermal properties of graphene and multilayer graphene: Applications in thermal interface materials. *Solid State Communications* 2012, 152 (15), 1331-1340.
- Shahriari, A.; Birbarah, P.; Oh, J.; Miljkovic, N.; Bahadur, V., Electric Field-Based Control and Enhancement of Boiling and Condensation. *Nanoscale and Microscale Thermophysical Engineering* 2016, 21 (2), 102-121.
- Shahriari, A.; Wuruz, J.; Bahadur, V., Heat transfer enhancement accompanying Leidenfrost state suppression at ultrahigh temperatures. *Langmuir* 2014, 30 (40), 12074-81.
- Shenogina, N.; Godawat, R.; Keblinski, P.; Garde, S., How wetting and adhesion affect thermal conductance of a range of hydrophobic to hydrophilic aqueous interfaces. *Phys Rev Lett* 2009, 102 (15), 156101.
- Shi, Z.; Barisik, M.; Beskok, A., Molecular dynamics modeling of thermal resistance at argon-graphite and argon-silver interfaces. *International Journal of Thermal Sciences* 2012, 59, 29-37.
- Smith, J.; Singh, R.; Hinterberger, M.; Mochizuki, M., Battery thermal management system for electric vehicle using heat pipes. *International Journal of Thermal Sciences* 2018, 134, 517-529.
- Somada, H.; Hirahara, K.; Akita, S.; Nakayama, Y., A molecular linear motor consisting of carbon nanotubes. *Nano Lett* 2009, 9 (1), 62-5.
- Song, F. H.; Li, B. Q.; Liu, C., Molecular dynamics simulation of nanosized water droplet spreading in an electric field. *Langmuir* 2013, 29 (13), 4266-74.
- Song, G.; Min, C., Temperature dependence of thermal resistance at a solid/liquid interface. *Molecular Physics* 2013, 111 (7), 903-908.
- Spori, D. M.; Drobek, T.; Zurcher, S.; Ochsner, M.; Sprecher, C.; Muhlebach, A.; Spencer, N. D., Beyond the lotus effect: roughness influences on wetting over a wide surface-energy range. *Langmuir* 2008, 24 (10), 5411-7.
- Stillinger, F. H.; Weber, T. A., Computer simulation of local order in condensed phases of silicon. *Phys Rev B Condens Matter* 1985, 31 (8), 5262-5271.
- Stipe, B. C.; Strand, T. C.; Poon, C. C.; Balamane, H.; Boone, T. D.; Katine, J. A.; Li, J.-L.; Rawat, V.; Nemoto, H.; Hirotsune, A.; Hellwig, O.; Ruiz, R.; Dobisz, E.; Kercher, D. S.; Robertson, N.; Albrecht, T. R.; Terris, B. D., Magnetic recording at 1.5 Pb m⁻² using an integrated plasmonic antenna. *Nature Photonics* 2010, 4 (7), 484-488.

Stuart, S. J.; Tutein, A. B.; Harrison, J. A., A reactive potential for hydrocarbons with intermolecular interactions. *The Journal of Chemical Physics* 2000, 112 (14), 6472-6486.

Šunka, P., Pulse electrical discharges in water and their applications. *Physics of Plasmas* 2001, 8 (5), 2587-2594.

Sur, A.; Lu, Y.; Pascente, C.; Ruchhoeft, P.; Liu, D., Pool boiling heat transfer enhancement with electrowetting. *International Journal of Heat and Mass Transfer* 2018, 120, 202-217.

Tao, Y.; Liu, C.; Chen, W.; Cai, S.; Chen, C.; Wei, Z.; Bi, K.; Yang, J.; Chen, Y., Mean free path dependent phonon contributions to interfacial thermal conductance. *Physics Letters A* 2017, 381 (22), 1899-1904.

Vakilian, M.; Majlis, B. Y. In Study of interdigitated electrode sensor for lab-on-chip applications, 2014 IEEE International Conference on Semiconductor Electronics (ICSE2014), IEEE: 2014; pp 201-204.

Van Gerwen, P.; Laureys, W.; Huyberechts, G.; De Baeck, M.; Baert, K.; Suis, J.; Varlan, A.; Sansen, W.; Hermans, L.; Mertens, R., Nanoscaled interdigitated electrode arrays for biochemical sensors. In *Proceedings of International Solid State Sensors and Actuators Conference (Transducers '97)*, 1997; pp 907-910.

Vera, J.; Bayazitoglu, Y., Temperature and heat flux dependence of thermal resistance of water/metal nanoparticle interfaces at sub-boiling temperatures. *International Journal of Heat and Mass Transfer* 2015, 86, 433-442.

Vo, T. Q.; Barisik, M.; Kim, B., Atomic density effects on temperature characteristics and thermal transport at grain boundaries through a proper bin size selection. *J Chem Phys* 2016, 144 (19), 194707.

Vo, T. Q.; Kim, B., Physical origins of temperature continuity at an interface between a crystal and its melt. *J Chem Phys* 2018, 148 (3), 034703.

Wang, B.-B.; Wang, X.-D.; Wang, T.-H.; Lu, G.; Yan, W.-M., Enhancement of boiling heat transfer of thin water film on an electrified solid surface. *International Journal of Heat and Mass Transfer* 2017, 109, 410-416.

Wang, Y.; Keblinski, P., Role of wetting and nanoscale roughness on thermal conductance at liquid-solid interface. *Applied Physics Letters* 2011, 99 (7).

Wei, N.; Li, S.; Zhang, Y.; Chen, J.; Chen, Y.; Zhao, J., Thermal rectification of graphene on substrates with inhomogeneous stiffness. *Carbon* 2019, 154, 81-89.

Wei, S.; Xiaobin, X.; Hong, Z.; Chuanxiang, X., Effects of dipole polarization of water molecules on ice formation under an electrostatic field. *Cryobiology* 2008, 56 (1), 93-9.

Weller, D.; Mosendz, O.; Richter, H. J.; Parker, G.; Pisana, S.; Santos, T. S.; Reiner, J.; Hellwig, O.; Stipe, B.; Terris, B., Sub-nanosecond Heat Assisted Magnetic Recording of FePt Media. In *Ultrafast Magnetism I*, 2015; pp 228-231.

Werder, T.; Walther, J. H.; Jaffe, R. L.; Halicioglu, T.; Koumoutsakos, P., On the Water–Carbon Interaction for Use in Molecular Dynamics Simulations of Graphite and Carbon Nanotubes. *The Journal of Physical Chemistry B* 2003, 107 (6), 1345-1352.

Wu, J. B.; Lin, M. L.; Cong, X.; Liu, H. N.; Tan, P. H., Raman spectroscopy of graphene-based materials and its applications in related devices. *Chem Soc Rev* 2018, 47 (5), 1822-1873.

Xie, G.; Luo, J.; Guo, D.; Liu, S., Nanoconfined ionic liquids under electric fields. *Applied Physics Letters* 2010, 96 (4).

Xing Zhang, Z. G., Zhang_2012_Micro nanoscale heat transfer interfacial effects dominate the heat transfer. *ASME International Conference on Micro/Nanoscale Heat and Mass Transfer* 2012, 54778, 961-970.

Yan, J. Y.; Patey, G. N., Molecular dynamics simulations of ice nucleation by electric fields. *J Phys Chem A* 2012, 116 (26), 7057-64.

Yan, Z.; Liu, G.; Khan, J. M.; Balandin, A. A., Graphene quilts for thermal management of high-power GaN transistors. *Nat Commun* 2012, 3, 827.

Yang, J.; Shen, M.; Yang, Y.; Evans, W. J.; Wei, Z.; Chen, W.; Zinn, A. A.; Chen, Y.; Prasher, R.; Xu, T. T.; Koblinski, P.; Li, D., Phonon Transport through Point Contacts between Graphitic Nanomaterials. *Physical Review Letters* 2014, 112 (20).

Yang, J. Z.; Wu, X.; Li, X., A generalized Irving-Kirkwood formula for the calculation of stress in molecular dynamics models. *J Chem Phys* 2012, 137 (13), 134104.

Yenigun, O.; Barisik, M., Effect of nano-film thickness on thermal resistance at water/silicon interface. *International Journal of Heat and Mass Transfer* 2019, 134, 634-640.

Yenigun, O.; Barisik, M., Electric Field Controlled Heat Transfer Through Silicon and Nano-confined Water. *Nanoscale and Microscale Thermophysical Engineering* 2019, 23 (4), 304-316.

Yenigun, O.; Barisik, M., Local Heat Transfer Control using Liquid Dielectrophoresis at Graphene/Water Interfaces. *International Journal of Heat and Mass Transfer* 2021, 166.

Yousefzadi Nobakht, A.; Ashraf Gandomi, Y.; Wang, J.; Bowman, M. H.; Marable, D. C.; Garrison, B. E.; Kim, D.; Shin, S., Thermal rectification via asymmetric structural defects in graphene. *Carbon* 2018, 132, 565-572.

Yousefzadi Nobakht, A.; Shin, S., Anisotropic control of thermal transport in graphene/Si heterostructures. *Journal of Applied Physics* 2016, 120 (22).

Yu, X.; Cheng, H.; Zhang, M.; Zhao, Y.; Qu, L.; Shi, G., Graphene-based smart materials. *Nature Reviews Materials* 2017, 2 (9).

Zhang, J.; Borg, M. K.; Ritos, K.; Reese, J. M., Electrowetting Controls the Deposit Patterns of Evaporated Salt Water Nanodroplets. *Langmuir* 2016, 32 (6), 1542-9.

Zhang, J.; Hong, Y.; Liu, M.; Yue, Y.; Xiong, Q.; Lorenzini, G., Molecular dynamics simulation of the interfacial thermal resistance between phosphorene and silicon substrate. *International Journal of Heat and Mass Transfer* 2017, 104, 871-877.

Zhang, Z.; Matin, M. A.; Ha, M. Y.; Jang, J., Molecular Dynamics Study of the Hydrophilic-to-Hydrophobic Switching in the Wettability of a Gold Surface Corrugated with Spherical Cavities. *Langmuir* 2016, 32 (37), 9658-63.

Zhao, Y.; Cho, S. K., Micro air bubble manipulation by electrowetting on dielectric (EWOD): transporting, splitting, merging and eliminating of bubbles. *Lab Chip* 2007, 7 (2), 273-80.

Zhu, X.; Yuan, Q.; Zhao, Y. P., Phase transitions of a water overlayer on charged graphene: from electromelting to electrofreezing. *Nanoscale* 2014, 6 (10), 5432-7.

VITA

ONUR YENİGÜN

EDUCATION

- Ph.D. in Mechanical Engineering, İzmir Institute of Technology (2021)
- Research Master (RM) in Environmental and Applied Fluid Dynamics, von Karman Institute for Fluid Dynamics (2017)
- M.Sc. in Mechanical Engineering, İzmir Institute of Technology (2016)
- B.Sc. in Mechanical Engineering, İzmir Institute of Technology (2014)

RESEARCH INTERESTS

Core areas of the Thermofluids, Micro/Nano-scale Heat Transfer, Microfluidics, Electric Field Applications in Nano-scale

LANGUAGE

Turkish (Native), English (Full professional proficiency)

SELECTED PUBLICATIONS

- **Yenigun O**, Barisik M, "Local heat transfer control using liquid dielectrophoresis at graphene water interfaces" International Journal of Heat and Mass Transfer 166 (2021), 120801
- Esposito C, **Yenigun O**, Gouriet J-B, Steelant J, Vetrano R, "Void fraction and speed of sound measurements in cavitating flows by the Three Pressure Transducers (3PT) technique" Experimental Thermal and Fluid Science 112 (2020), 109949
- **Yenigun O**, Barisik M, "Electric field controlled heat transfer through silicon and nanoconfined water" Nanoscale and Microscale Thermophysical Engineering 23 (4) (2019), 304-316
- **Yenigun O**, Barisik M, "Effect of nano-film thickness on thermal resistance at water silicon interface" International Journal of Heat and Mass Transfer, 134 (2019) 634-640
- **Yenigun O**, Cetkin E, "Experimental and numerical investigation of constructal vascular channels for self-cooling: Parallel channels, tree-shaped and hybrid designs" International Journal of Heat and Mass Transfer, 103 (2016) 1155–1165

CONFERENCE PROCEEDINGS

- **Yenigun O**, Barisik M, "Effects of electric field on interfacial thermal resistance between silicon and water at nano-scales", 6th International Conference on Heat Transfer and Fluid Flow, August 2019, Lisbon, Portugal (**Best Paper Award**)
- **Yenigun O**, "Constructal tree-shaped designs for self-cooling" Constructal Law and Second Law Conference, May 2015, Parma, Italy